TOWARDS A ROBOT ASSISTED BREAST BIOPSY SYSTEM

By

Vishnu Mallapragada

Dissertation

Submitted to the Faculty of the

Graduate School of Vanderbilt University

in partial fulfillment of the requirements

for the degree of

DOCTOR OF PHILOSOPHY

in

Mechanical Engineering

December, 2008

Nashville, Tennessee

Approved:

Professor Nilanjan Sarkar

Professor Eric Barth

Professor George E. Cook

Professor Michael Goldfarb

Professor Tarun K. Podder

ACKNOWLEDGEMENTS

TABLE OF CONTENTS

LIST OF TABLES

LIST OF FIGURES

LIST OF ABBREVIATIONS

3D	Three Dimensional
US	Ultrasound
FNAB	Fine Needle Aspiration Biopsy
CNB	Core Needle Biopsy
PBC	Passivity Based Control
2D	Two Dimensional
P	Proportional
PI	Proportional-Integral
PID	Proportional-Integral-Derivative
PO	Passivity Observer
PC	Passivity Controller
PBC	Passivity Based Control
RIBBS	Robotic Image-guided Breast Biopsy System
DOF	Degrees Of Freedom
DOA	Degrees Of Actuation
PPM	Pulse Position Modulation
D-H	Denavit-Hartenberg
SC	Supervisory Controller
DES	Discrete Event System
LED	Light Emitting Diode
WRLS	Weighted Recursive Least Squares

EM	ElectroMagnetic

CHAPTER I

INTRODUCTION

Subcutaneous insertion of a surgical device is common in clinical practice. In minimally invasive procedures such as hollow core needle biopsy, percutaneous tumor ablation etc., a surgical instrument is inserted into soft, inhomogeneous tissue in order to sample or remove a target (in this work the word target is used to refer to a tumor, a lesion or just a suspected region of tissue). In such procedures it is critical to position the instrument tip precisely at the target. Accurate needle placement at the target location is essential to reduce false negative results during biopsies. "While many factors are important to achieve local tumor control of a targeted lesion when using percutaneous image-guided ablation devices, the most important one is accurate placement of the device in the center of the targeted tumor." [1]

Minimally invasive procedures have numerous benefits such as low cost, short operating time, quick recovery of patient etc. Despite these advantages, precise placement of a surgical needle at the target is challenging because of several reasons such as tissue heterogeneity and elastic stiffness, tissue deformation and movement, and poor maneuverability of the needle. For procedures involving small diameter needles (such as the 18 – 25 gauge needles used for FNAB), heterogeneous nature of the tissue causes needle bending during insertion. For procedures involving large diameter needles (such as 10 – 14 gauge needles used for CNB) if the tip of the needle reaches interface between two different types of tissue, its further insertion will push the tissue, instead of piercing it, causing unwanted deformations. Tissue deformation causes the target to move away from the line of insertion of the needle

especially for deep seated targets. [2] describes a 3D finite element model of needle insertion in soft tissue. Results presented in [2] show that as the needle is inserted, large tissue deformation causes the target to move away from the path of the needle. Target motion can also be caused due to breathing or other involuntary movement of the patient. Since needle insertion point and needle orientation (in this work, the word orientation is used to refer to the six degrees of freedom of the needle) are chosen by assuming a straight line path to the target, needle bending or target motion causes error in placing the needle tip at the target location. In spite of the considerable skill of a clinician, it is difficult to achieve accurate and consistent results through manual compensation of needle - target misalignment.

Manually performed US guided needle breast biopsy and stereotactic breast biopsy have false negative rates of 1.7% and 8.9% respectively [3]. US guided procedures have lower false negative rates due to availability of real time image guidance. One of the main causes of false negative results is suboptimal sampling [4]. Suboptimal sampling is a direct consequence of target motion due to patient movement and tissue deformation. False negative rate for breast biopsy is fairly low, since, in clinical practice several insertions are performed to achieve good needle – target alignment. It has been noted that approximately five insertions are required to align a 3 mm target with manual needle insertion [5]. Retargeting (retraction of the needle and reinsertion due to needle – target misalignment) is also common for stereotactic breast biopsies. Retargeting and multiple insertions cause excessive bleeding which obscures the guiding images and causes significant discomfort to the patient. Retargeting is also fatiguing for the clinician and increases procedural time which is directly related to cost of the procedure.

In order to overcome the above limitations, significant research effort is being made to

investigate techniques that can address the problem of needle - target misalignment during needle insertion. In [6]-[8], steerable devices are presented that allow the clinician to steer the tip of the needle towards the target during insertion. A visually controlled needle-guiding system is developed in [9] for automatic or remote controlled percutaneous interventions. In the automated mode, the needle insertion path is updated based on image feedback to the needle-guiding system. Though these systems potentially reduce the number of insertions required to sample the target, maneuvering a needle inside the body causes tissue damage. In [10][11], a finite element model is used to predict movement of the target. Needle path is planned based on this prediction to accurately sample the target. To get an accurate prediction of the movement of the target, finite element analysis requires the geometric model and mechanical properties of the anatomical structures. In addition, finite element computation is not real-time. For example, in [10], the average time for computation is 29 minutes.

In this work, a new paradigm for image guided minimally invasive procedures is presented. In this approach a robotic system will be able to position a target inline with a surgical device during insertion in a safe and accurate manner. The system developed is for automating US guided breast CNB although much of the system development could be adapted to other real time imaging modalities and for performing FNAB, ablation etc

During US guided breast CNB a clinician inserts a needle through an incision to remove a tissue sample. A schematic of needle insertion in a breast is shown in Fig. 1.1. The two dimensional plane of the figure represents a horizontal plane passing through the target (the target mass in Fig. 1.1). In the figure, a simplified anatomy for the breast is shown. In reality, breast tissue is inhomogeneous and its biomechanical properties are nonlinear. Hence, if the

tip of the needle reaches the interface between two different types of tissue, its further insertion will push the tissue, instead of piercing it, causing unwanted deformations. These deformations move the target away from its original location, as shown in Fig. 1.1.b. The robotic system which consists of a set of actuators positioned around the breast applies force on the surface of the breast based on the image of the target to guide the target towards the line of insertion of the needle (Fig 1.1.c). This approach is independent of the specific surgical device used for performing the procedure. The accuracy of this system is demonstrated with a vacuum assisted biopsy needle. The system can autonomously position a target at a desired location (typically in the path of the needle) with a high degree of accuracy.
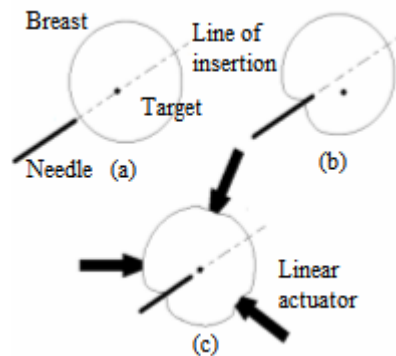
Fig. 1.1. Needle insertion schematic for breast CNB.

This robotic device has the following potential advantages: (a) Success rate (defined by the number of insertions required at a particular biopsy site to successfully sample the target tissue) of the procedure will be increased since the target is accurately positioned inline with the needle. (b) Since the number of insertions required is expected to be less, it will reduce fatigue of the clinician and patient discomfort. (c) The entire procedure is predicted to be

fast, making it clinically viable. (d) Since the needle is not steered inside the breast, and the number of insertions reduced, tissue damage is also potentially minimized and the structural integrity of the tissue specimen is preserved. (e) Geometric and mechanical properties of the breast are not required for precise positioning of the target. (f) By improving accuracy of biopsy, it will potentially enhance the diagnostic outcome by reducing the false negative rate.

This dissertation is organized as follows: Chapter II casts the needle – target alignment problem in a control framework and develops a PBC approach for manipulation of deformable objects (soft tissue is a specific instance of a deformable object). Chapter III develops the design of a integrated robotic system for automating US guided breast CNB. This system automates and integrates needle – target alignment, image acquisition and processing, and US probe motion to provide comprehensive assistance for performing breast CNB. Chapter IV presents experimental results on phantoms with varying elastic properties to verify validity of the approach. This chapter also presents a discussion on the targeting accuracy of this technique. Chapter V describes the contributions of this work.

CHAPTER II

MANIPULATION OF DEFORMABLE OBJECTS

Precise position control of a target embedded in soft tissue requires the ability to manipulate the soft tissue surrounding the target. The breast is a many layered organ consisting of various structures such as lobules, Cooper's ligaments and connective tissue. Biomechanical models of breast predominantly consist of two different types of tissue: fatty and glandular [12][10]. These tissues display viscoelastic response and in order to develop tractable mathematical models, researchers have assumed these tissues to be isotropic [14].

There is a lot of research in robotic grasping and manipulation of deformable objects with a wide range of applications [15][16]. In general, a deformable object is defined as an object whose degrees of freedom are characterized by viscoelastic interactions between the molecules. A deformable object changes its shape when an external force is applied [17]. Thus, breast tissue is a subset of a general class of inhomogeneous deformable objects and techniques used for robotic manipulation of deformable objects can be exploited for position control of a target embedded in soft tissue. Conversely, techniques developed for soft tissue manipulation can also be applied in other fields such as robotic assembly of flexible parts, fabric manipulation in textile manufacturing etc.

As will be discussed in Chapter III, ensuring needle – target alignment during breast CNB requires planar target position control. Hence, in this chapter, a technique for planar manipulation of deformable objects is developed.

Techniques for Deformable Object Manipulation

[19] presents an overview of research related to robotic grasping and manipulation of deformable objects with vision and tactile guidance. A general approach for position control of a nonlinear flexible structure is presented in [19]. The controller presented in [19] guarantees global asymptotic stability of the closed loop. However, convergence of the output displacement (target point) to the desired position requires accurate knowledge of the stiffness of the system. A passivity based controller for flexible structures is presented in [20]. This controller uses nominal model information to construct an observer and maps the reconstructed state to an approximate passive output. The controllers developed in [19][20] require information regarding the system model. In most cases, having a model of a nonlinear inhomogeneous deformable object is not feasible.

A simple PID controller is developed in [21] for manipulation and position control of deformable objects. Results presented in [21] show good convergence of the target points to the desired position but stability is not guaranteed due to noncollocation of the sensor and actuators. This controller is noncollocated since the desired configuration of the object is specified in terms of the states (target position) that are not directly actuated. PID controller design for a flexible link manipulator is developed in [22]. Due to distributed flexibility, a deformable object/manipulator is inherently an infinite dimensional system. But for control purposes, a finite dimensional model is obtained in [22] using system identification techniques. PID control gains are then chosen using H_∞ control synthesis to guarantee robust performance.

An adaptive technique for control of a flexible structure with noncollocated sensors and actuators is presented in [23]. In [23], an adaptive PI controller with feedforward

augmentation is used to stabilize the system. Due to feedforward augmentation, only boundedness of the tracking error is guaranteed. An impedance controller for a class of underactuated Euler-Lagrange systems based on energy shaping is presented in [24]. This approach is based on the fact that at equilibrium, there is an algebraic relationship (defined by a Jacobian) between the noncollocated and collocated variables. Design of a stabilizing controller is reduced to solving this algebraic equation for the noncollocated variable. [25] presents a model independent passivity based approach to guarantee stability of a flexible manipulator with a noncollocated sensor-actuator pair. This technique uses an active damping element to dissipate energy when the system becomes active. A similar approach is developed in this chapter for manipulation of deformable objects with multiple robotic fingers.

Geometric Arrangement of Robotic Fingers

Before discussing the control system development, the goal is to determine the number of robotic fingers and their geometric arrangement necessary for planar position control of a target embedded inside the deformable object. Fig 2.2.1 shows the schematic of a robotic finger (a rigid link mechanism driven by a rotary or linear actuator) in contact with a deformable object. Without loss of generality, a circular deformable object is shown.
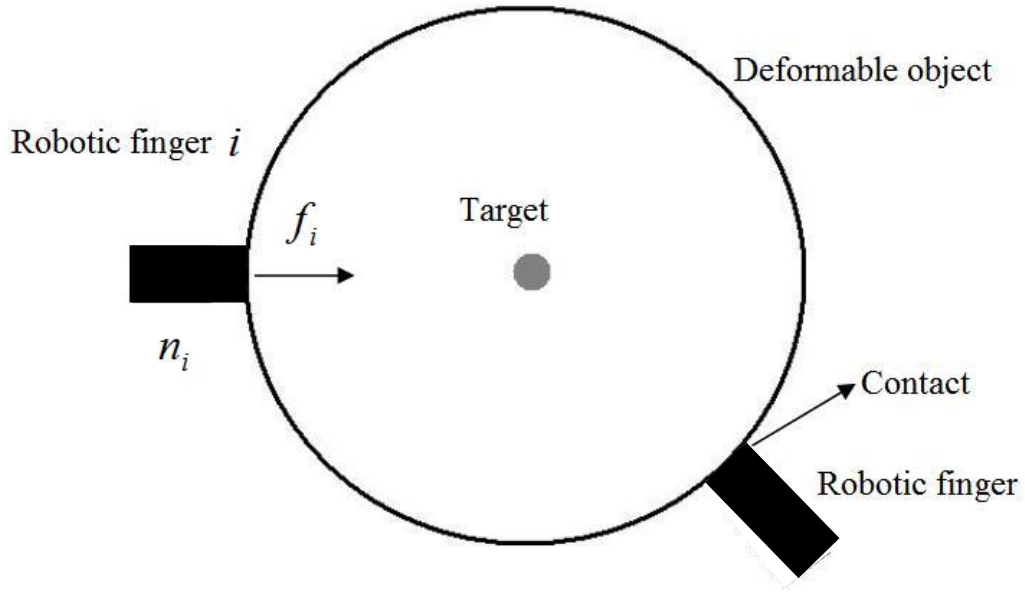
Fig. 2.2.1. Robotic fingers in contact with a deformable object.

In [21][26][27], the authors prove that one can control an internal point inside a deformable medium by applying force from the boundary. They further determine the number of robotic fingers required to position the target at an arbitrary location in the horizontal plane.

Result [27]: The number of manipulated (contact) points must be greater than or equal to that of the positioned (target) points in order to realize any arbitrary displacement.

In this case, the number of positioned points is one, since we are trying to control the position of just the target. Hence, ideally the number of manipulated points would also be one. But there are two practical constraints associated with this technique: (1) shear force on the surface should be minimized to avoid damage to the surface of the object; (2) the robotic finger is not rigidly attached to the surface, hence, only compressive forces directed into the object can be applied.

Thus this problem is more restrictive than [21][26][27] since the position of the target

needs to be controlled by applying only compressive force. However, there exists a general

theorem in Mechanics [28] that determines the equivalent number of compressive forces that

can replace one unconstrained force in a 2D plane.

Theorem [28]: A set of wrenches W can generate forces in any direction (in a plane) if and

only if there exists a three-tuple of wrenches $\{w_1, w_2, w_3\}$ *whose respective force directions*

n_1, n_2, n_3 *satisfy:*

- *Two of the three directions* n_1, n_2, n_3 *are independent.*

- *A strictly positive combination of the three directions is zero,*

$$\sum_{i=1}^{3} \alpha_i n_i = 0, \quad \alpha_i > 0.$$
(2.2.1)

The ramification of this theorem is that: (1) three robotic fingers are required; (2) the

arrangement of the fingers should be such that the end points of their force direction vectors

draw a non-zero triangle that includes their common origin point. With such an arrangement

the target position can be controlled in a plane.
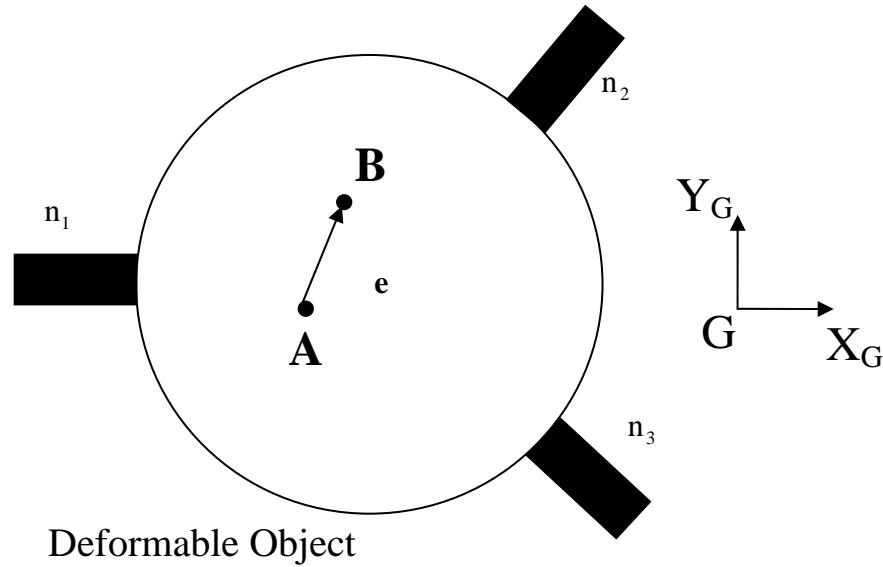
Fig. 2.3.1. Manipulation for target position control using robotic fingers.

Fig. 2.3.1 shows a schematic of three robotic fingers in contact with a deformable object. In this section, a control law for the robotic fingers is developed to guide a target from any point A to an arbitrary point B within the deformable object. At any given timestep, point A is the actual location of the target and point B is the desired location of the target. In Fig. 2.3.1, $\mathbf{e}$ (according to standard convention, letters in bold represent vectors) is the error vector pointing from A to B and indicates the error in target position. n_1, n_2 and n_3 are unit vectors which determine the direction of force application of the robotic fingers with respect to the global reference frame G.

Fig. 2.3.2 is a schematic of the control structure for the entire system. In Fig. 2.3.2, $\mathbf{P_d}$ is the position vector of point B and $\mathbf{P_t}$ is the position vector of point A. The position vector

11

of point A is determined using image feedback. Error vector, $\mathbf{e}$, is the difference between the desired and the actual target position. An outer loop controller (P control) determines the desired velocity for the actuators (which drive the robotic fingers), $\dot{\mathbf{x}}_d$, depending on the target position error. A servo loop controller (PI controller) acts on the error between the desired and actual actuator velocities, $\dot{\mathbf{x}}$, to generate the actuator input, $\mathbf{v}$. The desired control objective can be achieved with just the outer loop controller, the inner servo loop is used to add damping to the system [29]. The actuator velocities are determined using approximate differentiation of the position signals. The actuators drive the robotic fingers to apply a controlled external force, $\mathbf{f_c}$, on the surface of the object to guide the target towards the desired position. The control loop mitigates the effect of an external disturbance force, $\mathbf{f_n}$, on the target position.
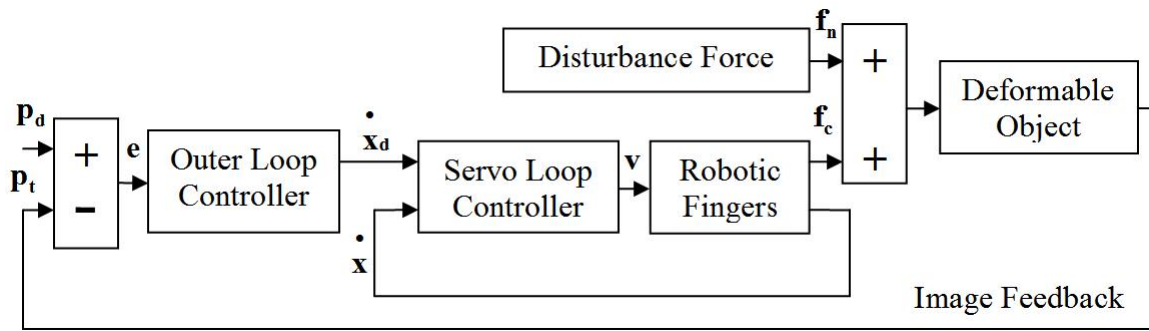
Fig. 2.3.2. Control structure for manipulating deformable objects.

The stability of the above control system is analyzed using a passivity based approach. First, the sign convention for all forces and velocities is defined such that their product is positive when power enters the system port. The following definition is used to analyze the passivity property of the system.

Definition [30]: The M-port network, N_M (Fig. 2.3.3), with initial energy storage $E(0)$ is passive if and only if,

$$\int_0^t \left[f_1(\tau)v_1(\tau) + \cdots + f_m(\tau)v_m(\tau) \right] d\tau + E(0) \geq 0, \quad \forall t \geq 0 . \tag{2.3.1}$$

for all admissible forces $(f_1, \cdots, f_m)$ and velocities $(v_1, \cdots, v_m)$.
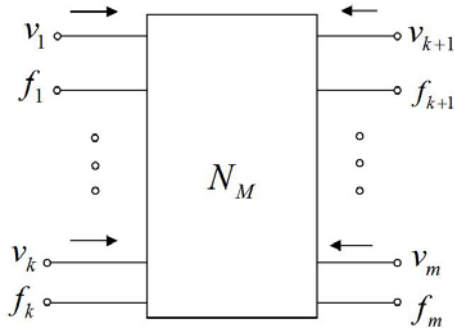
Fig. 2.3.3. M-port network

Similar to [31], energy is defined as the integral of the inner product between conjugate input and output, which may or may not correspond to physical energy. Equation (2.3.1) states that the energy applied to a passive network must be positive for all time. Fig. 2.3.4 shows a network representation of the energetic behavior of this control system. The block diagram in Fig. 2.3.3 is partitioned into four elements: the trajectory generator, outer loop controller, servo controller and plant. Each outer and servo loop controller pair corresponds to one actuator. Since three robotic fingers are used for planar manipulation, three controller pairs transfer energy to the plant.
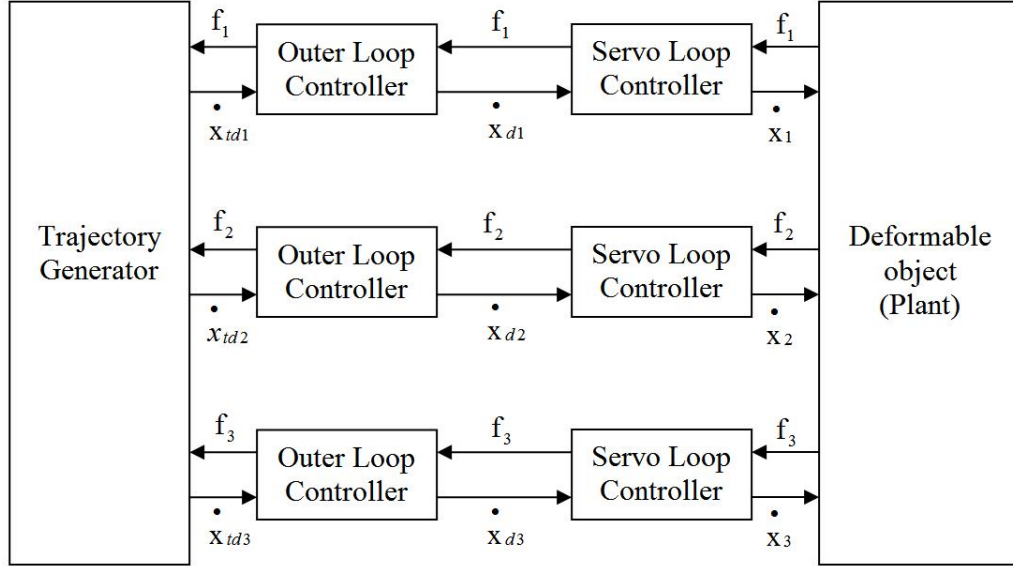
Fig. 2.3.4. Network representation of deformable object manipulation.

The connection between servo loop controller and plant is a physical interface at which

conjugate variables (f_i, $\dot{x}_i$; where f_i is the force applied by actuator i and $\dot{x}_i$ is the velocity of

actuator i) define physical energy flow between controller and plant. In this work, the

subscript i refers to the ith finger. i takes values of 1, 2 and 3 representing the three fingers.

$$\mathbf{f_c} = \begin{bmatrix} f_1 & f_2 & f_3 \end{bmatrix}^T. \tag{2.3.2}$$

$$\dot{\mathbf{x}} = \begin{bmatrix} \dot{x}_1 & \dot{x}_2 & \dot{x}_3 \end{bmatrix}^T. \tag{2.3.3}$$

The connections between trajectory generator and outer loop controller, and outer loop

controller and servo loop controller, which traditionally consist of a one-way command

information flow, are modified by the addition of a virtual feedback of the conjugate variable

[31]. For the system shown in Fig. 2.3.4, output of the trajectory generator is the desired

target velocity ($\dot{x}_{tdi}$ is the desired target velocity along direction of finger i) and output of

the outer loop controller is the desired actuator velocity ($\dot{x}_{di}$ is the desired actuator velocity for actuator i).

$$\dot{\mathbf{x}}_{\mathbf{d}} = \begin{bmatrix} \dot{x}_{d1} & \dot{x}_{d2} & \dot{x}_{d3} \end{bmatrix}^T. \qquad (2.3.4)$$

For both connections, virtual feedback is the force applied by the robotic fingers. Integral of the inner product between trajectory generator output ($\dot{x}_{tdi}$) and its conjugate variable (f_i) defines "virtual input energy". The virtual input energy is generated to give a command to the outer loop controller, which transmits the input energy to the plant through the servo loop controller in the form of "real output energy". Real output energy is the physical energy that enters the plant (deformable object) at the point where the robotic finger is in contact with the object. Therefore the plant is a three-port system since three fingers manipulate the object. The conjugate pair that represents the power flow is f_i, $\dot{x}_i$ (force and velocity of finger i, respectively). The reason for defining virtual input energy is to transfer the source of energy from the controllers (outer and servo loop) to the trajectory generator. Thus the controllers can be represented as two-ports which characterize energy exchange between the trajectory generator and the plant. Note that the conjugate variables that define power flow are discrete time values and so the analysis is confined to systems having a sampling rate substantially faster than the system dynamics.

For regulating the target position during manipulation, $\dot{x}_{tdi} = 0$. Hence the trajectory generator is passive since it does not generate energy. However, for target tracking, $\dot{x}_{tdi} \neq 0$ and $f_i \neq 0$. Therefore the trajectory generator is not passive because it has a velocity source as a power source. It is shown that even if the system has an active term, stability is

guaranteed as long as the active term is not dependent on the system states [32]. Therefore, passivity of the plant and controllers is sufficient to ensure system stability.

Elastic systems with collocated and compatible actuators and sensors are inherently passive [33]. Therefore, the plant is passive with respect to the pair f_i and $\dot{x}_i$, since this conjugate pair is collocated and compatible. It is known that a PI controller (servo loop controller) is output strictly passive with respect to the conjugate pair f_i, $-\dot{x}_i$ [34]. However, the outer loop controller (P controller) may not be passive.

The virtual energy generated by the ith outer loop controller at the nth timestep, $E_i(n)$, is given by

$$E_i(n) = E_i(n-1) + \Delta T \left[f_i(n) \left(Sat_2(\dot{x}_{tdi}(n)) + Sat_3(\dot{x}_{di}(n)) \right) \right]. \tag{2.3.5}$$

In the above equation, $E_i(n-1)$ is the energy generated by the ith outer loop controller at the $(n-1)$[th] timestep; ΔT is the sampling time; $f_i(n)$ is the force applied by the ith finger at n[th] timestep, respectively; $\dot{x}_{tdi}(n)$ and $\dot{x}_{di}(n)$ are the desired target and actuator velocities at n[th] timestep. The saturation functions, $Sat_2(q)$ and $Sat_3(q)$, are defined for any variable q, as follows:

$$Sat_2(q) = \begin{cases} q & \text{if} \quad q > 0 \\ 0 & \quad q \le 0 \end{cases}. \tag{2.3.6}$$

$$Sat_3(q) = \begin{cases} q & \text{if} \quad q < 0 \\ 0 & \quad q \ge 0 \end{cases}. \tag{2.3.7}$$

Robotic fingers compress the tissue when the velocity of the finger is negative. Since the fingers transfer energy to the object only during compression, energy generated by the outer loop controller during compression is only considered for passivity analysis. The net energy

16

output of the ith outer loop controller at the nth timestep, $E_{neti}(n)$, is given by

$$E_{neti}(n) = E_{0i} + E_i(n), \tag{2.3.8}$$

where E_{0i} is the initial stored energy of ith outer loop controller. The ith outer loop controller is not passive when $E_{neti}(n) < 0$. This can cause instability of the control system as shown in Fig. 2.3.2 and Fig. 2.3.4.

Passivity Based Control

A passivity control approach based on energy monitoring is developed for deformable object manipulation to guarantee passivity (and consequently stability) of the system. The basic idea is to use a passivity observer (PO) to monitor the energy generated by the outer loop controller (Fig. 2.3.4) and to dissipate excess energy using a passivity controller (PC) when the controller becomes active [31].

Target Position Error

Referring to Fig. 2.3.1, point A denotes the actual position of the target. The position vector of point A is given by

$$\mathbf{P_t} = \begin{bmatrix} x_t & y_t \end{bmatrix}^T, \tag{2.4.1}$$

where x_t and y_t are the position coordinates of point A in the global reference frame G. The desired target position is represented by point B whose position vector is given by

$$\mathbf{P_d} = \begin{bmatrix} x_{td} & y_{td} \end{bmatrix}^T. \tag{2.4.2}$$

x_{td} and y_{td} are the desired target position coordinates. The desired target velocity is obtained by differentiating Eq. 2.4.2 with respect to time.

$$\dot{\mathbf{p}}_\mathbf{d} = \begin{bmatrix} \dot{x}_{td} & \dot{y}_{td} \end{bmatrix}^T. \tag{2.4.3}$$

$\dot{x}_{td}$ and $\dot{y}_{td}$ are the desired target velocities along X_G and Y_G, respectively. The target position error, **e,** is

$$\mathbf{e} = \mathbf{P_d} - \mathbf{P_t}. \tag{2.4.4}$$

Outer Loop Controller with Saturation Feedback Compensation

The desired target velocity along the direction of actuation of the ith finger, $\dot{x}_{tdi}$, is

$$\dot{x}_{tdi} = \dot{\mathbf{p}}_\mathbf{d} \cdot \mathbf{n_i}, \tag{2.4.5a}$$

where,

$$\mathbf{n_i} = \begin{bmatrix} n_1 & n_2 & n_3 \end{bmatrix}^T. \tag{2.4.5b}$$

The error vector is resolved into components along the actuation directions as follows:

$$e_i = \mathbf{e} \cdot \mathbf{n_i}. \tag{2.4.6}$$

A proportional – integral (PI) controller is used for the outer loop which generates the desired velocity for actuator i.

$$\dot{x}_{di} = K_{pi} e_i^* + K_{Ii} \int e_i^* \, dt. \tag{2.4.7}$$

K_{pi} is the proportional gain K_{Ii} is the integral gain for the ith outer loop controller. e_i^* is the modified error with saturation feedback.

$$e_i^* = e_i + |e_i| \cdot \mathrm{sgn}\!\left[\mathrm{Sat}_1(J_i) - J_i \right]. \tag{2.4.8}$$

J_i is the estimated target position

$$J_i = \int \dot{x}_i \, dt. \tag{2.4.9}$$

The saturation function, $\text{Sat}_1(q)$, is defined for any variable q, as

$$\text{Sat}_1(q) = \begin{cases} q & \text{if} \quad l_{imin} < q < l_{imax} \\ l_{imin} & \text{if} \quad q \leq l_{imin} \\ l_{imax} & \text{if} \quad q \geq l_{imax} \end{cases} \quad , \quad (2.4.10)$$

where l_{imin} and l_{imax} represent the limits of motion of finger i. The result of using saturation feedback compensation (Eqs. 2.4.8 – 2.4.10) is that when finger i is within its limits of motion, $\dot{x}_{di}$ is computed using Eq. 2.4.7. When finger i reaches its limit, $\dot{x}_{di} = 0$. There are several advantages in using such a scheme: (a) wear on the actuator is minimized; (b) wind up of the servo controller is eliminated, and (c) limits of finger motion can be chosen based on safety considerations, thereby reducing the risk of accidental damage to the object.

Passivity Observer

The passivity observer (PO) and passivity controller (PC) are implemented as shown in Fig. 2.4.1. The PO monitors the combined energy output of the three outer loop controllers. When the energy becomes negative, PC dissipates energy from the controllers, based on the contribution of the individual controllers to the net energy output. Thus, passivity of the system (dotted box in Fig. 2.4.1) with three outer loop controllers and PO/PC is ensured.
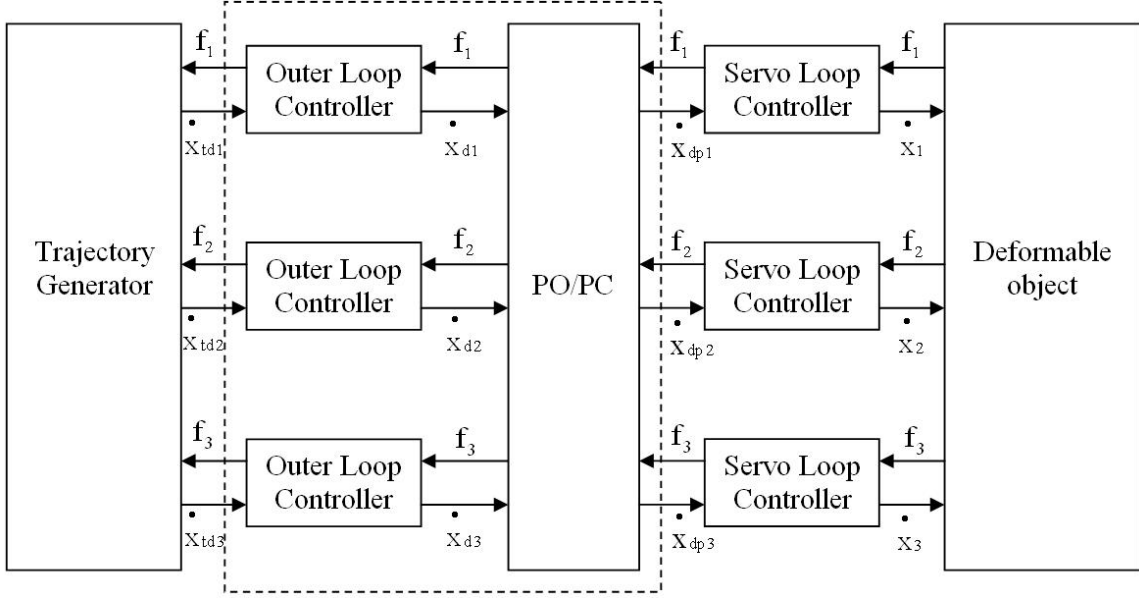
Fig. 2.4.1. Network representation of deformable object manipulation with PBC.

Net energy output of an individual outer loop controller is given by

$$E_i(n) = E_i(n-1) + \Delta T \left[\frac{f_i(n-1)^2}{\alpha_i(n-1)} + f_i(n) \left(Sat_2(\overset{\bullet *}{x}_{tdi}(n)) + Sat_3(\overset{\bullet}{x}_{di}(n)) \right) \right], \quad (2.4.11)$$

where, $\dfrac{f_i(n-1)^2}{\alpha_i(n-1)} \Delta T$ is the energy dissipated by the PC at the $(n-1)^{th}$ timestep. $\dfrac{1}{\alpha_i(n-1)}$ is

the damping coefficient from Eq. 2.4.15. $f_i(n) \left(Sat_2(\overset{\bullet *}{x}_{tdi}(n)) + Sat_3(\overset{\bullet}{x}_{di}(n)) \right) \Delta T$ is the energy

generated at the nth timestep. $\overset{\bullet *}{x}_{tdi}$ is the modified desired target velocity (along n_i) with

saturation feedback similar to Eq. 2.4.8.

$$\overset{\bullet *}{x}_{tdi} = \overset{\bullet}{x}_{tdi} + \left| \overset{\bullet}{x}_{tdi} \right| \cdot sgn\left[Sat_1(J_i) - J_i \right]. \quad (2.4.12)$$

Saturation feedback is used for desired target velocity so that $\overset{\bullet *}{x}_{tdi} = \overset{\bullet}{x}_{tdi}$ when robotic

finger is within limits and $\overset{\bullet *}{x}_{tdi} = 0$ when the finger reaches the limit. When the finger reaches

20

its limit of motion, it does not follow the desired velocity command due to a mechanical stop. In such a case, energy is not supplied to the plant. Saturation feedback mitigates the effect of the trajectory generator supplying energy to the controller when the finger manipulators do not transfer this energy to the plant.

The total energy output of the outer loop controllers is

$$E_{obs}(n) = E_0 + \sum_{i=1}^{3} E_i(n),$$
(2.4.13)

where, E_0 is the combined initial energy of the controllers.

Passivity Controller

The passivity controller (PC) is a dissipative element that obeys the constitutive equation

$$f = \alpha v \ [35],$$
(2.4.14)

where f is force, v is velocity and α is the damping coefficient. The output of the outer loop controller is velocity and the input is force, which imposes admittance causality on the PC. When the observed energy becomes negative, the damping coefficient is computed using the following relation (which obeys the constitutive Eq. 2.4.14):

$$\frac{1}{\alpha_i(n)} = \begin{cases} -\dfrac{E_{obs}(n)}{\Delta T \cdot f_i(n)^2} \cdot r_i(n) & \text{if} \quad E_{obs}(n) < 0 \\ 0 & \text{if} \quad E_{obs}(n) \geq 0 \end{cases}.$$
(2.4.15)

In the above equation, r_i is a weighting factor that determines the ratio of energy dissipation from each controller. r_i is computed as follows:

$$r_i(n) = \frac{Sat_3[E_i(n)]}{\sum_{i=1}^{3} Sat_3[E_i(n)]}.$$
(2.4.16)

21

The computation for the weighting factor only considers active behavior of the (outer loop) controllers. When net output energy of a controller is positive, the corresponding term in Eq. 2.4.16 is zero. Therefore, PC dissipates energy only from the active controllers and the amount of energy dissipated at a port is directly proportional to the net output energy of the corresponding controller. Output of the PC is the desired velocity for i^{th} finger, $\dot{x}_{dpi}$, given by

$$\dot{x}_{dpi} = \dot{x}_{di} + \frac{f_i(n)}{\alpha_i(n)}. \tag{2.4.17}$$

When the ith (outer loop) controller is passive, $\dot{x}_{dpi} = \dot{x}_{di}$. When the ith controller is active $\dot{x}_{dpi}$ is computed using Eq. 2.4.17.

<div align="center">Passivity Proof</div>

The total energy of the system (dotted box in Fig. 2.4.1) with three outer loop controllers (at the nth timestep), $E(n)$ is given by

$$E(n) = E_0 + \sum_{i=1}^{3}\left[\sum_{k=0}^{n}\Delta T \cdot f_i(k)\left(Sat_2(\dot{x}_{tdi}^{*}(k)) + \dot{x}_{dpi}(k)\right)\right]. \tag{2.4.18}$$

Substituting from Eq. 2.4.17,

$$E(n) = E_0 + \sum_{i=1}^{3}\left[\sum_{k=0}^{n}\Delta T \cdot f_i(k)\left(Sat_2(\dot{x}_{tdi}^{*}(k)) + \dot{x}_{di}(k) + \frac{f_i(k)}{\alpha_i(k)}\right)\right]. \tag{2.4.19}$$

$$\Rightarrow \quad E(n) = E_0 + \sum_{i=1}^{3}\left[\sum_{k=0}^{n}\Delta T \cdot f_i(k)\left(Sat_2(\dot{x}_{tdi}^{*}(k)) + Sat_3(\dot{x}_{di}(k)) + \frac{f_i(k)}{\alpha_i(k)}\right)\right]. \tag{2.4.20}$$

since energy is transferred to the plant only when $\dot{x}_{di} < 0$. Using Eqs. 2.4.11 and 2.4.13, we can reduce the above expression to

$$E(n) = E_{obs}(n) + \sum_{i=1}^{3} \frac{f_i(n)^2}{\alpha_i(n)} \Delta T . \tag{2.4.21}$$

Case 1: $E_{obs}(n) \geq 0$

In this case, from Eq. 2.4.16, $\dfrac{1}{\alpha_i(n)} = 0$.

$$\therefore \quad E(n) = E_{obs}(n) \geq 0 . \tag{2.4.22}$$

Case 2: $E_{obs}(n) < 0$

In this case, from Eq. 2.4.16, $\dfrac{1}{\alpha_i(n)} = -\dfrac{E_{obs}(n)}{\Delta T \cdot f_i(n)^2} \cdot r_i(n)$. Substituting this expression into

Eq. 2.4.21,

$$E(n) = E_{obs}(n) + \sum_{i=1}^{3} -\frac{E_{obs}(n)}{\Delta T \cdot f_i(n)^2} \cdot r_i(n) \cdot \Delta T \cdot f_i(n)^2 . \tag{2.4.23}$$

$$\Rightarrow \quad E(n) = E_{obs}(n) - \left[E_{obs}(n) \cdot \sum_{i=1}^{3} r_i(n) \right] . \tag{2.4.24}$$

From Eq. 2.4.17,

$$\sum_{i=1}^{3} r_i(n) = 1 . \tag{2.4.25}$$

$$\therefore \quad E(n) = 0 . \tag{2.4.26}$$

Hence, it can be concluded from Eqs, 2.4.22 and 2.4.26 that

$$E(n) \geq 0 \quad \forall n , \tag{2.4.27}$$

which ensures passivity of the system.

Servo Loop Controller

The servo controller is a PI velocity controller. The actuator input for the ith finger is

determined using the following relation:

$$v_i = K_{proi}(\dot{x}_{dpi} - \dot{x}_i) + K_{inti}\int(\dot{x}_{dpi} - \dot{x}_i)\,dt\,. \qquad (2.4.28)$$

K_{proi} and K_{inti} are the proportional and integral control gains. The actuator input vector is

$$\mathbf{v} = \begin{bmatrix} v_1 & v_2 & v_3 \end{bmatrix}^{T}. \qquad (2.4.29)$$

Actuator velocities $\dot{x}_i$ (Eq. 2.4.28) are computed using approximate differentiation of the position signals. It is known that collocated PD position control (equivalent to PI velocity control) with approximate velocity signal is passive [36]. This ensures passivity of the servo loop controller.

Choice of E_0

In [31], for a collocated PID controller, E_0 is chosen as follows:

$$E_0 = \frac{1}{2}\sum_{i=1}^{3} K_{pi}e_i(0)^2\,, \qquad (2.4.30)$$

where $e_i(0)$ is the initial position error. The idea behind this choice is that, PID controller simulates a spring-damper with an effort source. Proportional control action represents a spring, Derivative control action represents a damper and the integral control action represents an effort source. E_0 is chosen as in Eq. 2.4.21 since spring is the only energy storage element.

Since the outer loop controller in Fig. 2.4.1 is noncollocated, some of the energy supplied by the robotic fingers for target position control is stored in the elastic medium of the object. Hence the choice of E_0 has to accommodate this energy storage. The proposed choice of E_0 is

$$E_0 = \frac{3}{2}\overline{K}x^2 + \frac{1}{2}\sum_{i=1}^{3} K_{pi}e_i(0)^2\,, \qquad (2.4.31)$$

where $\overline{K}$ is the estimated minimum stiffness of the object. x is the average compression of the object at the contact points at steady state. Noting that

$$\frac{1}{2}\sum_{i=1}^{3}K_{pi}e_i(0)^2 << \frac{3}{2}\overline{K}x^2 , \tag{2.4.32}$$

E_0 is chosen as

$$E_0 = \frac{3}{2}\overline{K}x^2 . \tag{2.4.33}$$

E_0 is the initial energy stored in the outer loop controller. During target manipulation, this energy is transferred to the elastic medium of the deformable object. The energy stored in the elastic medium is used in restoring the object to its original state when robotic actuation is disabled (Some energy is obviously dissipated in the process). Note that accurate model information is not required for determining E_0. A rough estimate of the stiffness is sufficient in choosing $\overline{K}$. It is fairly simple to obtain such an estimate using straightforward system identification techniques. Choice of E_0 does not affect passivity (and stability) of the system, it only affects performance of the controller in minimizing target position error.

The implicit assumption in the above discussion is that there exists a kinematic coupling between the contact points and the target. More specifically, we assume that applying external control force (at the contact point) in a particular direction causes the target to move in a direction that has positive projection along the direction of force. This assumption is generally valid for continuous media, however inhomogeneous. Inhomogeneity might cause the target to deflect away from the direction of force application, but continuity of the medium ensures kinematic coupling. Weak coupling (when the target is located away from the line of action of the fingers or due to inhomogeneity in the tissue) may necessitate larger external forces to position the target but theoretically this does not undermine the control

framework. Controllability issues related to handling of deformable objects have been investigated in [37]. A deformable object (in some cases, inhomogeneous with nonlinear properties) is an infinite dimensional system and there does not exist a general result for establishing controllability. Therefore, the approach presented here does not guarantee convergence of the target to the desired position. However, the controller does ensure stability of the system irrespective of the plant properties. This is important in safety critical applications such as breast CNB.

CHAPTER III

ROBOTIC IMAGE GUIDED BREAST BIOPSY SYSTEM

Breast cancer is the most common cancer among American women and the second leading cause of cancer death in women. In 2008, the American Cancer Society (ACS) estimates 182,460 (26% of all female malignancies) new breast cancer cases with 22% mortality rate [38]. Early detection of breast cancer has been proven to reduce mortality by about 20% to 35% [39]. Histopathological examination is considered to be the "Gold Standard" for definitive diagnosis of cancer but requires tissue samples that are collected through biopsy. Of the two major approaches for breast biopsy, needle biopsy and open excisional biopsy, needle biopsy is more attractive because it is less traumatic, produces little or no scar, allows quicker recovery, and is less costly. Despite many benefits of needle biopsy, there are significant technical challenges concerning accurate steering and precise placement of a biopsy needle at the target in the breast. To successfully remove a suspicious small targeted lump various issues must be addressed, such as architectural distortion and target deflection during needle insertion and poor maneuverability of the biopsy needle. These issues are even more important when the collection of a large and intact core becomes necessary for histopathological diagnosis. Although mammography, sonography, and magnetic resonance imaging (MRI) techniques have significantly improved early detection of breast cancer, accurate placement of a biopsy needle at the target location and reliable collection of target tissue remain challenging tasks.

There are two major problems to be addressed to improve the accuracy and reduce the

difficulty of obtaining tissue samples during breast CNB.

1) Target mobility: As discussed in Chapter I, during needle insertion, complex tissue of the breast induces the small target to deflect away from its original location. Fig. 3.1 [2]

(a)

(b)

(c)

(d)
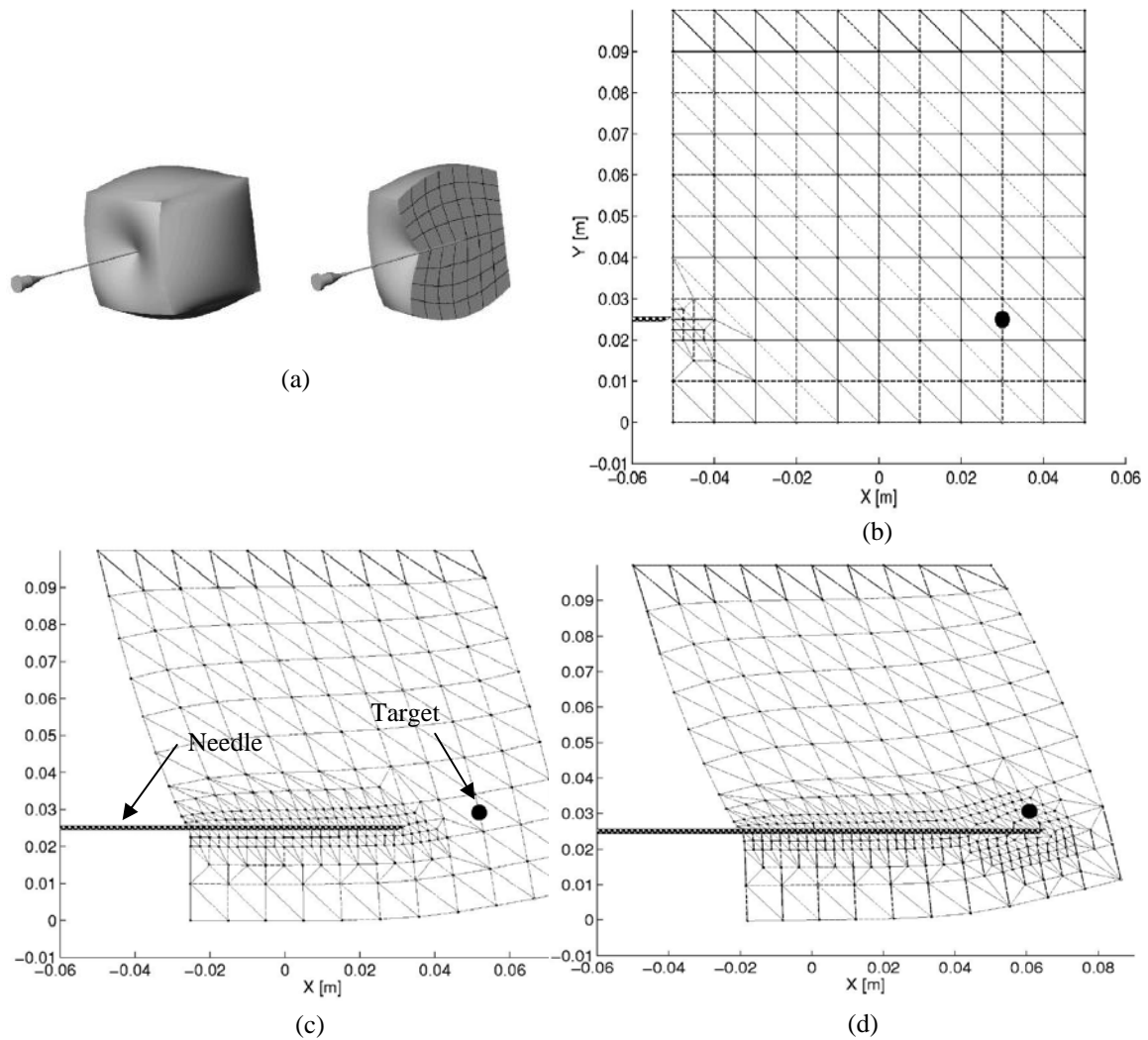
Fig. 3.1. Finite element modeling of needle insertion in elastic tissue [2].

shows a 3D finite element model of needle insertion that estimates the force distribution along the needle shaft. It can be observed from Fig. 3.1.b that the target is initially located on the line of insertion of the needle. As the needle is inserted, large tissue deformation causes

28

the target to move away from the line of insertion of the needle (Fig. 3.1.d). In Fig. 3.1.d, error between needle and target position is approximately 5 mm.

2) Difficulty of operation: Needle biopsies are guided by stereotactic mammography, MRI or two dimensional (2D) ultrasound (US). 2D Sonography is a widely used imaging technique because of its real-time capability and cost-effectiveness [40]. The current state-of-the-art US guided biopsy technique is highly dependent on the skill of the clinician [41]. A clinician performs this procedure by holding the US probe with one hand and inserting the needle with the other hand. Since sonography only provides a 2D image, if the target moves out of plane of the transducer, the clinician has to continuously reorient the probe to keep the needle and the target in the imaging plane while inserting the needle. It is critical to orient the imaging plane parallel to the needle, otherwise a false impression of the needle tip causes sampling errors [42]. This freehand biopsy procedure requires excellent hand-eye coordination. Since stabilization of the breast is problematic [43] and steering of the needle inside the breast is extremely difficult, many insertion attempts are required to successfully sample the target tissue. This may cause architectural damage to the tissue, excessive bleeding obscuring the guiding images, clinician fatigue and patient discomfort. More importantly, especially for small lesion, false negative may be assessed due to inaccurate biopsy.

As can be seen from the above discussion, a robotic breast biopsy system can help the clinician and address the above-mentioned problems by: 1) providing a mechanism that stabilizes the breast and minimizes needle – target misalignment; 2) developing an automated image acquisition system that can be coupled with the needle insertion procedure; and 3) coordinating image acquisition, needle insertion and target movement compensation. Such a robotic platform has the potential to improve speed of biopsy, minimize the need for multiple

insertions, reduce clinician fatigue and patient discomfort, and in general, reduce cost of biopsy. Additionally, by improving accuracy of biopsy, it will potentially enhance diagnostic value by reducing false negative results.

Review of Interventional Robotic Systems

Techniques to compensate for needle – target misalignment

Currently there are several methods for performing needle biopsies. These methods differ in the size of the tissue samples obtained and the mechanism for obtaining the samples. Three common methods for obtaining core tissue samples are: core needle biopsy, vacuum assisted biopsy and large core biopsy. Commercially available Bard® Biopty-cut® [44], Mammotome® [45] and ABBI® (Advanced Breast Biopsy Insturmentation) [46] systems are used (respectively) to perform these procedures.

The above commercially available biopsy instruments do not compensate for target movement during needle insertion. Several groups have designed robotic systems to improve the accuracy of needle insertions [47]-[52]. The reader is referred to [47] for a detailed review of state-of-the-art in interventional robotic systems. In [48], a remote controlled robotic device for conditioning of the breast and positioning of the biopsy probe is presented. A robotic system for precise positioning and insertion of the biopsy needle along a desired path is presented in [49]. This robot has seven passive degrees of freedom (DOF) for precise positioning and three active DOF for accurate needle insertion. An image guided robotic system for precise intratumoral placement of therapeutic agents to eliminate cancer cells is proposed in [50]. Robotic systems have been developed for performing spinal [51] and renal

[52] percutaneous procedures. These systems [50] - [52] use the robot developed in [49] for needle insertion. "Although these innovations greatly improve accuracy by automating needle target alignment, they do not provide active trajectory correction in the likely event that trajectory errors arise" [6]. Needle trajectory errors and target mobility result in multiple insertions at the same biopsy site for accurate sampling. In addition, such sampling errors may increase false negative results.

As a result, significant research effort is being made to investigate techniques that can address the problem of target movement during needle insertion. As discussed in Chapter I, steerable needle devices [6]-[8], visually controlled needle guidance systems [9], finite element based preplanning techniques [10][11] have been developed to minimize needle – target misalignment.

Robotic systems for US image acquisition

Researchers have developed robotic systems to alleviate the difficulty associated with acquiring US images during medical procedures. A force controlled robotic manipulator for performing cardiovascular 3D US image acquisition has been presented in [53]. Teleoperated master/slave robotic systems have been developed that enable remote acquisition of US images [54][55]. A needle driver robot is presented in [56] where two degrees of freedom (DOF) in the US image plane are controlled through visual servoing. In this approach the needle is constrained to lie in the US image plane for visual feedback. This idea is extended in [57] where the controlled instrument is not constrained to lie in a plane but has to intersect with the US image plane. An image guided robot for positioning the US probe and tracking a target in real-time has been developed for diagnostic US [58]. The robot controller, US image

processor and the operator have shared control over the robot for guiding the US probe.

Even though these systems greatly reduce the difficulty of acquiring US images, the target cannot be tracked in real-time if it moves out of the imaging plane of the probe. [59] presents a speckle decorrelation technique for estimating out-of-plane motion of a target. This is a very interesting approach but simulation results presented assume rigid motion of internal tissue to preserve correlation between successive image planes. Due to needle insertion and target manipulation, large tissue deformation occurs inside the breast which prohibits application of this technique.

One of the limitations of US based imaging is that the US probe has to be continuously in contact with the surface of the breast to ensure acoustic coupling. Force sensors are typically used to ensure contact between the tissue surface and the US probe [53][55][58].

The goal of the current research is to address many of the technical challenges associated with needle breast biopsies leading to the design and development of an innovative robotic breast biopsy system named RIBBS (Robotic Image-guided Breast Biopsy System) to aid the clinician during the biopsy procedure. RIBBS can aid the operating clinician in 1) acquiring US images; 2) compensating for target deflection and; 3) coordinating needle insertion, image acquisition and target movement compensation. RIBBS will potentially overcome a number of challenges in needle biopsies (as discussed earlier) and will allow the clinician to solely focus on the detection, decision making, and collection of the tissue sample without being encumbered by the difficulty of achieving good targeting accuracy, in addition to, coordinating needle insertion, breast stabilization, US image monitoring and US probe manipulation. It is evident from the literature review that there does not currently exist a robotic system that addresses the above-mentioned problems to provide comprehensive

assistance during breast CNB.

The specific subsystems that will lead to the development of RIBBS are:

1) Mechanism to compensate for needle – target misalignment for providing access to mobile lesions.

A novel approach based on "robotic manipulation" (developed in Chapter II) is used to position the target inline with the needle thereby minimizing error in needle – target alignment. This approach is fundamentally different from techniques presented in literature such as needle steering, finite element based preplanning etc. The real-time manipulation system presented here is a set of position controlled robotic fingers. These fingers are placed around the breast during the needle insertion procedure. They control the position of the target, by applying forces on the surface of the breast, such that the target is placed inline with the needle. The idea is to design a controller that minimizes the tracking error in the position of the target. In this approach, needle insertion force is treated as a disturbance to the system.

2) Image acquisition system for dynamic tracking of the location of a target in real-time using a 2D US probe.

A new US-based image acquisition system is developed that imparts autonomous mobility and searching capability to a traditional clinical US probe. The robust image acquisition technique developed in this work is capable of automatic search and recovery of the target should it go out of the imaging plane. Currently, none of the existing systems have this ability. A novel sensorless contact detection technique is also developed that reliably detects contact transitions (between US probe and tissue surface) based on US image data.

3) Integrate the above subsystems for a semi-automated modality of breast biopsy.

To coordinate robotic manipulation, US imaging and needle insertion, a hybrid supervisory controller is developed to provide comprehensive assistance during needle breast biopsy procedures.

Design of Robotic Image-Guided Breast Biopsy System

Robotic Image-guided Breast Biopsy System (RIBBS) is designed with the following objectives: (a) to manipulate the position of the target to compensate for target mobility; b) to automate real-time tracking of the target using a US probe; and (c) to integrate a needle guidance device with the manipulation mechanism and US image acquisition system.

RIBBS is designed for prone position breast biopsies. Conventional US guided breast biopsies are performed with the patient in a supine position. This position is preferred by the clinicians for freehand US guided breast biopsies since it provides easy access for the US probe to be manually placed and maneuvered over the breast, allows clinician to manually stabilize the breast and insert the needle. On the other hand, where imaging and stabilization are automated and needle insertion is aided by a mechanism, such as stereotactic breast biopsies, the biopsies are performed with the patient in a prone position lying on a table with the breast projecting through an opening in the table. The biopsy procedure is then performed under the table, after raising it to gain access to the patients' breast. Although prone position biopsies require a dedicated biopsy table that incurs cost, prone position is chosen for US guided biopsies for several reasons. A vast majority of the breast cancer patients are older and they may have softer/loose breast tissue (may be pendulous breast). For these patients, breasts tend to be flattened over the chest wall when in supine position, which may create difficulty in accessing the target. Prone position, on the other hand, allows the target to move

away from the chest wall and thus makes it easier to perform robotic-assisted biopsy. Also, prone position is comfortable for the patient and it offers unobstructed access to the region of interest, and facilitates easy compression of the breast for reducing target movement during the procedure. With the patient in a prone position, vasovagal reactions and patient motion are eliminated. This also keeps the whole procedure out of patient's view, helping to make the entire intervention more comfortable and relaxed. From an engineering perspective, prone position offers maximum workspace for RIBBS with good surface contact area on the breast for the robotic fingers. Performing US guided biopsy procedure with the patient in a prone position will not cause operational inconvenience to the clinician since breast stabilization, target movement compensation and image guidance are automated using RIBBS. It will not compromise the advantages of US guided biopsy such as real-time feedback, much less preplanning about needle-target alignment (e.g., in comparison to stereotactic biopsy), and cost-effectiveness.

Design of Robotic Manipulation Mechanism

During the biopsy procedure, needle is inserted into the breast at a shallow angle (away from the chest wall) to the horizontal plane containing the target. Needle incision site and orientation of the needle are chosen by the clinician considering factors such as location of target, location of critical anatomical structures and ease of access to target. Desired target position is the point where the line of insertion (of the needle) intersects the plane containing the target. While one can choose any plane that contains the target and has an intersection with the line of needle insertion, this plane is chosen to be the horizontal plane for simplicity. The desired target position is determined by a planner based on the actual target location and

needle orientation. Note that planar (horizontal plane) target position control is sufficient to be able to successfully position the target along the line of insertion of the needle.

The overall design requirements for the manipulation mechanism are:

1) As discussed in Chapter II, planar manipulation of deformable objects requires three robotic fingers with a geometric arrangement such that the end points of their force direction vectors draws a non-zero triangle that includes their common origin point.

2) Design should facilitate easy access to needle insertion instrument and US image tracking device.

3) Force applied by the fingers should be limited to avoid injury to the patient.

4) Mechanism should be adjustable to accommodate different breast sizes.

5) Mechanism should be compact.

6) It should be easy to clean and decontaminate.

7) Mechanism should be inexpensive.

Based on these requirements, manipulation mechanism is designed as shown in Fig. 3.2.1.1. Fig. 3.2.1.2 shows a perspective view of the manipulation mechanism. Fig. 3.2.1.3 shows a view (View A) of the manipulation mechanism along the direction indicated by the block arrow in Fig. 3.2.1.2. In Fig. 3.2.1.1, clear block arrows represent passive degrees of freedom and shaded block arrows represent degrees of actuation.

The system consists of a rotary base that can rotate about the central vertical axis (P1). The rotary base has a detent locking mechanism that can be used to lock the entire system at eight different positions (45^0 intervals). Actuator base is connected to the rotary base with three telescoping links. The telescoping links can be used to move the actuator base vertically (P2). These links provide a range of motion of 122 mm. The telescoping links can be fixed using a

36

locking pin. These two DOF provide flexibility in positioning the device for convenient access based on location of the target and needle incision site.
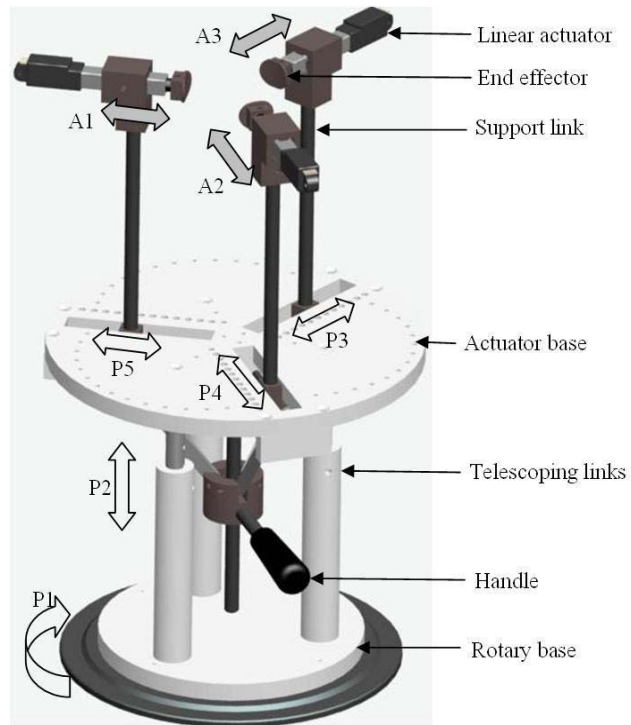
Fig. 3.2.1.1. Design of manipulation mechanism.
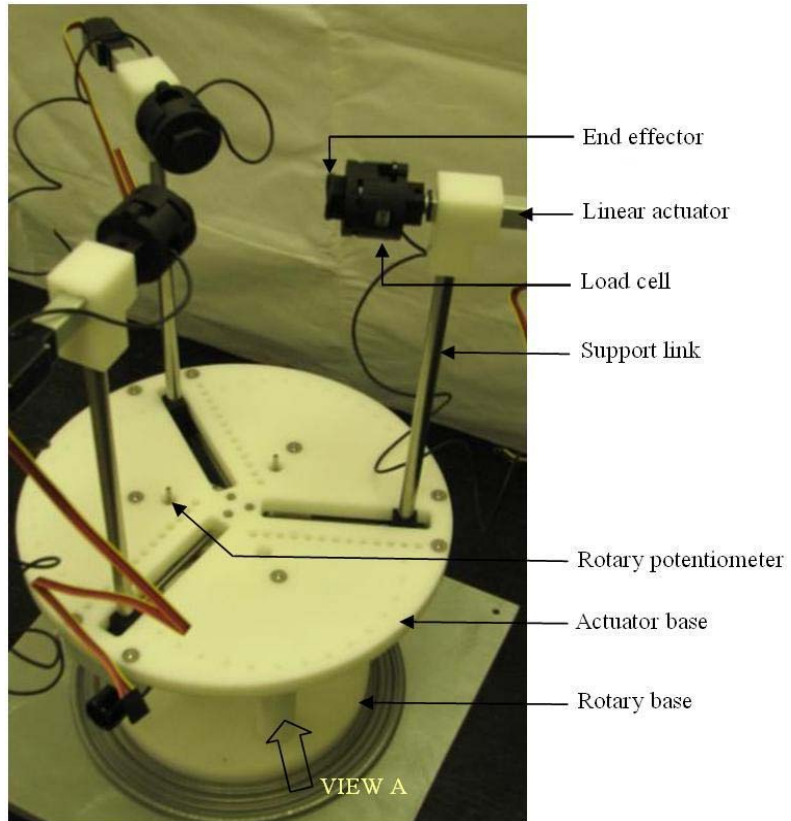
Fig. 3.2.1.2. Perspective view of manipulation mechanism.
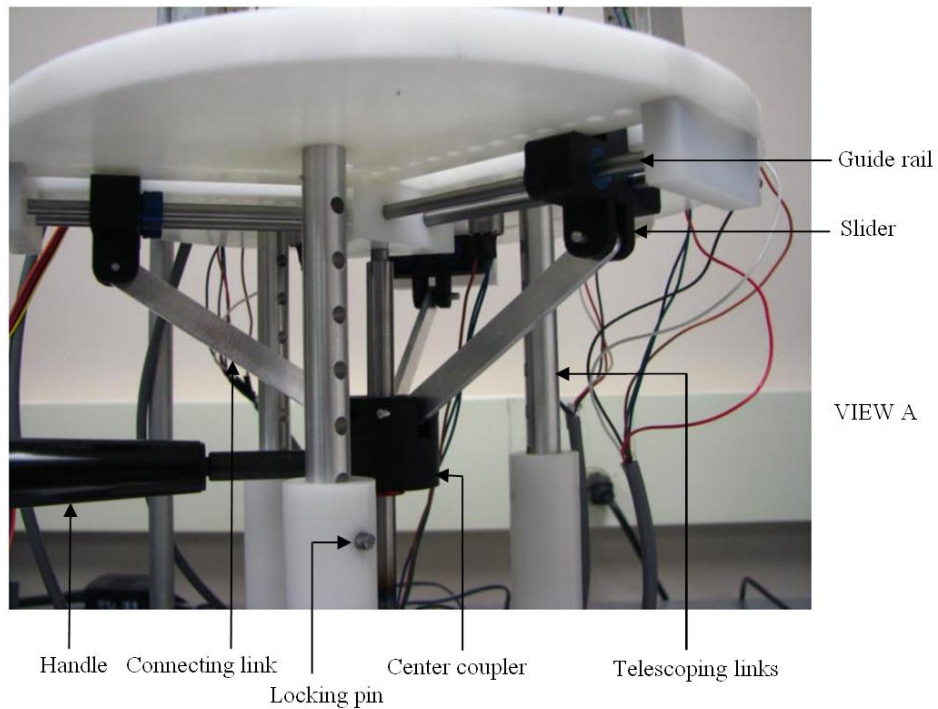
Fig. 3.2.1.3. (View A) Mechanism for coupled radial motion of robotic fingers.

The robotic finger for applying force on the breast consists of a lead screw driven linear actuator, end effector and load cell. The miniature linear actuator (L12-50-210-12-P, Firgelli Technologies Inc) is a DC motor driven lead screw with a gear ratio of 210:1. They are light weight (weight 37 g, dimensions 18 mm X 15 mm X 115.5 mm) having a stroke of 50 mm and a force capability of 45 N (at a speed of 2.5 mm per second). The end effector is a contoured link that can apply compressive, frictionless force on the breast. A load cell (MSP6948-ND, Digikey) is mounted between the end effector and linear actuator to measure the force applied by the finger. Three fingers are positioned 120^0 apart to satisfy conditions of the theorem discussed in Chapter II.

The finger mechanisms are mounted on support links which are attached to sliders underneath the actuator base. A handle can be used to move the center coupler vertically. Vertical motion of the center coupler can be transformed into coordinated radial motion (P3, P4, and P5) of the sliders through the connecting links. Radial motion of the fingers is used to accommodate different breast sizes. The finger mechanisms can be moved 100 mm radially.

The robotic fingers have a cylindrical workspace of 2209 cm^3 (12.5 cm height and 7.5 cm radius). The system has a footprint of 2027 cm^2 and overall height of 49 cm. It has three degress of actuation (A1, A2 and A3) and three degrees of freedom (P1, P2 and coupled P3, P4, P5). The mechanism is compact and its open structure facilitates easy positioning and access for needle insertion instrument and US image tracking device. The mechanism is designed using off-the-shelf components and easy-to-machine parts to minimize cost.

Design of Autonomous Image Acquisition System

This section presents the design of a system for autonomous positioning of the US probe that can dynamically track the location of a target inside the breast.

Design requirements for this system are:

1) The device should be developed for a 2D US probe that is currently used for US-based breast biopsies.

2) It should maintain contact between the US probe and the surface of the breast for acoustic coupling.

3) It should have ability to move the US probe in a 2D plane that is perpendicular to the imaging plane of the probe to recapture the target image if the target deflects away from the original imaging plane.

4) It should be compact.

Based on these requirements, a design for the autonomous image acquisition system is developed as shown in Fig. 3.2.2.1. In Fig. 3.2.2.1, clear block arrows represent passive degrees of freedom and shaded block arrows represent degrees of actuation.

The US probe is mounted on an end-effector that has two DOF (P7 and P8). The imaging plane of the US probe is the u-v plane. The end-effector can rotate about u (P7, range of motion 69^0) and v (P8, range of motion 70^0) axes for orienting the US probe such that the imaging plane is parallel to the needle. The end-effector is driven using a two DOF cartesian robot. Vertical motion (A5) is achieved using a lead screw driven linear actuator. The miniature linear actuator (L12-30-210-12-P, Firgelli Technologies Inc) is a DC motor driven lead screw with a gear ratio of 210:1. The actuator is light weight (weight 37 g, dimensions 18 mm X 15 mm X 95.5 mm) having a stroke of 30 mm and a force capability of 45 N with

maximum speed of 2.5 mm per second. The actuator is mounted inside a telescoping link that provides additional adjustability in vertical positioning of the US probe (P6, range of motion 42 mm). This mechanism is mounted on a slide that is moved using a lead screw mechanism for horizontal motion (A4, range of motion 55 mm). The lead screw mechanism is driven using a DC motor (no load speed 7800 rpm, maximum torque 5 mNm; 2224012SR, Micromo Electronics Inc) with a worm gear drive (reduction ratio 45:1; S1C83Z-P048B090D, SDP/SI).

If the probe is not in contact with the breast, the US probe is moved along A4 to make contact with the breast. The system can also slide the US probe using the linear actuator (A5) for tracking the location of a target if it moves out of the imaging plane (u-v). US gel (Clear image high viscosity US gel, Cone Instruments) is used for coupling between the probe and the phantom. The gel also acts as a lubricant for smooth sliding along the surface. This system has two degrees of actuation (A4, A5) and three degrees of freedom (P6, P7, P8). All joint coordinates are measure using rotary and linear potentiometers.

Fig. 3.2.2.1. Design of image acquisition system.

Fig. 3.2.2.2. Image acquisition system.
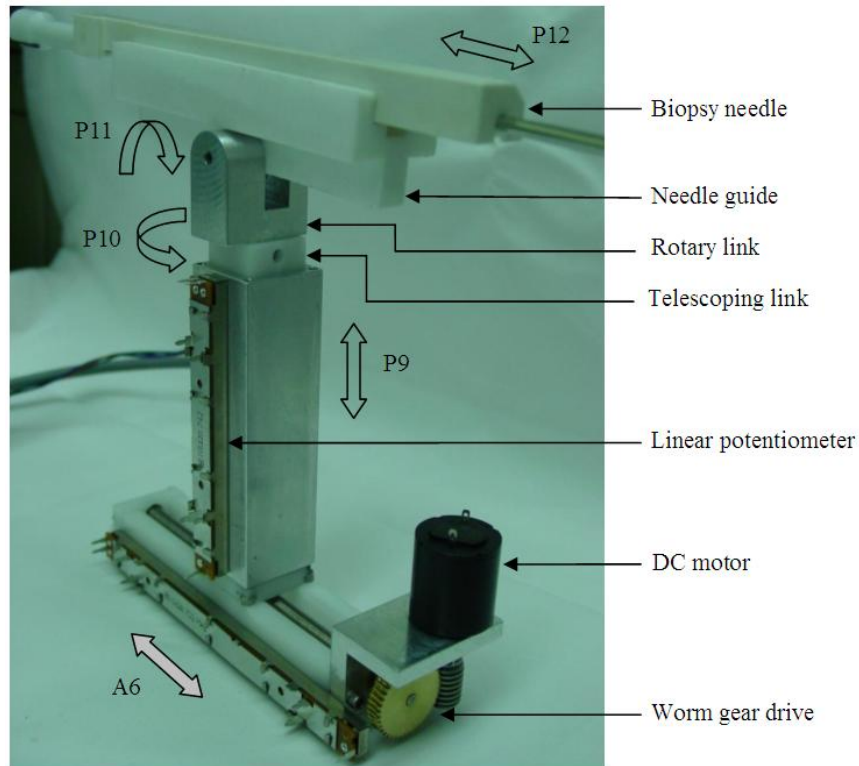
Fig. 3.2.3.1. Needle guidance device.

Fig. 3.2.3.1 shows a needle guidance platform which facilitates positioning and orienting of the biopsy needle based on location of lesion and other critical anatomical structures. The system has four degrees of freedom (P9, P10, P11, P12) and one degree of actuation (A6). All joints of the system are equipped with potentiometers for determining needle orientation. Essentially, this platform is capable of positioning and orienting the needle to reach any target in the breast.

The needle guide provides linear guidance (P12) for inserting the biopsy needle into the breast. The needle guide is mounted on a rotary link and can rotate (P11, range of motion 57^0) about the horizontal axis perpendicular to the biopsy needle. The rotary link is attached

to a telescoping link and rotates (P10, range of motion 50^0) about a vertical axis. The telescoping link can be moved vertically (P9, range of motion 55 mm) to adjust the height of the needle. This mechanism is mounted on a lead screw driven actuator for automated positioning (A6, range of motion 63 mm) of the needle at the desired incision site.

Integrated System

Figs. 3.2.4.1 and 3.2.4.2 show the integrated robotic breast biopsy system. The target manipulation mechanism, US image acquisition system, and needle guidance device are integrated in such a manner that the complete robotic system, RIBBS, is compact, easy to setup and operate. The image acquisition system and the needle device are mounted on the actuator base (Fig. 3.2.1.2). The actuator base has slots 120^0 apart for accommodating radial movement of the target manipulation actuators. Both the image acquisition system and the needle device can passively rotate (P14 and P15 in Fig. 3.2.4.2 respectively; range of motion 110^0) about vertical axes and thus can be placed at any angle (current configuration shows in steps of approximately 8^0) between two adjacent fingers of the target manipulation system. The center of the actuator base is chosen to be the global reference frame. Rotation of the image acquisition system and the needle device (with respect to the target manipulation mechanism) are measured by rotary potentiometers (shown in Fig. 3.2.1.2) mounted on the base. As a result, a kinematic relationship determines the global position of the image (u-v plane in Fig. 20) and the needle orientation.

The integrated system shown in Fig. 3.2.4.1 has six actuated degrees of freedom. three (A1, A2, A3 in Fig. 3.2.1.1) for the target manipulation mechanism, two for the imaging system (A4 and A5 in Fig. 3.2.2.1) and one for the needle guidance device (A6 in Fig. 3.2.3.1). The

44

system has fourteen potentiometers for measuring position coordinates of all the links. Three potentiometers measure the extension of the target manipulation actuators (A1, A2, A3 in Fig. 3.2.1.1), five potentiometers measure joint coordinates of the imaging system (A4, A5, P6, P7, P8 in Fig. 3.2.2.1) and four potentiometers measure joint coordinates of the needle device (A6, P9, P10, P11 in Fig. 3.2.3.1). Three load cells measure the force applied by the robotic fingers (Fig. 3.2.1.2). A 16 channel, 16-bit analog input board (PCI-DAS6034, Measurement Computing) is used for reading the analog data for input to the control algorithm. Analog data is sampled at a rate of 1KHz. An 8 channel, 16-bit analog output board (PCI-DDA08/16, Measurement Computing) is used for controlling the actuators. To overcome friction generated limit cycle behavior [60], pulse position modulation (PPM) is used to control the actuators. Therefore, duty cycle is the actuator input in Eq. 2.4.28. A timer chip (NE555, Texas Instruments) generates the PPM signal for driving a full bridge driver (L298, ST Microelectronics) which controls the actuator.
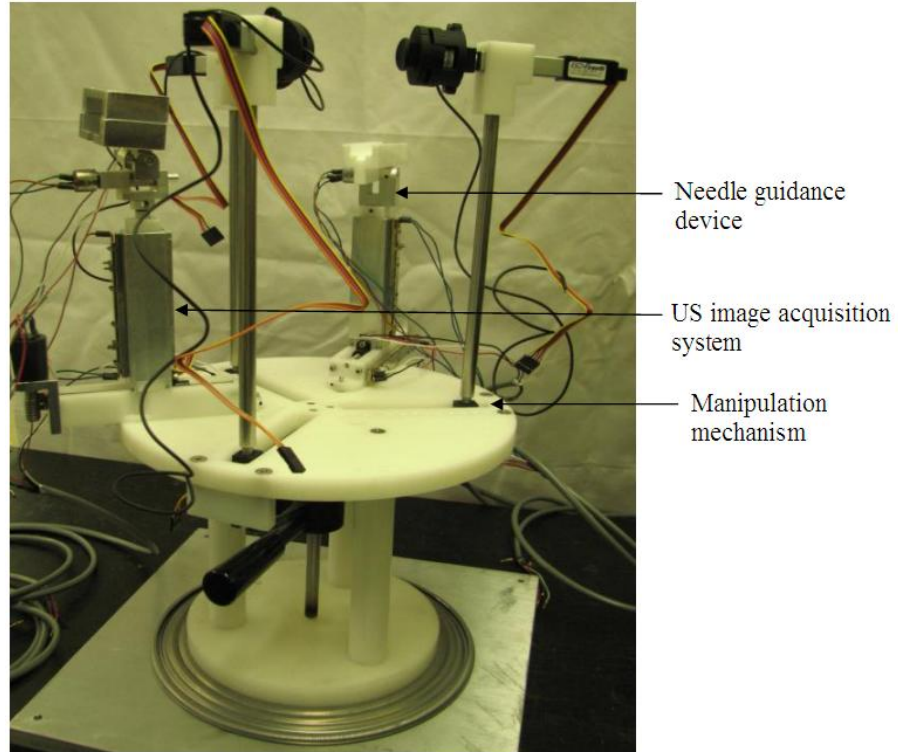
Fig. 3.2.4.1. Integrated design of RIBBS.
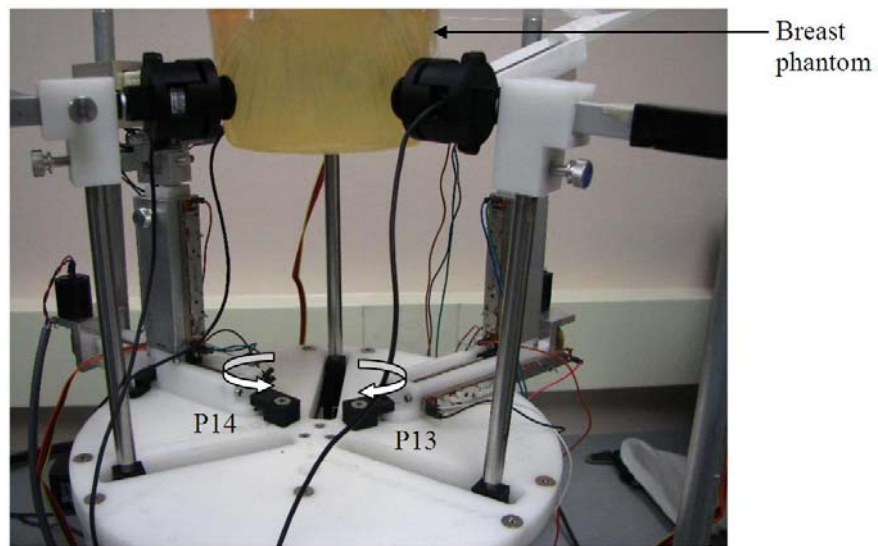
Fig. 3.2.4.2. RIBBS testbed with breast phantom.

Fig. 3.2.4.3 shows the overall architecture of RIBBS. Image frames from the US unit

(Eccocee SSA-340A, Toshiba) are sent to a computer (1.6 GHz and 2 GB RAM, shown as PC1 in Fig. 3.4.2.3) in RS-170 format. Image frames are digitized using a frame grabber card (DT3120, Data Translation) and an image processing algorithm extracts position coordinates of the target. The image processing algorithm consists of the following steps: 1) region segmentation to extract the region of interest; 2) histogram equalization; 3) thresholding to differentiate the target from the background; 4) median filtering to remove noise; 5) blob analysis to extract target centroid coordinates. Target position data is communicated serially to a microcontroller (Freescale 68HC912B32, 8 MHz clock frequency). The microcontroller outputs this data in a 16 bit parallel format. This data is read by another computer (1.6 GHz and 1GB RAM, shown as PC2 in Fig. 3.2.4.3) using a data acquisition card (PCIM DDA06/16, Measurement Computing). Each iteration of image processing and data communication requires a maximum time of 0.2 seconds. This is the time delay in the feedback loop of the controller. This computer (PC2) runs the control algorithm and outputs control signals to the motor driver circuit for driving the linear actuators.
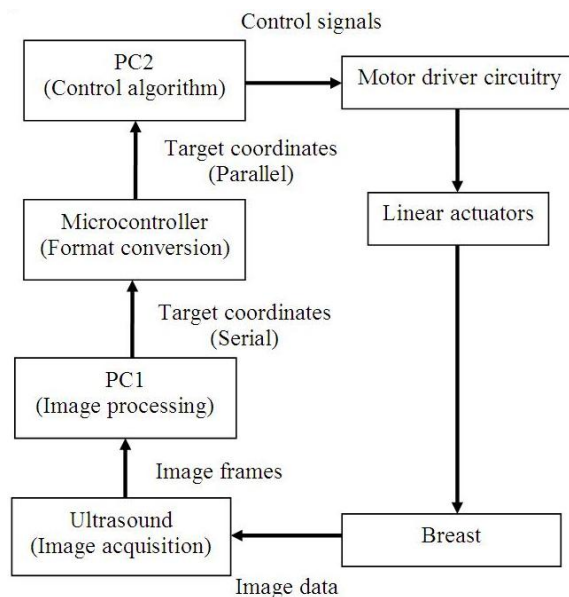
Fig. 3.2.4.3. RIBBS architecture.

47

RIBBS will be used to aid the clinician in needle biopsy. The first step is to identify the target through the US image. The US probe is positioned to identify the target on the imaging screen. Once the target is identified and located, the image acquisition system continuously tracks the target. The next step is to set the needle orientation. The needle incision site and orientation of the needle are chosen considering factors such as location of target, location of critical anatomical structures etc. The position of the needle device and the needle entry angle are manually controlled. Once the location and needle angle are chosen, the needle path is automatically determined from the sensor readings. The target manipulation controller is automatically updated with the target location information as obtained from the US image. Now as the needle is inserted and the target starts to deflect away from the needle path, the target manipulation controller computes the distance between the target and the needle path and generates appropriate controlled force to move the target back to the needle path.

Forward Kinematics of RIBBS

Needle orientation and target coordinates have to be measured with respect to a global reference frame to be able to position the target along the needle path. For this purpose, a kinematic model is developed for the system described in the preceding sections.
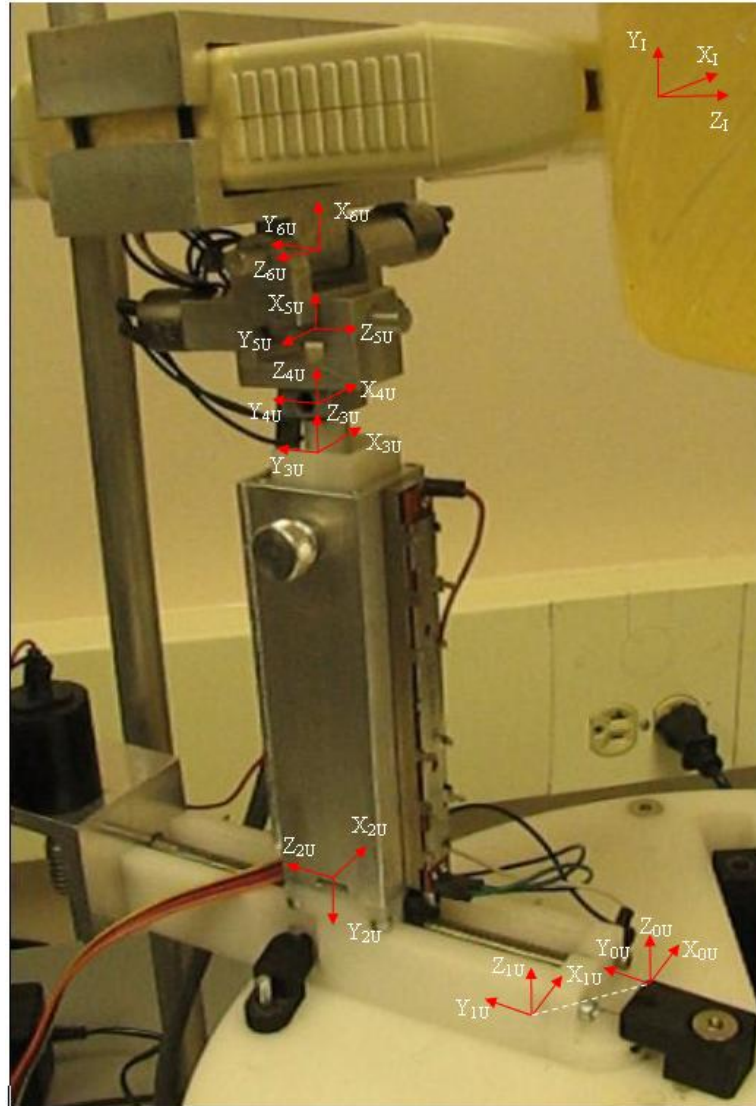
Fig. 3.3.1.1. Coordinate frame assignment for US device.

Fig. 3.3.1.1 shows the frame assignment for the US image acquisition device. The frame assignment shown in Fig. 3.3.1.1 is used to generate the Denavit-Hartenberg (D-H) parameters given in Table 3.3.1.1. The notation for the frames is that C_{iU} denotes the coordinate frame formed by the axes $X_{iU}Y_{iU}Z_{iU}$. The subscript 'iU' indicates that the frame

is attached to link 'i' (i = 1,2,3,4,5,6) on the US device. In Fig. 3.3.1.1, frames C_{2U}, C_{3U}, C_{4U} and C_{5U} are not shown in their home positions. The white dotted line joining C_{0U} and C_{1U} denotes that frame C_{1U} is located at the same point as frame C_{0U}. These D-H parameters are used to derive the forward kinematic relationship describing the position and orientation of the US image frame with respect to the local reference frame.

Table 3.3.1.1. D-H parameters for US device.

Link	Link Parameters		Joint Variables	
i	α_{i-1}	a_{i-1}	d_i	θ_i
1	0	0	0	θ_1
2	-90	0	d_2	0
3	90	0	d_3	0
4	0	0	d_4	0
5	90	0	0	θ_5
6	-90	a_5	0	θ_6

The transformation matrix between link 'i' and link 'i-1' is given by [61]

$$
{}^{i-1}_{i}T_U = \begin{bmatrix}
\cos(\theta_i) & -\sin(\theta_i)\cos(\alpha_i) & \sin(\theta_i)\sin(\alpha_i) & a_i\cos(\theta_i) \\
\sin(\theta_i) & \cos(\theta_i)\cos(\alpha_i) & -\cos(\theta_i)\sin(\alpha_i) & a_i\sin(\theta_i) \\
0 & \sin(\alpha_i) & \cos(\alpha_i) & d_i \\
0 & 0 & 0 & 1
\end{bmatrix}, \quad (3.3.1.1)
$$

where the symbols follow the standard convention. The transformation matrix of C_{6U} with respect to C_{0U} is obtained as

$$_{6}^{0}T_U = {}_{1}^{0}T_U \, {}_{2}^{1}T_U \, {}_{3}^{2}T_U \, {}_{4}^{3}T_U \, {}_{5}^{4}T_U \, {}_{6}^{5}T_U \, . \qquad (3.3.1.2)$$

The transformation matrix of the US image frame C_{IU} with respect to C_{6U} is given by

$$_{I}^{6}T_U = \begin{bmatrix} 0 & 1 & 0 & r_{14} \\ 0 & 0 & -1 & r_{24} \\ -1 & 0 & 0 & 0 \\ 0 & 0 & 0 & 1 \end{bmatrix}, \qquad (3.3.1.3)$$

where r_{14} and r_{24} are components of the translation vector. The transformation matrix of the US image frame (C_{IU}) with respect to the local reference frame (C_{0U}) is obtained as

$$_{I}^{0}T_U = {}_{6}^{0}T_U \, {}_{I}^{6}T_U \, . \qquad (3.3.1.4)$$

Forward Kinematics of Needle Guidance System

Fig. 3.3.2.1 shows the frame assignment for the needle guidance device. The frame assignment shown in Fig. 3.3.2.1 is used to generate the Denavit-Hartenberg (D-H) parameters given in Table 3.3.2.1. The notation for the frames is that C_{iN} denotes the coordinate frame formed by the axes $X_{iN}Y_{iN}Z_{iN}$. The subscript 'iN' indicates that the frame is attached to link 'i' (i = 1, 2, 3, 4, 5, 6) on the needle device. In Fig. 3.3.2.1, frames C_{2U}, C_{3U}, C_{4U} and C_{5U} are not shown in their home positions. The white dotted line joining C_{0U} and C_{1U} denotes that frame C_{1U} is located at the same point as frame C_{0U}. These D-H parameters are used to derive the forward kinematic relationship describing the position and orientation of the needle with respect to the local reference frame. The transformation matrix of C_{6N} with respect to C_{0N} is obtained as

$$_{6}^{0}T_N = {}_{1}^{0}T_N \, {}_{2}^{1}T_N \, {}_{3}^{2}T_N \, {}_{4}^{3}T_N \, {}_{5}^{4}T_N \, {}_{6}^{5}T_N \, . \qquad (3.3.2.1)$$
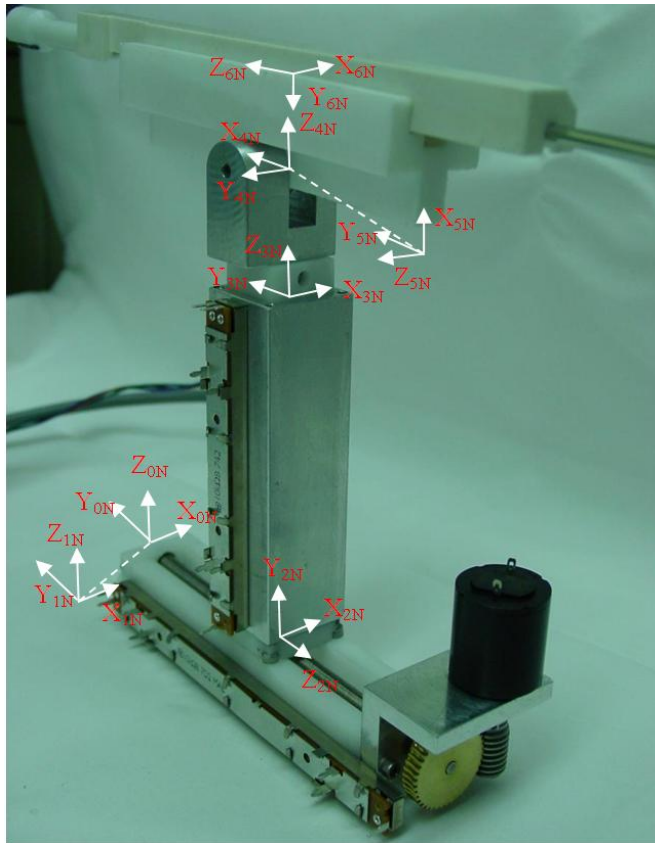
Fig. 3.3.2.1. Coordinate frame assignment for needle guidance device.

Table 3.3.2.1. D-H parameters for needle guidance device.

Link	Link Parameters		Joint Variables	
i	α_{i-1}	a_{i-1}	d_i	θ_i
1	0	0	0	θ_1
2	90	0	d_2	0
3	-90	0	d_3	0
4	0	0	0	θ_4
5	-90	0	0	θ_5
6	-90	a_5	d_6	0

Fig. 3.3.3.1 shows the reference frames for RIBBS. C_{0U} and C_{0N} are the local reference frames for the US device and the needle guidance system respectively. C_G (defined by axes $X_G Y_G Z_G$) is the global reference frame.
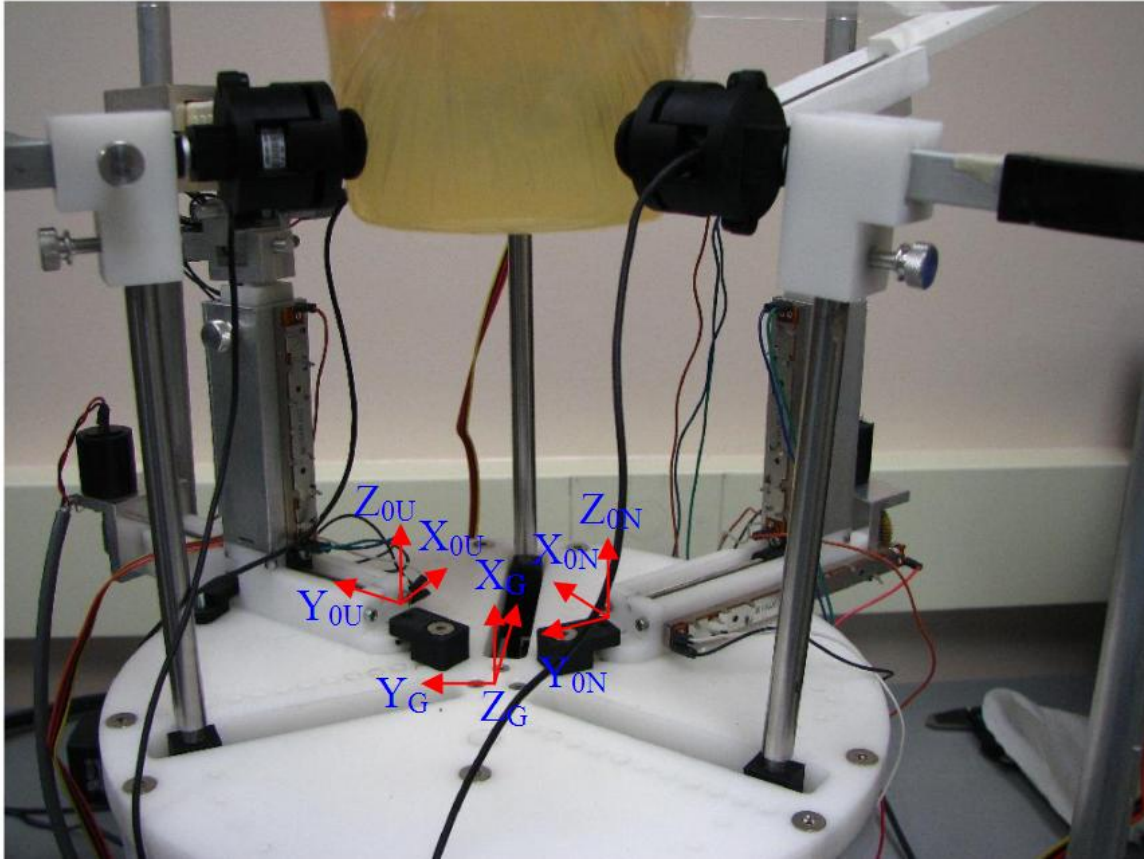
Fig. 3.3.3.1. Coordinate frame assignment for RIBBS.

The transformation matrix of the US image frame with respect to the global reference frame is given by

$$^G_I T_U = {}^G_0 T_U \, {}^0_I T_U . \tag{3.3.3.1}$$

The transformation matrix of the needle with respect to the global reference frame is given

by

$$\prescript{G}{6}{T}_N = \prescript{G}{0}{T}_N \prescript{0}{6}{T}_N . \tag{3.3.3.2}$$

The transformation matrices defining the position and orientation of the robotic fingers with respect to the global frame are not derived since the control algorithm does not require this information. However, the direction vectors (shown in Fig. 2.3.1) of the robotic fingers are defined with respect to the global reference frame.

RIBBS Control Architecture

Control system for RIBBS consists of low level controllers for the manipulation mechanism and the US image acquisition system integrated through high level hybrid supervisory control architecture. In the current system, needle insertion is performed manually using the needle guidance device. This technique leverages the expertise and skill of the clinician with the precision and consistency of the robotic system to increase effectiveness of the system. The low level controller for the manipulation mechanism is the passivity based control algorithm developed in Chapter II. In the following sections, controller for the image acquisition system and hybrid supervisory controller are developed.

Controller for US Image Acquisition System

Controller for the US image acquisition system consists of two subsystems. The first subsystem is used to track the target position in 3D and the second subsystem is used to ensure contact between the US probe and the breast surface.

Target Tracking

Tracking the location of a target (3D coordinates) using a 2D US probe requires knowledge

of the position of the probe and coordinates of the target in the image plane of the probe. Potentiometers are used to measure position and orientation of the probe. Coordinates of the target are extracted using an image processing algorithm, if the target is in the imaging plane. Presence of the target in the image plane is inferred when blob analysis (during image processing) returns atleast one object in the image frame. If the target is out of the imaging plane, there is uncertainty in determining the location of the target with respect to the imaging plane i.e., there is no information regarding the location of the target in a direction perpendicular to the imaging plane. The search strategy exhaustively searches for the target using a position controlled linear actuator. The linear actuator (A5 in Fig. 3.2.2.1) moves the US probe vertically along a desired trajectory, x_{5d}, given by

$$x_{5d} = A \, Sin(2\pi f (t - t_0)),$$ (3.4.1.1.1)

where A is the amplitude (7.5 mm), f is the frequency (1/15 Hz) and t_0 is the time (in seconds) at which target tracking is enabled.

In the interval $[t_0 \; t_0+3.75]$ the US probe is moved vertically upwards. If during this time, the target is located, the actuator stops moving to keep the target in the image plane. If the target is not located by moving along this direction, the actuator reverses and moves along the opposite direction in the interval $(t_0+3.75 \; t_0+11.25]$ to locate the target. Since typically the target movement is not greater than 10 mm, by moving the US probe 7. 5 mm in each direction (total 15 mm) the target should be detected. *A* proportional controller is used to track the desired trajectory. If for any reason, the target is not found then the above cycle is repeated until the target is detected.

Contact Detection

Due to high acoustic impedance of air, US probe has to be in contact with the breast for

imaging the target and surrounding tissue. Surface deformation due to target manipulation and needle insertion may result in the US probe losing contact with the breast. Loss of contact has to be detected and the US probe has to be moved to reestablish contact with the surface. The region in the image close to the edge (where the US probe makes contact with the surface) is used to detect the contact state of the US probe. This region is extracted from the US image and Otsu's method is used to estimate the greyscale threshold for the region. When the probe is in contact with the surface the threshold is small and when the probe breaks contact with the surface the threshold increases. This change in the threshold is used to infer the contact state of the probe. This algorithm reliably predicts contact state transitions of the probe. During biopsy procedure, if the probe breaks contact with the breast, the US probe is moved radially inwards (along A4 in Fig. 3.2.2.1) using the linear actuator to reestablish contact. This technique is used to facilitate continuous imaging of the target and surrounding tissue.

Hybrid Supervisory Controller

The fundamental theoretical framework that is used to integrate the controllers of the image acquisition system and target manipulation system is based on hybrid system theory [62]. In particular, a supervisory controller is designed that monitors and coordinates these two controllers based on discrete events. Fig. 3.4.2.1 shows a schematic of the supervisory controller (SC). The supervisory controller activates the individual subsystem controllers at any given time based on certain events that take place during the biopsy procedure.
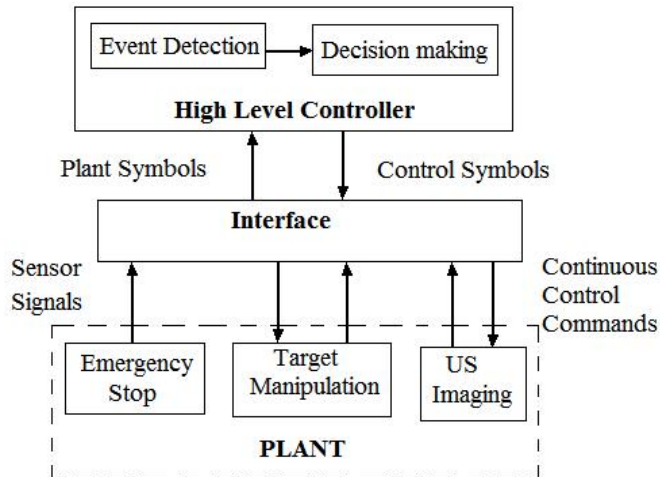
Fig. 3.4.2.1. Hybrid control architecture.

The high-level controller is a discrete-event system (DES) that includes a discrete decision process described by a finite state automaton. The proposed high level controller makes decision about the task that is required for robotic assistance during biopsy. The high-level controller and the plant (Fig. 3.4.2.1) cannot communicate directly in a hybrid control system because each utilizes different types of signals. Thus an interface is required which can convert continuous-time signals to sequences of symbols and vice versa. There has been no work on designing such a hybrid system for biopsy purposes. However, there has been some work on developing such hybrid controllers in other fields, such as industrial robotics, medicine and manufacturing [63]. In order for the high-level controller to decide the necessary control actions, the state information from the plant is observed by the process monitoring module through the interface. The interface triggers events pertinent to the task and communicates to the process monitoring block of the high-level controller. Once these events are triggered, the decision making module othe high-level controller determines what actions need to be taken in response to these events. The high-level control instructions are sent to the low-level controllers through the interface, which then executes these actions. The

proposed architecture is flexible and extendable in the sense that new events can be included and detected by simply monitoring the additional state information, and accommodated by introducing new low level controllers.

The high-level controller is a discrete-event system deterministic finite automaton, which is specified by

$$D = (\tilde{P}, \tilde{X}, \tilde{R}, \psi, \lambda) \quad [62]. \tag{3.4.2.1}$$

Here $\tilde{P}$ is the set of discrete states. Each event is represented as a plant symbol, where $\tilde{X}$ is the set of such symbols, for each discrete state. The next discrete state is activated based on the current discrete state and the associated plant symbol using the following transition function: $\psi : \tilde{P} \times \tilde{X} \to \tilde{P}$. In order to notify the low level controller the next course of action in the new discrete state, the controller generates a set of symbols, called control symbols denoted by $\tilde{R}$ using an output function: $\lambda : \tilde{P} \to \tilde{R}$. The action of the high level control is described by the following equations:

$$\tilde{p}_j[n] = \psi(\tilde{p}_i[n-1], \tilde{x}_k[n]), \tag{3.4.2.2}$$

$$\tilde{r}_c[n] = \lambda(\tilde{p}_j[n]), \tag{3.4.3.3}$$

where $\tilde{p}_i, \tilde{p}_j \in \tilde{P}, \tilde{x}_k \in \tilde{X}, \tilde{r}_c \in \tilde{R}$ represent the index of discrete states. k and c represent the index of plant symbols and control symbols respectively. n is the time index that specifies the order of the symbols in the sequence.

The high-level controller first detects state information from the plant through the interface, and then determines the actions to be taken in response to this information. The state information from the plant can be a continuous signal or a discrete value. Let S_{Mn}, S_{In} and

58

S_{En} represent the sets of robot manipulation, imaging and emergency state information respectively. In this system, the signal detected from the manipulation system is: a) Force applied by the robotic fingers (S_{Mn} is the force applied by the nth robotic finger, n = 1, 2, 3). Three signals are monitored from the US imaging system: a) Contact condition of the US probe (S_{I1}, 0 – contact; 1 – no contact) b) Presence of target in the image plane (S_{I2}, 0 – target in image plane; 1 – target not in image plane) c) Position of linear actuators for US probe movement (S_{I3} and S_{I4}). An emergency signal is also monitored to detect when the stop button is pressed (S_{E1}, 1 – no emergency; 0 – emergency stop). The emergency stop provides a mechanism for stopping the biopsy procedure incase of unexpected behavior of the robot or discomfort to the patient. In this procedure, we define the following plant states $\tilde{P}$: manipulation, contact initiation, target tracking and stop. Manipulation ($\tilde{p}_1$) implies that target manipulation is activated. Contact initiation ($\tilde{p}_2$) implies that the US probe is moved to make contact with the surface of the breast. Target tracking ($\tilde{p}_3$) implies that the search algorithm is activated to locate the target. Stop ($\tilde{p}_4$) means that the entire system is disabled.

State information from the plant is monitored to trigger relevant events to modify the task. When these events are triggered, the interface provides the necessary plant symbol ($\tilde{x}$) to the high-level controller. Currently we have defined six events for the proposed high-level controller. However, the number of events can be easily extended. Events are reset at the beginning of task execution. Additionally, the triggered event is reset when a new event occurs.

The symbols Ld_3, Ud_3, Ld_2 and Ud_2 represent lower and upper limits of the range of motion

of actuators A5 and A4 (Fig. 3.2.2.1) respectively. Let f_{maxn} represent the maximum safe

force that can be applied by the nth robotic finger. The signal S_{S1} is defined as follows:

$$S_{S1} = (S_{Mn} \leq f_{\max n}) \wedge (Ld_3 \leq S_{I3} \leq Ud_3) \wedge (Ld_2 \leq S_{I4} \leq Ud_2) \wedge (S_{E1} = 1). \quad (3.4.3.4)$$

When the force applied by the fingers is within safe limits, actuators for the US device are

within limits and emergency stop is not detected, S_{S1} is true. When any one of the above

conditions is not satisfied, S_{S1} is false. S_{S1}, S_{I1} and S_{I2} are discrete (binary) valued signals.

Based on the edges detected on these signals, events E_1 through E_6 are triggered according to

Table 3.4.2.1.

Table 3.4.2.1. Events for high level controller.

Signal	Edge	Event	Plant Symbol
S_{S1}	Rising	E_1	$\tilde{x}_1$
S_{S1}	Falling	E_2	$\tilde{x}_2$
S_{I1}	Rising	E_3	$\tilde{x}_3$
S_{I1}	Falling	E_5	$\tilde{x}_5$
S_{I2}	Rising	E_4	$\tilde{x}_4$
S_{I2}	Falling	E_6	$\tilde{x}_6$

If a rising or falling edge is detected on S_{S1}, events E_1 and E_2 are triggered respectively.

When the US probe breaks/makes contact with the surface, events E_3 / E_6 are triggered.

When the target moves out of/into the imaging plane, events E_4 / E_5 are triggered. Plant symbols are designed based on the events (Fig. 3.4.2.1).

When an event is triggered, the corresponding plant symbol ($\tilde{x}$) is generated by the interface. The current state ($\tilde{p}$) and the plant symbol ($\tilde{x}$) are used by the high-level controller to determine the next state. The control mechanism of the proposed high-level controller is shown in Fig. 3.4.2.2. The supervisory controller generates a control symbol for each state according to the following output function:

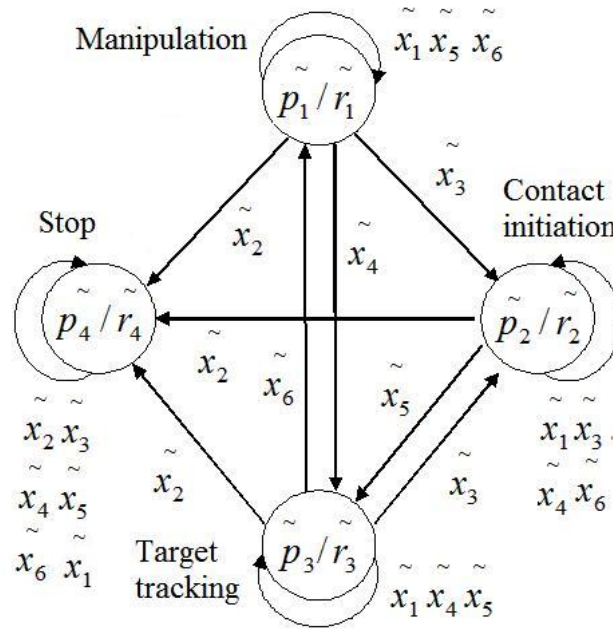$$\lambda(\tilde{p}_i) = \tilde{r}_i \quad for \quad i = 1,2,3,4 . \tag{3.4.3.5}$$

Fig. 3.4.2.2. Supervisory controller.

In this application only one state is active at a time and therefore a control symbol is uniquely assigned for each state. Any event that generates a plant symbol along with the current state information determines the next state and as a result the corresponding control

symbol. Since the low-level assistive controller cannot interpret the control symbols, the interface converts them into enable/disable signals based on the control policy. The control symbols and their corresponding control policies are given in Table 3.4.2.2.

Table 3.4.2.2. Supervisory control strategy.

Output Symbol	Control Policy
$\tilde{r}_1$	Enable target manipulation
$\tilde{r}_2$	Enable contact initiation
$\tilde{r}_3$	Enable target tracking
$\tilde{r}_4$	Disable all systems

To demonstrate the supervisory control structure in Fig. 3.4.2.2., when the current state of the system is 'Manipulation' and event E_6 is detected the control state changes to 'Target Tracking' until another event is detected. All the state transitions for the respective triggered events are shown in Fig. 3.4.2.2. An LED is used as a state indicator in the system. The state indicator shows the current state of the system to the clinician. The clinician can modify his actions based on the system state (Table 3.4.2.3) to maximize performance and eliminate injury to the patient.

As shown in Table 3.4.2.3, when the system is in the manipulation state, needle insertion can proceed as the robot can compensate for needle – target misalignment. When the system is in target tracking or contact initiation states, target coordinates are not available for the controller to compensate for needle – target misalignment. Hence, in this case it is preferred

to suspend needle insertion until contact is established or target is detected (or both). When emergency stop is activated, either due to unexpected robot behavior or patient discomfort, best protocol is to abort the biopsy procedure and retract the needle to prevent injury to the patient.

Table 3.4.2.3. Preferred clinician action based on system state.

System State	LED Status	Preferred Action
Manipulation	Off	Insert needle
Contact Initiation	On	Wait
Target Tracking	On	Wait
Stop	Blinking	Retract needle

Planner

Fig. 3.5.1 shows the control structure for the manipulation mechanism. This control structure is similar to Fig. 2.3.2. In Fig. 3.5.1, target position data ($\mathbf{P_t}$) is obtained through image feedback. The desired target position ($\mathbf{P_d}$) is determined by the planner based on the current target location and the needle path. The desired target position is always along the line of insertion of the needle. The controller acts on the position error and drives the robotic fingers to position the target at the desired location. The force exerted by the needle is the disturbance to the system. Design of the controllers is described in Chapter II. In this section, planner description is presented.

Fig. 3.5.2 shows a schematic of needle orientation and target position during breast CNB. As discussed in Chapter II, $\mathbf{P_t}$ is the actual target position, $\mathbf{P_d}$ is the desired target position and $\mathbf{e}$ is the error vector (These are 2D vectors measured with respect to the global reference frame, C_G). It can be observed from the schematic that the desired target position is along the

needle path. To facilitate ease of positioning of the robotic fingers (for satisfying Eq. 2.2.1), horizontal plane is chosen for target manipulation. Therefore, the desired target position is at the point of intersection of the needle path and the horizontal plane. So, the error vector is also located in the horizontal plane. Altitude (θ) indicates the angle between needle and the vertical. Needle is inserted at an angle to the horizontal plane to have a unique intersection point ($\theta \neq 90^0$). As shown in Fig. 3.3.2.1, C_{6N} (defined by axes $X_{6N}Y_{6N}Z_{6N}$) is the coordinate frame attached to the needle. L is the distance between the origin of the needle coordinate frame and the desired target position.
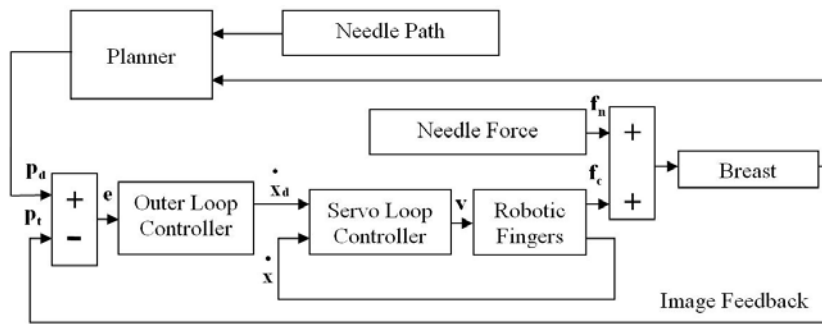

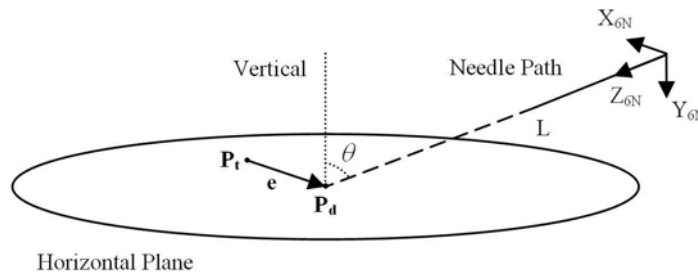Fig. 3.5.1. Control structure for minimizing needle – target misalignment.

Fig. 3.5.2. Needle – target alignment during breast CNB.

The transformation between the needle coordinate frame and the global reference frame is given by $_6^G T_N$ (Eq. 3.3.3.2). Let

64

$$
{}^{G}_{6}T_{N} = \begin{bmatrix} r_{11} & r_{12} & r_{13} & P_x \\ r_{21} & r_{22} & r_{23} & P_y \\ r_{31} & r_{32} & r_{33} & P_z \\ 0 & 0 & 0 & 1 \end{bmatrix},
\tag{3.5.1}
$$

where r_{ij}, P_x, P_y, P_z are elements of the transformation matrix. Desired target position with respect to the global reference frame is defined as

$$
{}^{G}\mathbf{P_d} = \begin{bmatrix} x_{td} \\ y_{td} \\ z_t \\ 1 \end{bmatrix}.
\tag{3.5.2}
$$

x_{td} and y_{td} are the desired target position coordinates defined in Eq. 2.4.2. z_t is the Z coordinate of the actual target position in the global reference frame. Let ${}^{6}\mathbf{P_d}$ denote the desired target position (in 3D coordinates) with respect to the needle frame.

$$
{}^{6}\mathbf{P_d} = \begin{bmatrix} 0 & 0 & L & 1 \end{bmatrix}^{T},
\tag{3.5.3}
$$

since the desired target position is at a distance L along Z_{6N} (Fig. 3.5.2). The desired target position with respect to the global reference frame is, ${}^{G}\mathbf{P_d}$, given by

$$
{}^{G}\mathbf{P_d} = {}^{G}_{6}T_{N}\,{}^{6}\mathbf{P_d}.
\tag{3.5.4}
$$

Substituting from Eqs. 3.5.1 and 3.5.3,

$$
{}^{G}\mathbf{P_d} = \begin{bmatrix} r_{13}L + P_x \\ r_{23}L + P_y \\ r_{33}L + P_z \\ 1 \end{bmatrix}.
\tag{3.5.5}
$$

Equating third element of ${}^{G}\mathbf{P_d}$ from Eqs. 3.5.2 and 3.5.5,

$$
L = \frac{z_t - P_z}{r_{33}}.
\tag{3.5.6}
$$

65

As discussed earlier, $\theta \neq 90^0$, therefore $r_{33} \neq 0$. Equating first and second elements of ${}^G\mathbf{P_d}$ from Eqs. 3.5.2 and 3.5.5,

$$x_{td} = r_{13}L + P_x .$$
(3.5.7)

$$y_{td} = r_{23}L + P_y .$$
(3.5.8)

x_{td} and y_{td} are the desired target coordinates (Eq. 2.4.2 and Fig. 3.5.1) given to the target manipulation controller for positioning the target along the needle path.

Safety

RIBBS is designed with several inherent safety features to avoid catastrophic failure or accidental injury during operation.

1) All mechanical components of the system are designed to ensure structural safety.

2) Robotic fingers have built in overload protection so that if the force exceeds 45 N, actuator shuts off to prevent injury.

3) Supervisory controller also has (software) adjustable force limits.

4) Manipulation fingers have built in limit switches to avoid over compression.

5) Range of motion of the fingers is also limited through software control.

6) Controller is designed based on passivity analysis to ensure stability of the system.

7) LED state indicator informs the clinician regarding the preferred course of action to avoid unanticipated modes of operation.

8) A panic button is integrated into the system for manual shut down in case of emergency.

CHAPTER IV

EXPERIMENTAL RESULTS

In this chapter experimental results are presented to verify and validate the system design and control technique developed in the previous chapters. Results related to elastic properties of phantoms, manipulation of phantoms using passivity based control and application of this control technique for minimizing needle – target misalignment during breast CNB are presented.

Phantom Properties

Deformable plastic phantoms are created to test the efficacy of RIBBS. Phantoms are made in such a manner that their material properties closely resemble breast tissue properties as published in the literature [12]. Breast tissue properties vary greatly based on factors such as age, presence of tissue abnormality etc. In order to demonstrate the feasibility of this technique under significant parameter variation, phantoms are prepared with varying elastic properties to demonstrate that the controller can work in realistic scenarios. This step is necessary to ensure success of the controller when it is applied during breast CNB.

The phantom is made of PVC (Poly Vinyl Chloride) plastic. Plasticizer (hardener/softener, chemical composition: phthalate ester) is added to this plastic to alter its elastic properties. Hardener increases the stiffness of plastic whereas softener decreases its stiffness. Procedure for preparing the phantoms is as follows: Plastic and plasticizer are mixed in a mold. A container in the shape of a cylinder or a truncated cone is used to mold the plastic to make

the phantom. The ratio of plastic and plasticizer is chosen to mimic breast tissue properties. Phantoms are made using a two step procedure.

1) Heating: A conventional oven is preheated to a temperature of 350^0 F and the mold is placed in the oven. Initially the mixture is milky white in color. The mixture is allowed to heat (with frequent stirring) till it turns clear (approximately 1 hour).

2) Cooling: Heated plastic is removed from the oven and the entire mixture is allowed to cool in the mold. Cooling process (between 1 -2 hours depending on volume of material) completely solidifies the plastic to form the phantom.

Uniaxial compression tests are performed on three phantoms to determine their elastic properties. A linear actuator is used to apply compressive force on the phantom. The linear actuator follows a sinusoidal motion profile. Force and position data are measured using a load cell and a potentiometer. Nominal stress – strain values are computed from force – displacement data measured during the compression test. The phantoms used in these tests are homogeneous, isotropic and incompressible. These tests are performed to determine the elastic properties of the phantoms and therefore do not contain an embedded target. Table 4.1.1 shows the specifications for the phantoms. Phantoms used in these tests are cylindrical in shape. The ratio in Table 4.1.1 is the volumetric ratio of plastic and plasticizer.

Table 4.1.1. Phantom specifications.

Phantom	Height, h (cm)	Cross Sectional Area, A (cm^2)	Plasticizer	Ratio
A	6.5	75.4	None	-
B	6.5	73.9	Hardener	19:5
C	3.0	79.1	Softener	5:2

Three trials are performed on each of the above phantoms. In each trial, sinusoidal frequency of motion of the linear actuator is different. Changing the frequency of motion varies the average actuator velocity. Strain rate of the phantom is directly dependent on the actuator velocity. Increasing actuator velocity increases the strain rate of the phantom. Table 4.1.2 shows the frequency of the actuator and the corresponding strain rate for each trial.

Table 4.1.2. Actuator motion characteristics for phantom compression trials.

Trial	Frequency of Actuator Motion (Hz)	Average Strain Rate (% / s)
1	1/25	0.86
2	1/10	2.16
3	1/5	3.78

The stress – strain curves for the phantoms are linear for all the trials. Fig 4.1.1 shows the stress – strain curves of the phantoms for Trial 1. The slope of the stress – strain curve gives the Young's modulus of the phantom. The Young's modulus is determined for the phantoms using least square curve fitting. Table 4.1.3 gives the Young's moduli of the phantoms for all trials. It can be observed from Tables 4.1.2 and 4.1.3 that increasing the strain rate increases the Young's modulus of the phantom. The change is Young's modulus for different phantoms are 9.38% (phantom A), 3.56% (phantom B) and 10.05% (phantom C).
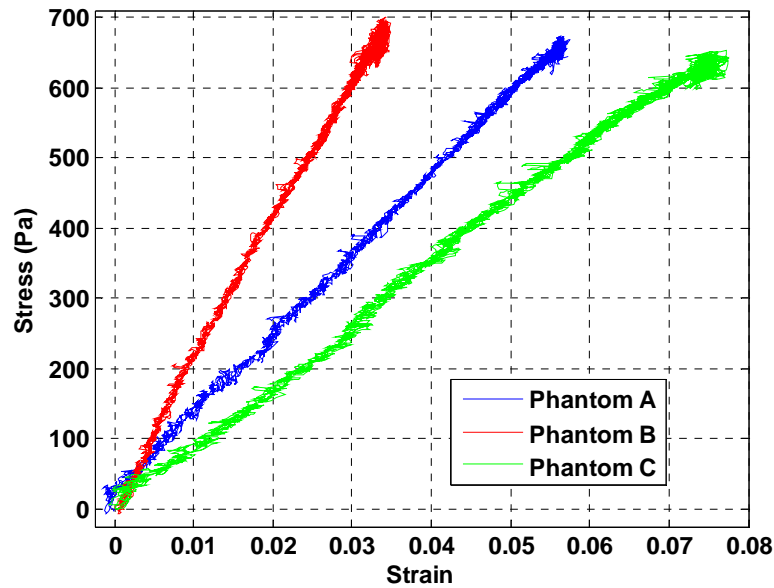
Fig. 4.1.1. Phantom stress – strain curves for Trial 1.

Table 4.1.3. Young's moduli of phantoms.

Phantom	Trial	Young's Modulus (KPa)
A	1	11.30
	2	11.82
	3	12.36
B	1	19.67
	2	19.97
	3	20.37
C	1	8.46
	2	8.69
	3	9.31

The stress – strain curve for breast tissue is exponential [12]. Therefore Young's modulus of breast tissue is dependent on strain. Table 4.1.4 shows the Young's modulus of breast tissue at four different strain values [12]. In [12], it is noted that there is slightly less than 5% change in Young's modulus for different strain rates.

Table 4.1.4. Young's modulus of breast tissue [12].

Breast Tissue	Young's Modulus(KPa)			
	Strain = 0.01	Strain = 0.05	Strain = 0.1	Strain = 0.15
Fat	4.8	6.6	10.4	17.4

Comparing Tables 4.1.3 and 4.1.4, it can be observed that the phantoms have Young's moduli similar to that of fat tissue in the breast. Therefore, the above phantoms can be used to simulate breast tissue. Inhomogeneous and nonlinear nature of the breast is mimicked by making phantoms which have asymmetric (geometrical) arrangement of different kinds of plastic material (with varying volumetric composition of plasticizer). More details regarding inhomogeneous phantoms are given in Appendix A. Several phantoms with different elastic properties are used in the following experiments. Appendix A (Table A.1) lists the phantoms and their specifications.

Deformable Object Manipulation

In this section, experimental results are presented to demonstrate the efficacy of the passivity based control technique developed in Chapter II. As discussed earlier, the basic idea is to manipulate a deformable object (phantoms are used as deformable objects) by applying external force using robotic fingers to control the position of an internal target. The target is a plastic insert placed inside the phantom during the molding process. The stiffness of the target is much greater than that of the phantom.
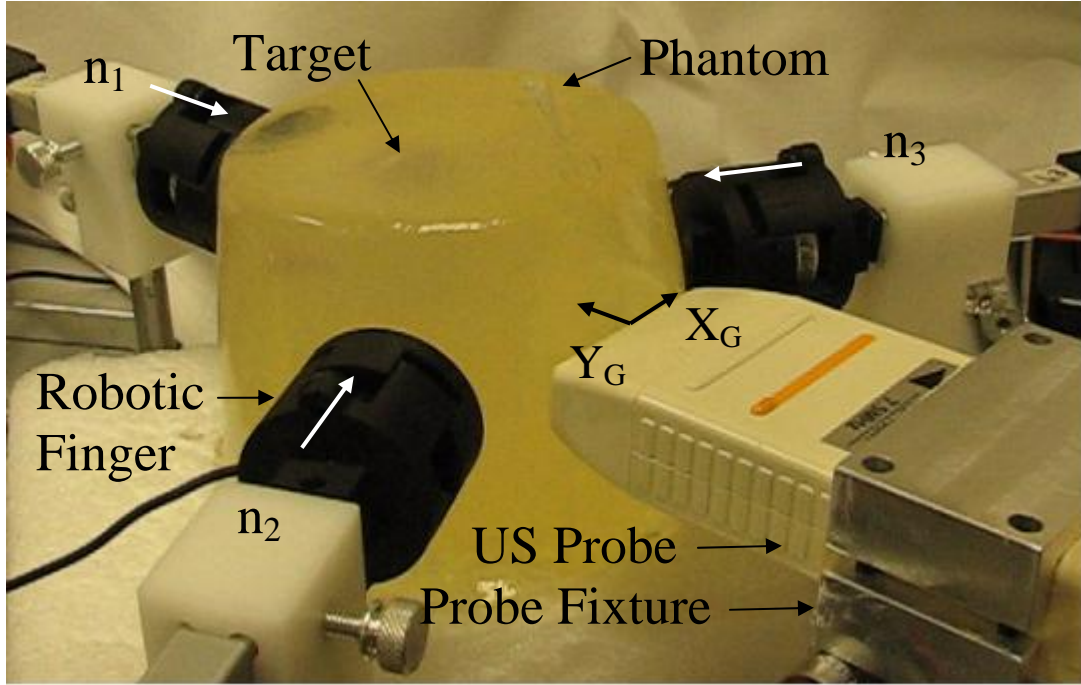
Fig. 4.2.1.1. Experimental setup for planar manipulation of phantoms.

Fig. 4.2.1.1 shows the experimental setup used for planar target position control during deformable object manipulation. As discussed in Chapter II, three robotic fingers are positioned at 120^0 interval around the phantom. A target is placed inside the phantom. Due to opacity of the phantom, the target cannot be clearly seen in the above setup. The US probe is placed in a fixture and is coplanar with the robotic fingers. Image frame of the probe is chosen as the global reference frame ($X_G Y_G$). Unit vectors defining the direction of force application by the robotic fingers are n_1, n_2 and n_3. In this setup,

$$n_1 = [0\ \text{-}1], \tag{4.2.1.1}$$

$$n_2 = [\text{-}0.866\ 0.5], \tag{4.2.1.2}$$

$$n_3 = [0.866\ 0.5]. \tag{4.2.1.3}$$

As mentioned in Chapter II, planar target manipulation is investigated in this work.

Therefore, the target movement along the vertical direction (Z_G) is not controlled. Target movement along the vertical direction is minimal and does not cause the target to move out of the image plane of the US probe.

Regulation

Several experimental results are presented to demonstrate the efficacy of the passivity based control technique for regulating the position of a target embedded in a deformable object. For regulation tasks it is desired to position the target at a specific location, denoted as $\mathbf{P_d}$. In the following experiments, the desired target position (in mm) is given by

$$\mathbf{P_d} = [x_0+3 \ y_0-3]^T. \tag{4.2.2.1}$$

$\mathbf{P_0}(x_0,y_0)$ represents the initial target position. To aid understanding and comparison, all the graphs in this section are plotted by zeroing the initial target coordinates.

For regulation tasks, desired velocity of the target is zero. Using force - displacement data from phantom compression tests, stiffness of the phantoms is determined using weighted recursive least squares. Estimated minimum stiffness of the phantoms[*] ($\overline{K}$) is found to be 525 N/m. It is observed during target position control experiments that the average compression of the phantom at the contact points is roughly 18 mm. Therefore, value of E_0 computed using Eq. 2.4.33 is approximately 0.25. Servo loop control gains K_{proi} and K_{inti} (Eq. 2.4.28) are chosen to be 0.5 and 0.05, respectively, through experimental tuning. Limits of motion of the robotic fingers, l_{imin} and l_{imax} (Eq. 2.4.10), are chosen to be 0 and 50 mm, respectively. This means that each robotic finger can compress the phantom only to the extent that the contact point moves a maximum distance of 50 mm.

---

[*] Excluding Phantom 7; See description of Experiment 4 in this section.

<u>Experiment 1 (Effect of Control Gains)</u>

This experiment demonstrates the effect of outer loop control gains (K_{pi} and K_{Ii}) on target position response. The passivity based controller is used to move the target from its initial position $\mathbf{P_0}$ to the desired position $\mathbf{P_d}$ (Fig. 2.3.1). Phantom 3 (homogeneous, see Appendix A for details) with an embedded target is used in this experiment. Fig. 4.2.2.1 shows X and Y coordinates of the target position for three sets of control gains.
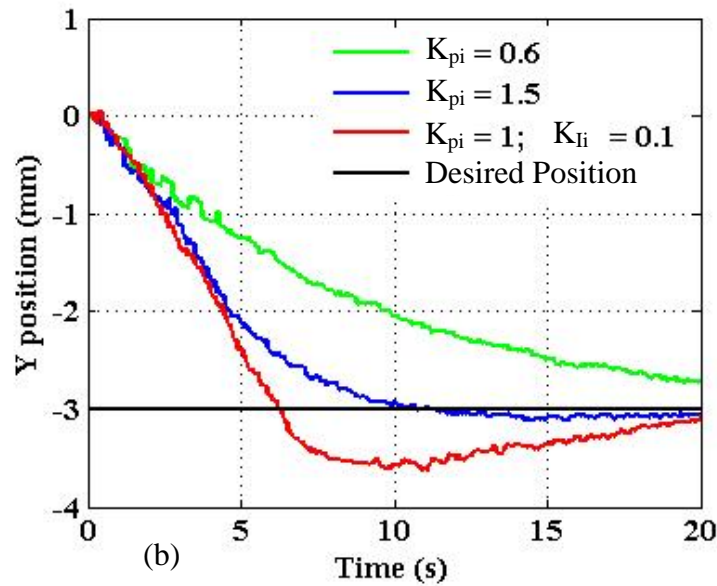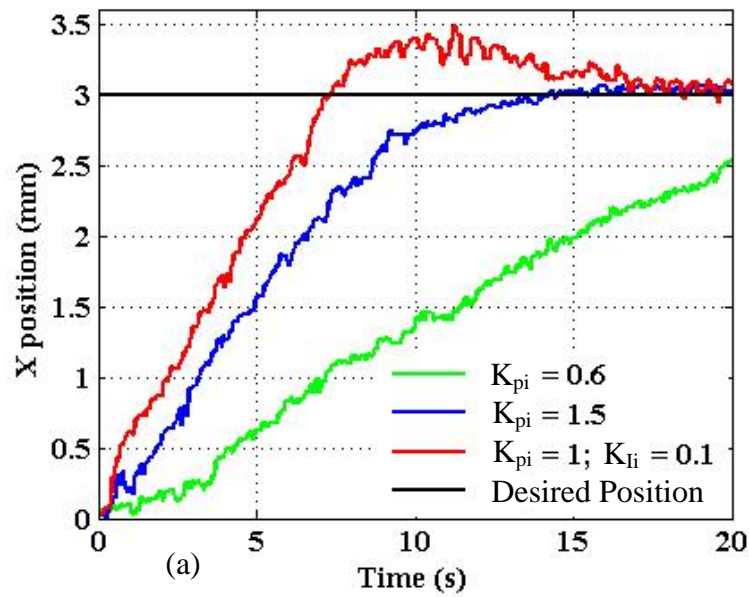
Fig. 4.2.2.1. Target position response for different gains (a) X displacement (b) Y displacement.

From Fig. 4.2.2.1, it can be observed that proportional controller (with K_{pi} = 1.5) gives the best response with minimum overshoot and settling time. The target reaches the desired position (with small steady state error) in approximately 15 seconds. For the following experiments, unless otherwise mentioned, proportional controller is used for the outer loop

with $K_{pi} = 1.5$. Note that the sampling rate (1 KHz) is substantially faster than the system dynamics. This satisfies requirement of the passivity control approach based on energy monitoring using discrete time force and velocity signals.

Experiment 2 (Effect of Phantom Properties)

This experiment demonstrates the effect of elastic properties of the phantom on target position response. Three different phantoms (phantoms 3, 4 and 5; see Appendix A for details) are used in this experiment. Phantoms 3 and 4 are homogeneous whereas phantom 5 is inhomogeneous. Fig. 4.2.2.2 shows X and Y coordinates of the target position for the three phantoms.
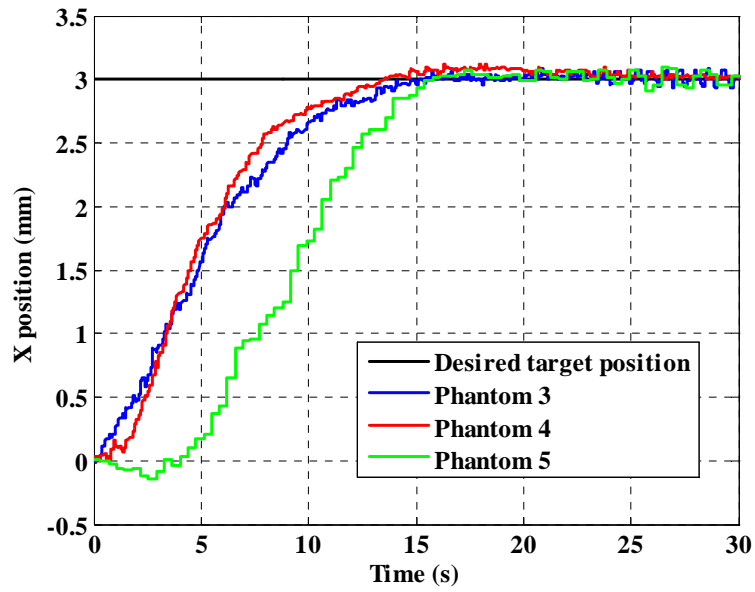
(a)
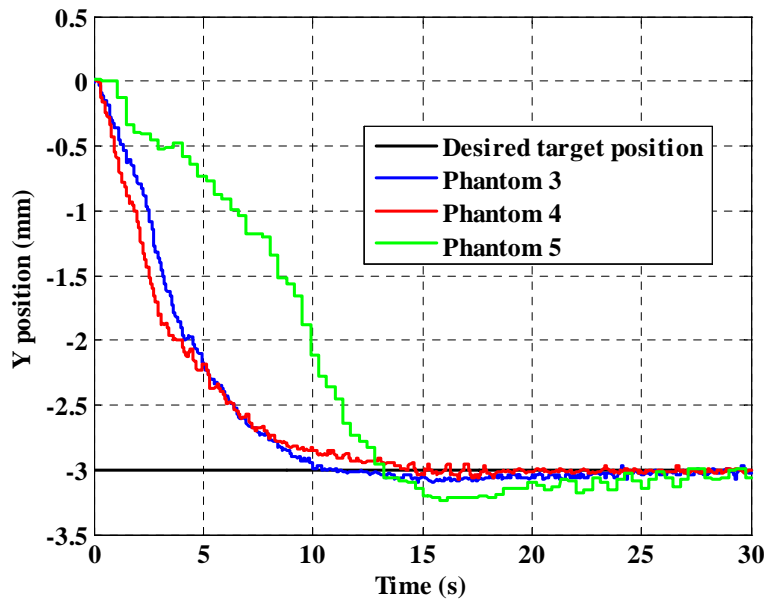
(b)

Fig. 4.2.2.2. Target position response for different phantoms (a) X displacement (b) Y displacement.

It can be observed from Fig. 4.2.2.2 that the target reaches the desired position in all cases. For phantom 5 (inhomogeneous), X coordinate reaches the desired position in 15 seconds

and Y coordinate reaches the desired position in 20 seconds. This demonstrates that the controller is effective in regulating the target position even when the composition of the phantom is inhomogeneous.

<u>Experiment 3 (Effect of Disturbance)</u>

This experiment demonstrates the effect of step disturbance on target position response. Phantom 3 (homogeneous) is used in this experiment. During target manipulation, an external step disturbance force (unknown magnitude) is applied to the phantom at point A (Fig. 4.2.2.3). This causes a change in path of the target. The controller corrects this deviation and guides the target to its desired position. The target reaches its desired position in about 25 seconds.

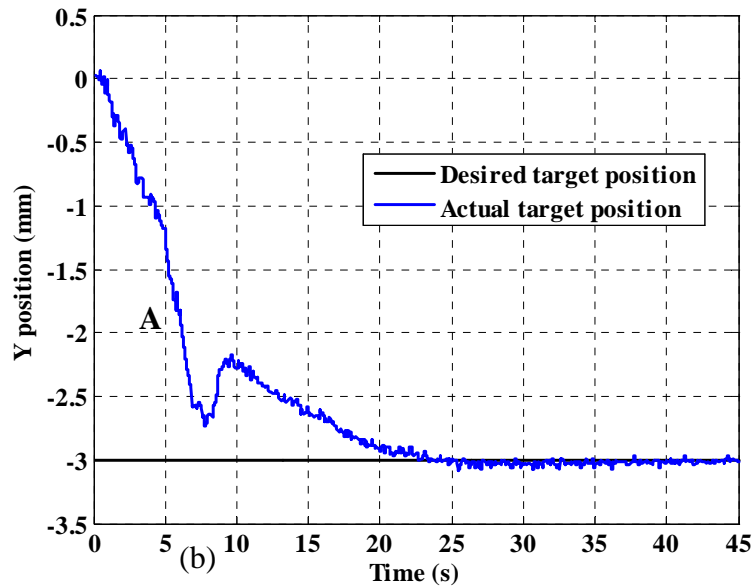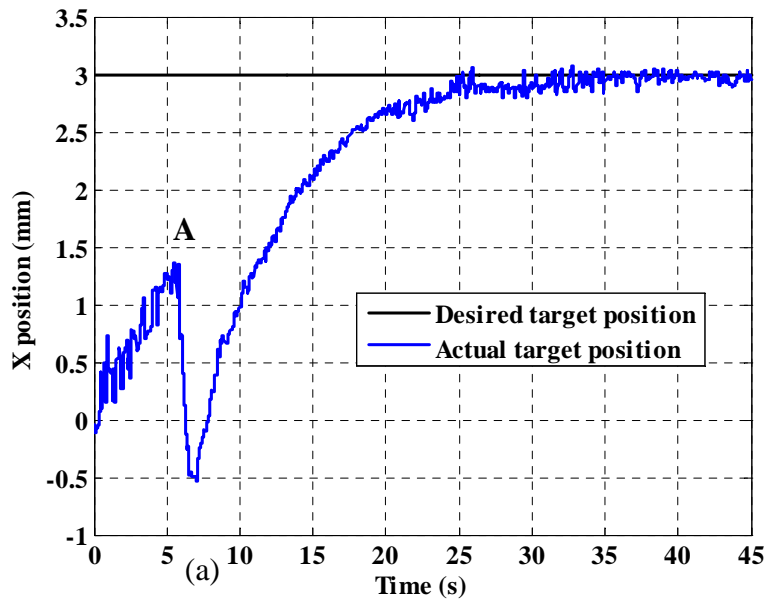Fig. 4.2.2.3. Target position response with step disturbance (a) X displacement (b) Y displacement.

Experiment 4 (Effect of PBC on Stability)

This experiment demonstrates performance of passivity based controller in stabilizing the target manipulation system under extreme operating conditions. It has been observed experimentally (Experiments 1, 2 and 3, for instance) that the system is stable under normal

operating conditions. Therefore, to demonstrate effectiveness of PBC, system parameters are modified as follows:

1) Choice of phantom: A very soft phantom, phantom 7 (with highest softener content, lowest volumetric ratio of plastic to plasticizer; Table A.1) is used. Estimated minimum stiffness ($\overline{K}$) of this phantom is 315 N/m. With an average compression of 18 mm at the contact points, value of E_0 computed using Eq. 2.4.33 is approximately 0.15.

2) Outer loop control gains: Outer loop control gains, K_{pi} and K_{Ii} and are chosen to be 0 and 5, respectively.

3) Feedback delay: Two second delay is introduced in the outer loop feedback path (x_t and y_t).

Without a passivity controller, low stiffness of the phantom in combination with high integral gain and feedback delay makes the system unsafe. To demonstrate this, in the first part of the experiment, PO/PC is not activated. Fig. 4.2.2.4 shows plots of the desired and actual velocities ($\dot{x}_{di}$ and $\dot{x}_i$, respectively) for the three robotic fingers. It can be observed from Fig. 4.2.2.4 (a) that the output of the outer loop controllers (desired actuator velocity, $\dot{x}_{di}$) increases to very high values. Fig. 4.2.2.4 (b) shows plots of the actual velocities of the robotic fingers. The robotic fingers do not track the desired actuator velocities due to saturation of the actuators. As mentioned in Chapter III, the actuators have a peak power point of 45 N at 2.5 mm/s. Unbounded increase in desired velocity is due to active behavior of the outer loop controllers. Fig 4.2.2.5 shows a plot of net energy output of the outer loop controllers. Inset in Fig. 4.2.2.5 shows a close up view of the energy plot from 0 - 4 seconds. It can be observed from Fig. 4.2.2.5 that the initial energy (E_0) of the outer loop controllers is

80

positive. As the fingers manipulate the phantom, net energy output reaches zero at point A (around 2.75 seconds) and continues to go negative (active behavior from point A to point B). Due to active behavior of the outer loop controllers, very high energy is transferred through the robotic fingers resulting in complete damage of the phantom.
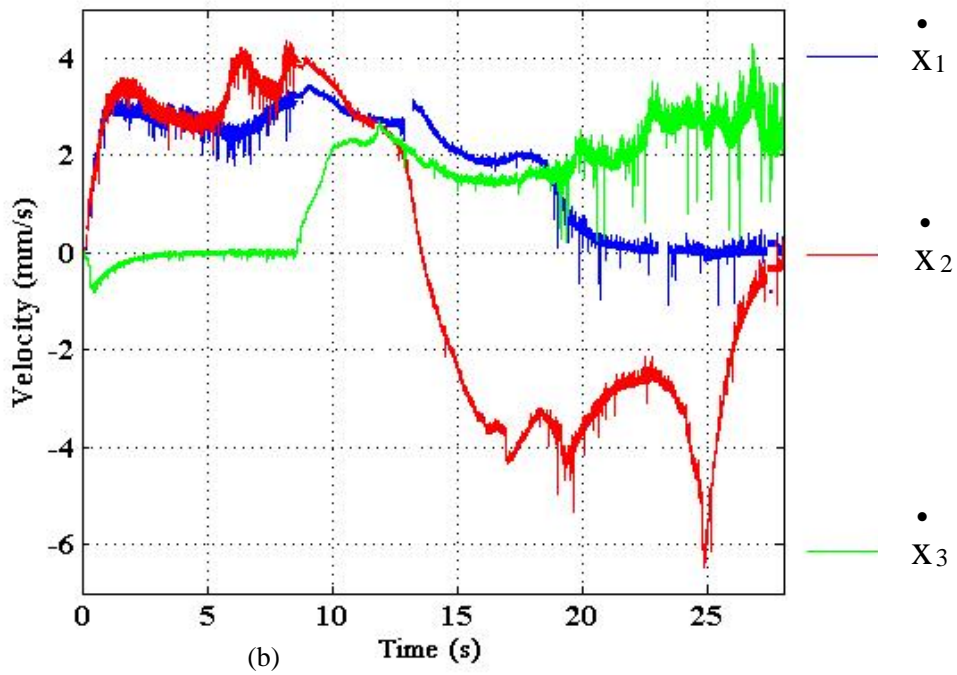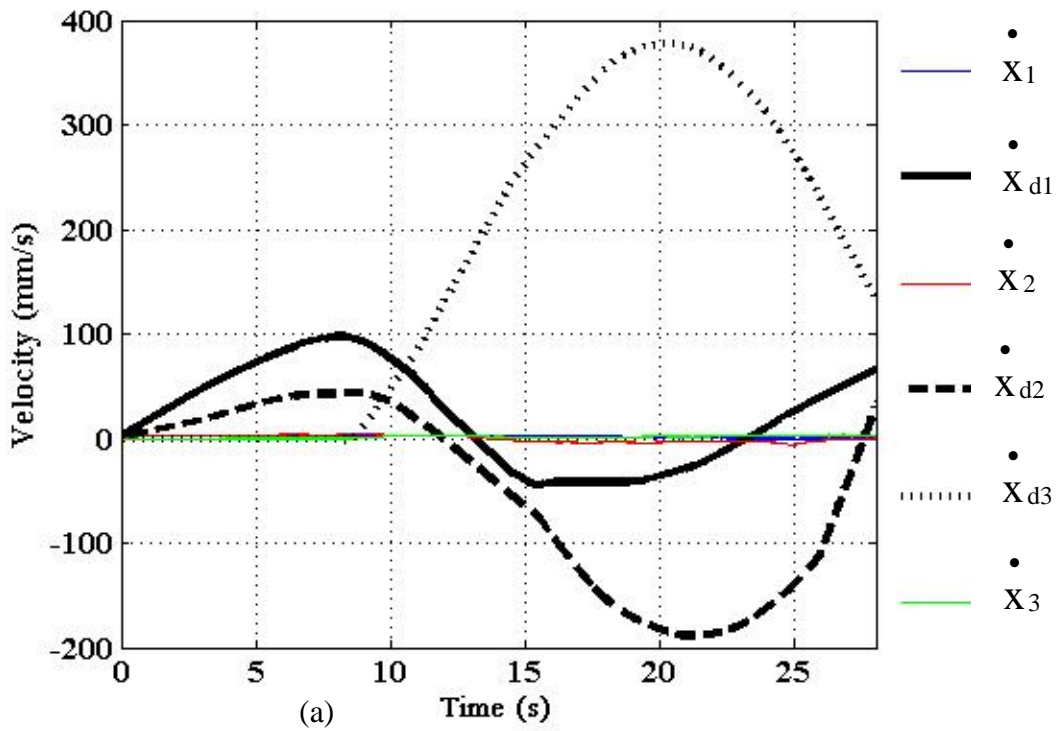
Fig. 4.2.2.4. Desired and actual velocities of robotic fingers without PO/PC (a) Desired and actual velocities (b) Actual velocities.

Fig. 4.2.2.5. Net energy output of outer loop controllers without PO/PC. Inset shows a close up view of the energy plot from 0 - 4 seconds.

Passivity based controller avoids this undesired behavior by modifying output of the outer loop controllers to ensure passivity of the entire system. To demonstrate this, the experiment in the first part is repeated with PO/PC enabled. Fig. 4.2.2.6 shows net energy output of the outer loop controllers. Inset in Fig. 4.2.2.6 shows a close up view of the energy plot from 0 – 4 seconds. It can be observed from Fig. 4.2.2.6 that the initial energy (E_0) is positive. As robotic fingers manipulate the phantom, net energy output reaches zero at point A (around 2.5 seconds). At this point the passivity controller is activated which constrains net energy output to be non negative using the constitutive relation of Eq. 2.4.14. This ensures passivity and consequently the stability of the entire system. Fig. 4.2.2.7 shows plots of the desired and actual velocities of the robotic fingers. The desired velocity increases from 0 – 2.5 seconds

(upto point A in Fig. 4.2.2.7 (a) and (b)). At point A, due to activation of PC, damping is introduced into the system which dissipates excess energy and reduces the desired velocity. Comparing Figs. 4.2.2.4 and 4.2.2.7, it can be observed that using the PC constrains output of the outer loop controllers ($\dot{x}_{di}$) to reasonable values within limits of saturation of the actuators. This passivity based control approach limits the amount of energy transferred to the deformable object ensuring safe target manipulation.

As mentioned earlier, during normal operation the system is passive and energy is not dissipated from the outer loop controllers with PO/PC. Extreme operating conditions (very high gains with significant feedback delay in target position) are specifically chosen for this experiment to demonstrate effectiveness of the passivity based controller in ensuring stability of the system. Even though the target does not converge to the desired position in such cases, the control law guarantees stability under all conditions.
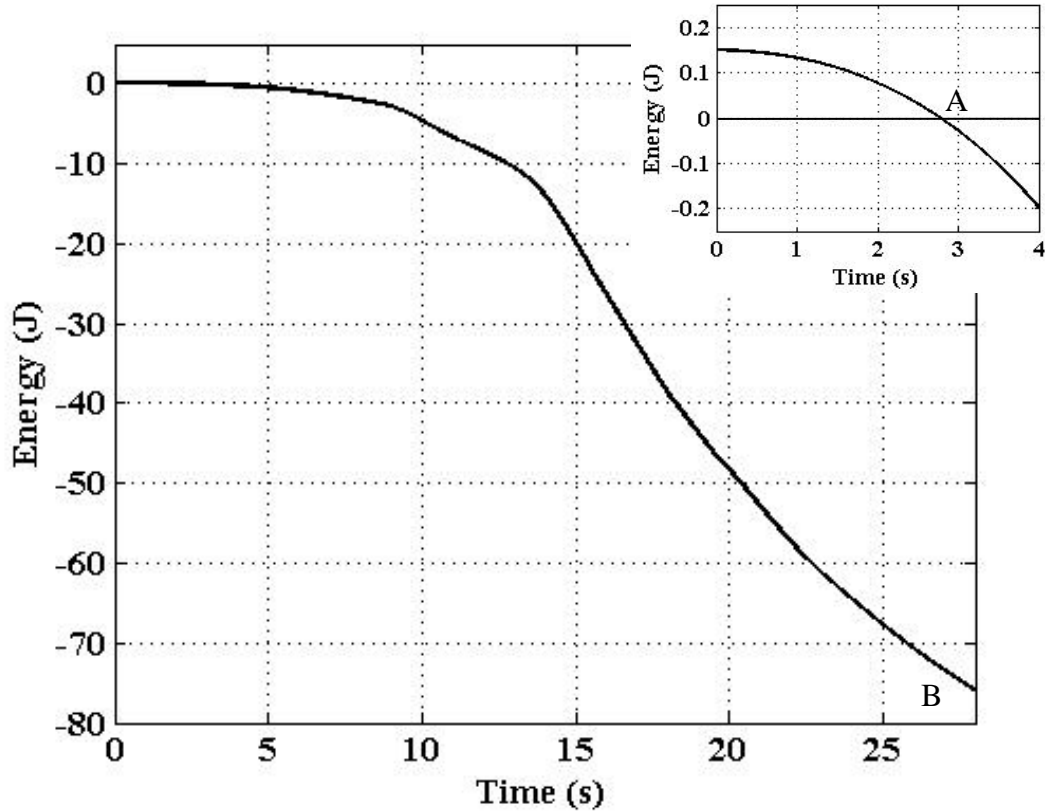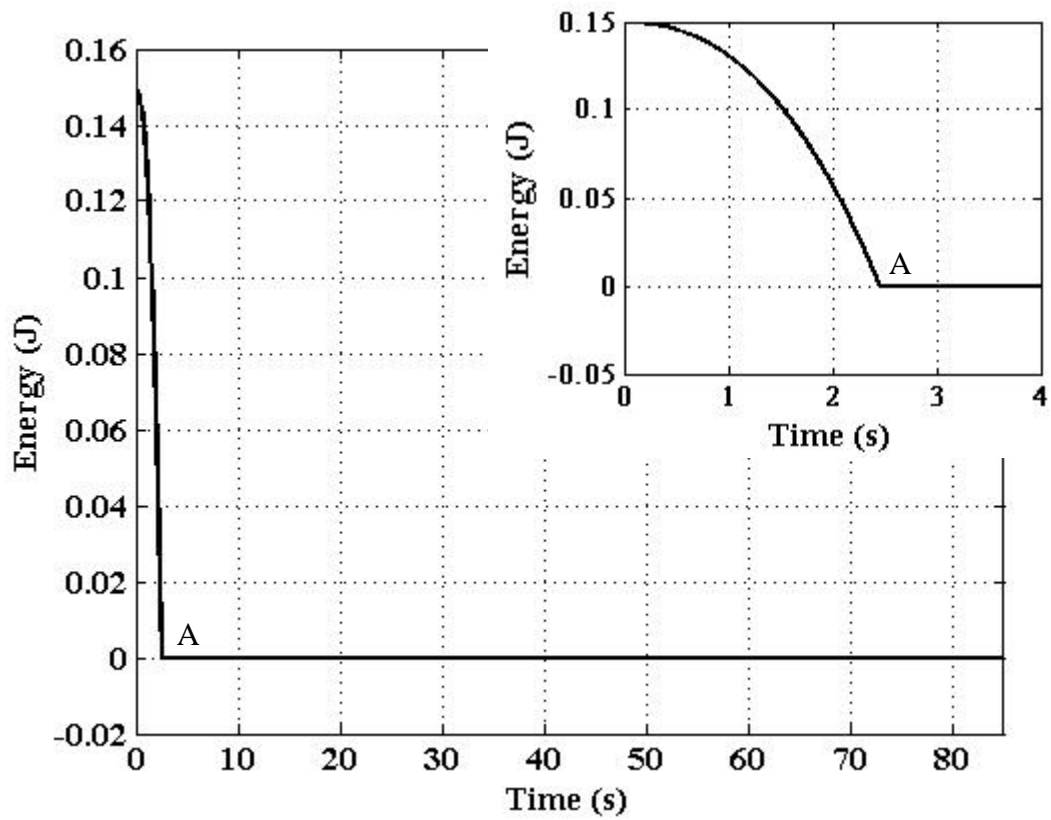
Fig. 4.2.2.6. Net energy output of outer loop controllers with PO/PC. Inset shows a close up view of the energy plot from 0 - 4 seconds.
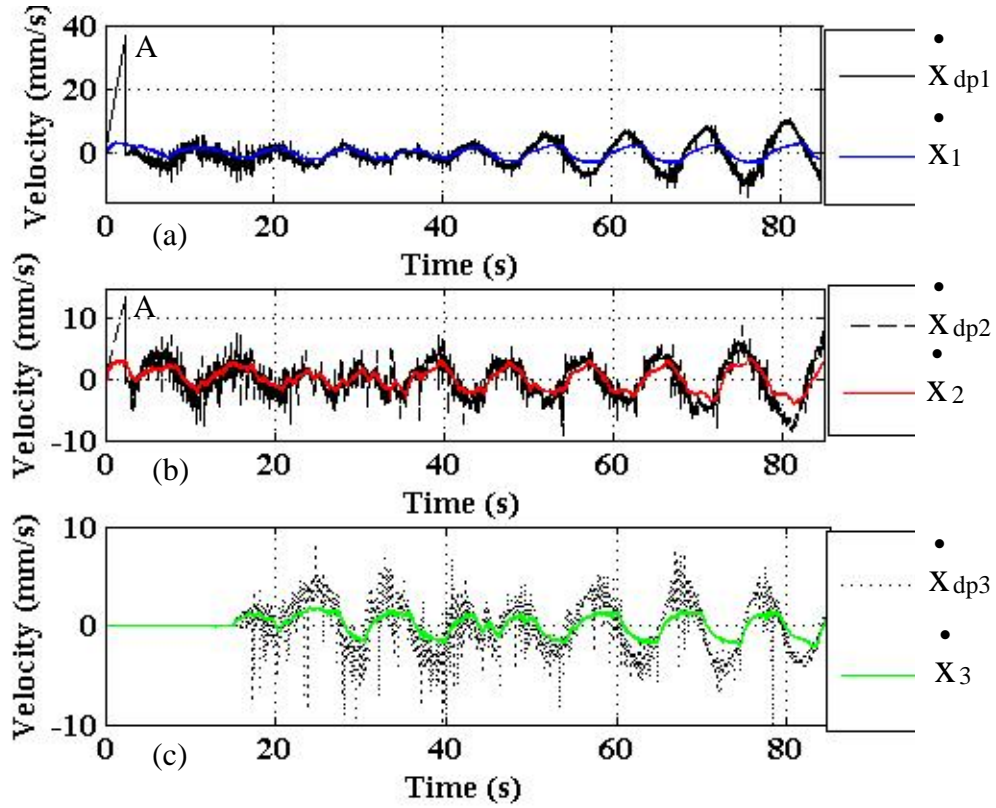
Fig. 4.2.2.7. Desired and actual velocities of three robotic fingers with PO/PC.

Tracking

Even though the primary application of this controller is for regulation tasks (for instance, breast CNB), tracking results are presented briefly to ensure continuity of the discussion and to demonstrate the capabilities (and limitations) of this system. For tracking, it is desired to move the target along a desired trajectory, denoted as $\mathbf{P_d}$ (in this case, $\mathbf{P_d}$ is a function of time). In the following experiments, the desired trajectory (in mm) is given by

$$\mathbf{P_d} = \begin{bmatrix} x_0 + 3\sin(2\pi f t) \\ y_0 - 3\sin(2\pi f t) \end{bmatrix}. \tag{4.2.3.1}$$

$$\dot{\mathbf{P}}_\mathbf{d} = \begin{bmatrix} 6\pi f \cos(2\pi f t) \\ -6\pi f \cos(2\pi f t) \end{bmatrix}. \tag{4.2.3.2}$$

$\mathbf{P_0}(x_0, y_0)$ represents the initial target position and f is the frequency of the desired trajectory.

To aid understanding and comparison, all the graphs in this section are plotted by zeroing the initial target coordinates.

For tracking tasks, desired velocity of the target is non zero, $\dot{x}_{tdi} \neq 0$. Therefore the trajectory generates energy and is not passive. However, from Eq. 4.2.3.2 it can be observed that the desired target velocity is not dependent on system states. Therefore, passivity of the plant and controllers is sufficient to ensure system stability.

Experiment 5 (Effect of Frequency of Desired Target Trajectory)

The passivity based controller is used to track the desired target trajectory. Phantom 5 (inhomogeneous) is used in this experiment. Fig. 4.2.3.1 shows X and Y coordinates of the target position for five sets of trajectory frequencies. In all cases, tracking is not good during the initial period (0 – 10 seconds) since only two fingers are active. Once the phantom is compressed, radially outward motion of the fingers also contributes toward target movement. Since all three fingers are active, tracking is improved. However tracking is fairly good up to a frequency of 1/20 Hz. Target does not follow the trajectory well at higher frequencies.
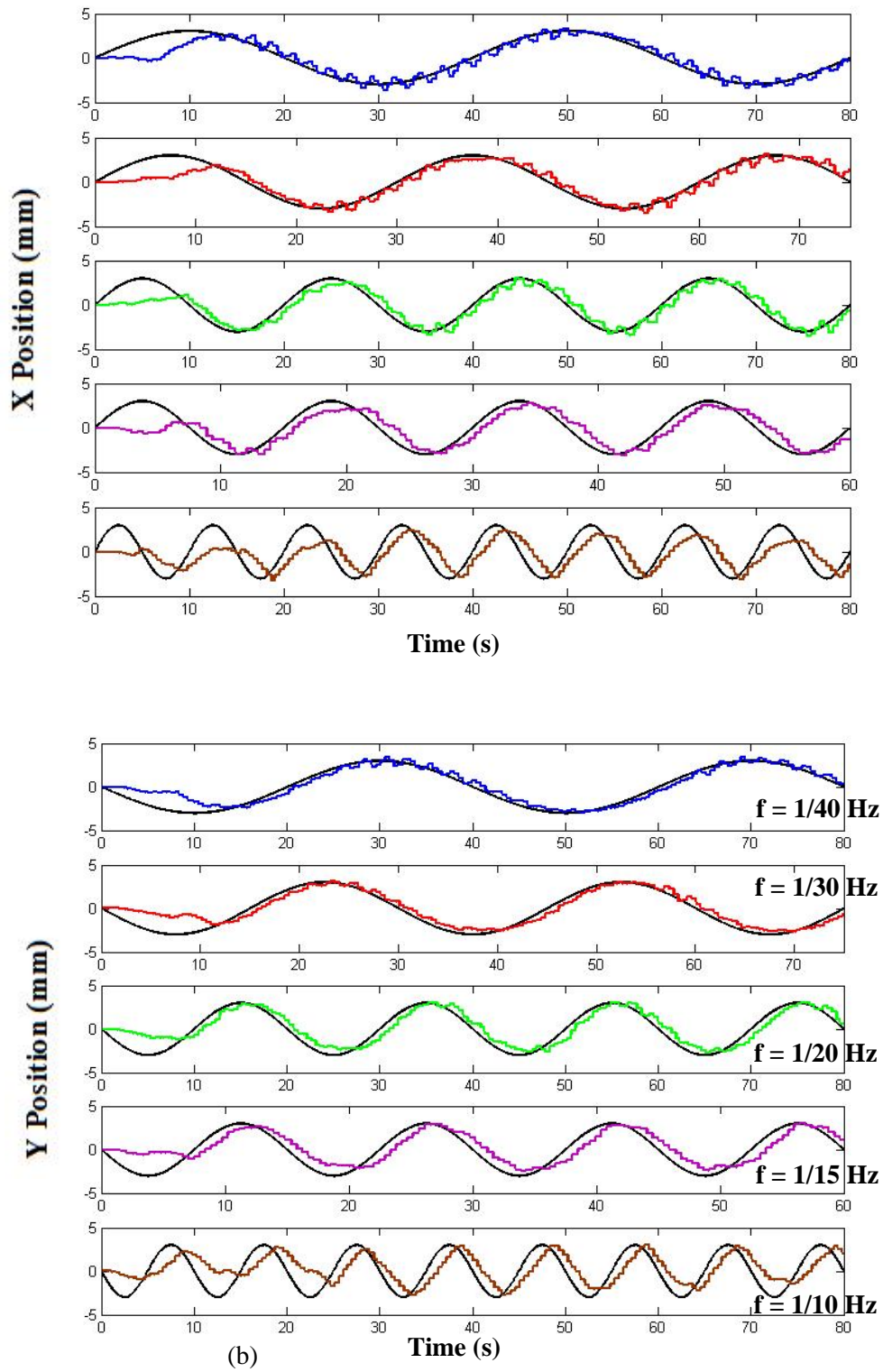
Fig. 4.2.3.1. Trajectory tracking with passivity based controller (a) X displacement (b) Y displacement.

88

Error Analysis of Target Positioning During Planar Manipulation

Root mean square error (RMSE) is used to quantify the target positioning accuracy using passivity based control. RMSE is defined as

$$\text{RMSE} = \sqrt{\dfrac{\sum_{t=t_i}^{t_f}(\mathbf{P_d} - \mathbf{P_t})^2}{n}} \, , \tag{4.2.4.1}$$

where t_i and t_f represent the limits of the time interval over which RMSE is computed. $\mathbf{P_d}$ is the desired target position and $\mathbf{P_t}$ is the actual target position at time t. n is the number of data points in the chosen time interval. Table 4.2.4.1 shows the RMSE values for the five trials. Targeting accuracy is evaluated at steady state. Therefore, in all cases, t_i and t_f are chosen such that the time interval spans the last five seconds of the experiment. Sampling time for the controller is 0.001 s, hence n equals 5001. It can be observed from Table 4.2.4.1 that the error in target position is less than 0.09 mm (3%) in all trials. Therefore this technique can be used to successfully manipulate position of a target embedded in a deformable object.

Table 4.2.4.1. Error in target positioning using PBC.

Trial	RMSE (mm)
Experiment 1; $K_{pi} = 1.5$	0.042
Experiment 2; Phantom 3	0.056
Experiment 2; Phantom 4	0.022
Experiment 2; Phantom 5	0.087
Experiment 3	0.074

<u>Needle – Target Alignment During Breast CNB</u>

In this section, experimental results are presented to demonstrate the efficacy of the passivity based control technique developed in Chapter II for target manipulation during breast CNB. Experiments are performed on phantoms which mimic breast tissue. A target embedded in the phantom simulates a tumor or a lesion in the breast. As discussed in Chapter I, the basic idea is to manipulate the breast tissue by applying external force using robotic fingers to control the position of an internal target. The goal is to position the target on the needle insertion line so as to minimize needle – target misalignment. Experimental results are also presented to demonstrate the application of a hybrid supervisory controller for autonomous coordination of target manipulation, US image acquisition and needle insertion.

Needle Orientation in Global Reference Frame

Needle orientation is required to accurately position the target along the needle path (Eq. 3.5.1). Needle segmentation in US images is a challenging task. Therefore, forward kinematics of the needle device (Chapter III) is used to determine orientation of the needle and position of the needle tip. Target coordinates are measured with respect to the global reference frame (Fig. 3.3.3.1). Hence, needle orientation is also expressed in the global reference frame. Since the target coordinates are measured using the forward kinematics of the US device (Chapter III) and the needle orientation is measured using the forward kinematics of the needle device, there exists relative measurement error between the two devices. The following experiment is conducted to quantify the measurement error.

<u>Experiment 6 (Relative Measurement Error Between the US and the Needle Devices)</u>

A phantom (without any embedded target) is suspended vertically as shown in Fig. 4.3.1.1.
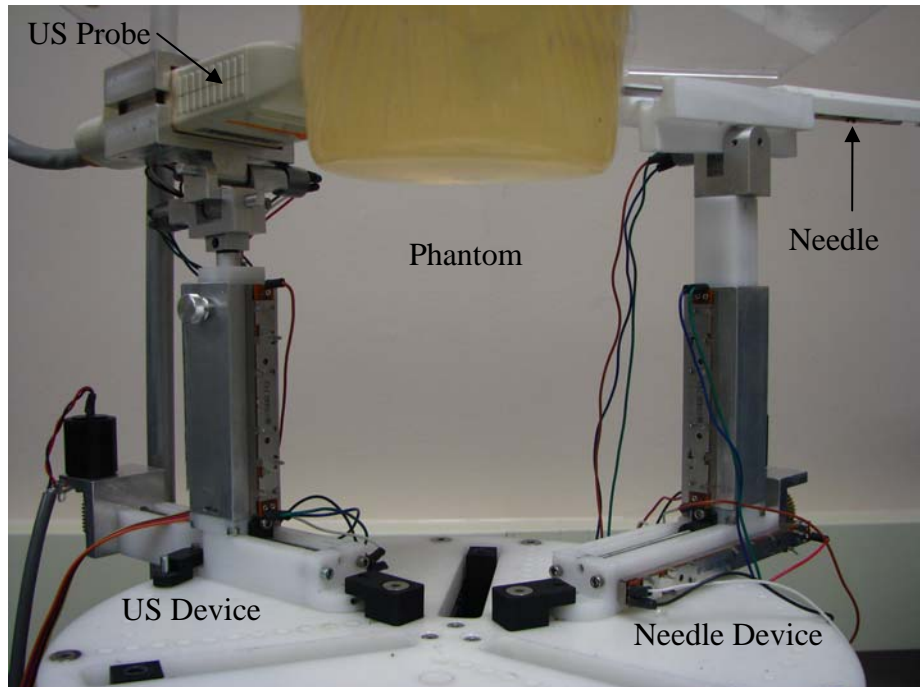
Fig. 4.3.1.1. Experimental setup for determining measurement error.

The needle device is used to position the biopsy needle at an arbitrary location. Using the needle guide, the biopsy needle is inserted into the phantom. The US device is positioned such that needle is visible in the US image. Care is taken to ensure that the image plane of the US probe is parallel to the needle to eliminate error in identifying the needle tip. Needle tip position is then measured using two techniques: (1) Needle insertion depth and the joint coordinates of the needle device are measured. Position of the needle tip (with respect to global reference frame, Fig. 3.3.3.1) is determined using the forward kinematics of the needle device. (2) Needle tip is identified in the US image using semi-automatic segmentation. Position of the needle tip (with respect to global reference frame) is determined using the forward kinematics of the US device. This process is performed for four different poses of the needle. Table 4.3.1.1 shows the position coordinates of the needle tip measured using the two techniques.

It can be observed from Table 4.2.4.1 that the maximum error in determining the needle tip position with the two devices is 7.9 mm. Volumetric workspace of the needle device is 90100 mm^3 and maximum distance moved by the needle device in the horizontal plane is 106 mm (joint 2 in Fig. 3.3.2.1) from the global origin. Maximum distance moved by the needle device in the vertical plane is 184 mm (joint 3 in Fig. 3.3.2.1) from the global origin. Needle device uses five potentiometers and the US device uses six potentiometers to determine position of the needle tip. Considering these facts, error (less than 7.9 mm in determining needle tip position) between the two devices is within reasonable limits.

Table 4.3.1.1. Relative measurement error of needle tip.

Pose	Needle Tip Coordinate	Position Measurement		Absolute Error (mm)
		US Device (mm)	Needle Device (mm)	
1	X	15.5	23.4	7.9
	Y	22.7	25.2	2.5
	Z	191.2	196.4	5.2
2	X	21.9	26.6	4.7
	Y	58.8	55.0	3.8
	Z	191.2	197.1	5.9
3	X	24.2	27.7	3.5
	Y	49.3	48.6	0.7
	Z	155.3	150.3	5.0
4	X	17.7	21.9	4.2
	Y	25.9	18.7	7.2
	Z	134.7	141.5	6.8

Experimental Setup for Needle Insertion

As discussed in the previous section, there is an error in determining the needle tip position between the US device and the needle device. In experiment 6, needle tip is a convenient choice to quantify the error between the two devices. In fact, this error exists in determining the relative position of the needle and the target (with respect to global reference frame) using the forward kinematics of the devices. Even though the error is within reasonable limits

for the system, this (an absolute error of about 8 mm) could potentially undermine the accuracy achieved using target manipulation. The primary objective of this work is to demonstrate the effectiveness of target manipulation in minimizing needle – target misalignment during needle insertion tasks. Therefore, assuming that the needle orientation is known (which can be accomplished by using a six degree-of-freedom EM sensor; for instance miniBIRD® from Ascension Tech has translational and angular accuracy of 1.8 mm and 0.5^0 respectively), target manipulation technique can be used to position the target accurately on the needle path.

The experimental setup is shown in Fig. 3.3.3.1. A top view of the experimental setup is shown in Fig. 4.3.2.1. Since the needle path cannot be determined very accurately, a nominal needle path is defined with respect to the orientation of the US image frame. The needle device is positioned such that needle insertion is as close as possible to the nominal path. Due to inherent limitation of accurately determining the needle path, the actual needle path will vary slightly from the nominally defined path. The goal of the controller is to position the target on the nominal path. Since the actual needle path is fairly close to the nominal path, disturbance force exerted due to needle insertion will sufficiently mimic an actual biopsy procedure. This facilitates objectively determining the accuracy of target manipulation independent of the accuracy of measuring needle orientation.

Typically during breast biopsy procedures, needle is inserted parallel to the image plane of the US probe. This minimizes error in visually identifying the needle tip in the US image. In this experimental setup, the US probe is coplanar (horizontal plane) with the robotic fingers. As discussed in Chapter III, needle is inserted at an angle (altitude, θ) to the horizontal plane. Therefore, needle insertion is not parallel to the image plane of the US probe. The US

probe is placed coplanar with the robotic fingers because the thickness of the image slice obtained with the US probe is about 5 mm. Therefore maximum resolution (in controlled coordinates, X and Y) of target position is obtained when the image plane is coplanar with the target manipulation plane (horizontal plane).
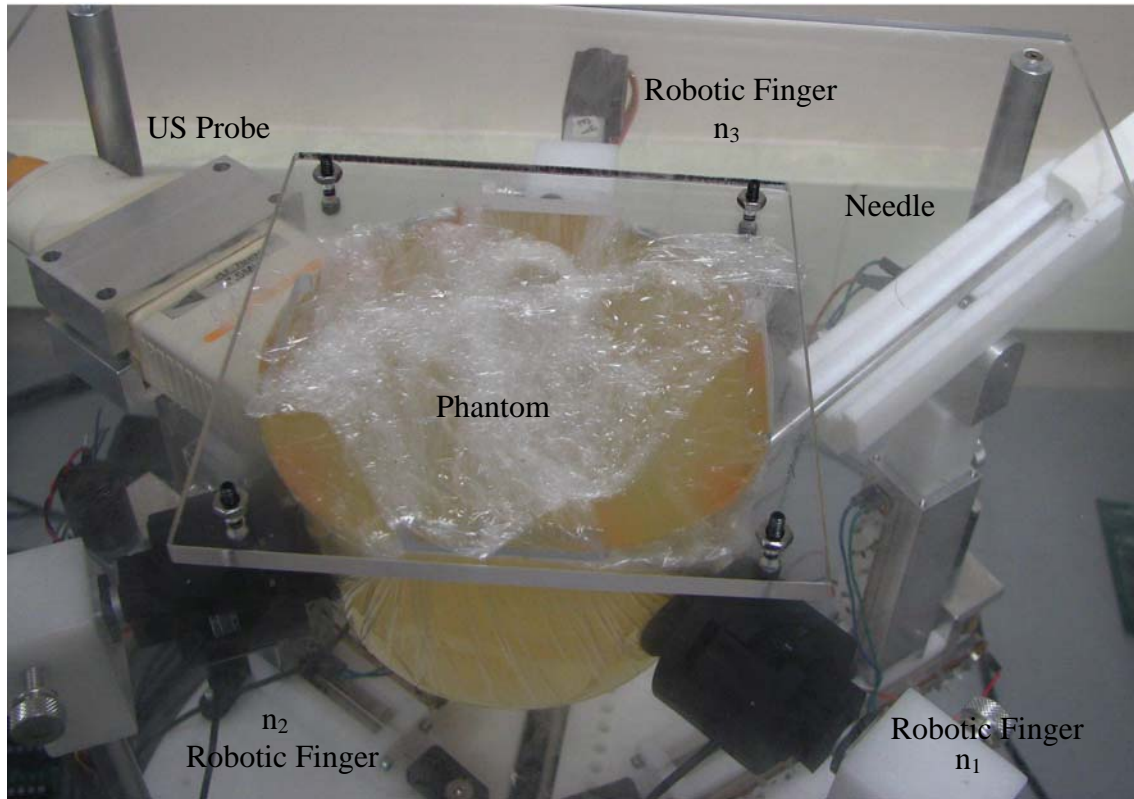

Fig. 4.3.2.1. Experimental setup for target manipulation during needle insertion.

Unit vectors defining the direction of force application by the robotic fingers are n_1, n_2 and n_3. In this setup,

$$n_1 = [0.5\ 0.866], \tag{4.3.2.1}$$

$$n_2 = [0.5\ \text{-}0.866], \tag{4.3.2.2}$$

$$n_3 = [\text{-}1\ 0]. \tag{4.3.2.3}$$

To minimize needle – target misalignment, the desired target position is along the nominal needle path. The desired target position is determined using the planner (discussed in Chapter III). Since the target is positioned at a specific location, this is a regulation task.

Target Manipulation During Needle Insertion

Several experimental results are presented to demonstrate the (1) accuracy of target positioning during needle insertion and (2) efficacy of supervisory controller in coordinating image acquisition, manipulation and needle insertion. Force threshold (Eq. 3.4.3.4) for the robotic fingers is chosen as 25 N.

Experiment 7 (Minimizing Needle – Target Misalignment During Needle Insertion)

This experiment demonstrates the efficacy of target manipulation in minimizing needle – target misalignment during needle insertion. Phantom 5 (inhomogeneous, see Appendix A for details) with an embedded target is used in this experiment. Fig. 4.3.3.1 shows the target and nominal needle paths. In Fig. 4.3.3.1, point A is the initial location of the target and point B is the final location of the target. It can be observed from Fig. 4.3.3.1 that the target is not located on the needle path initially (point A). Robotic fingers apply external force to minimize the initial misalignment. As the needle is inserted, due to disturbance force exerted by the needle (first puncture occurs at point A^*), target moves out of the needle path. The robotic fingers compensate for the random target movement and steer the target onto the needle path (point B). Fig. 4.3.3.2 shows a plot of the X and Y coordinates of the target position. It can be observed from Fig. 4.3.3.2 that needle insertion and target manipulation takes about 30 seconds. At the end of needle insertion, the target is positioned at the needle tip accurately. In this experiment, the US probe is continuously in contact with the phantom

and the target is in the image plane of the probe. Therefore, the supervisory controller is in the manipulation state (see Chapter III) throughout the experiment.
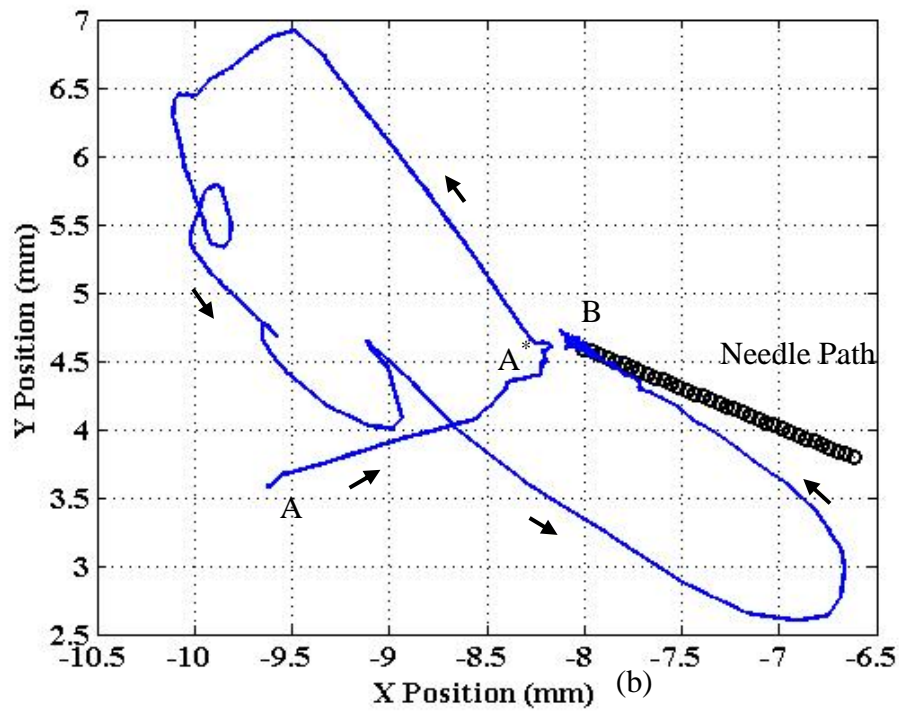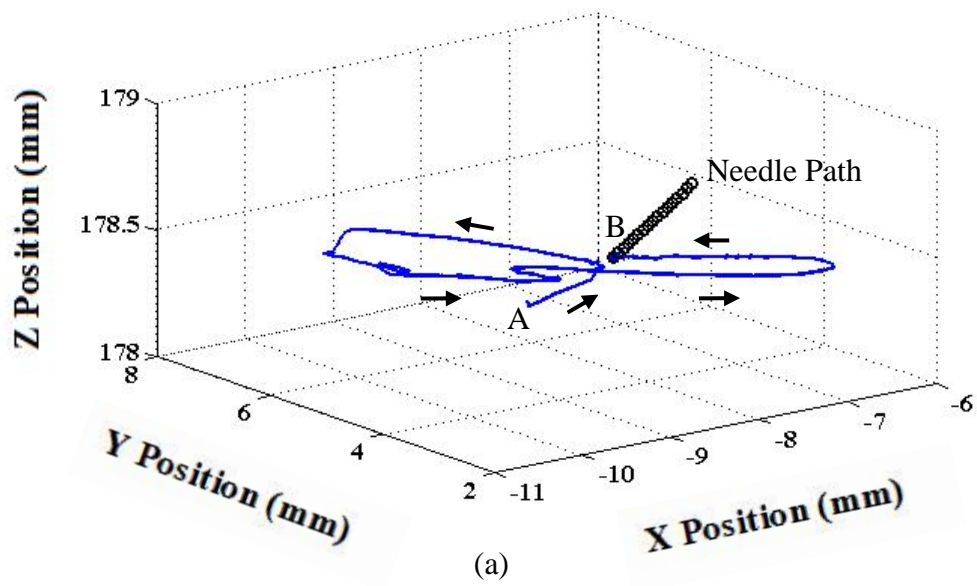
Fig. 4.3.3.1. Target and nominal needle paths during needle insertion (a) 3D (b) projection onto the XY

(horizontal) plane.
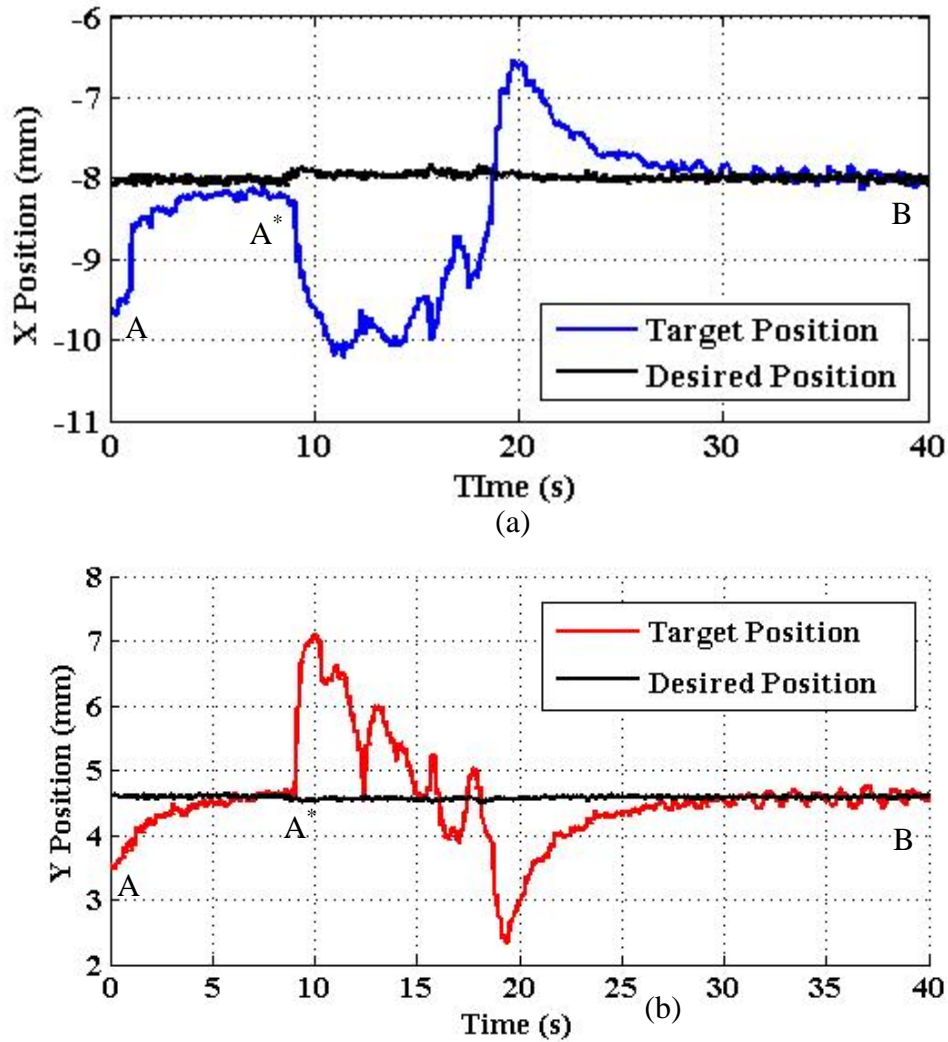
Fig. 4.3.3.2. Target position response during needle insertion (a) X displacement (b) Y displacement.

Experiment 8 (Supervisory Control During Needle Insertion)

This experiment demonstrates the efficacy of the supervisory controller in coordinating target manipulation, US probe movement and needle insertion. Phantom 1 (homogeneous, see Appendix A for details) with an embedded target is used in this experiment. Fig. 4.3.3.3 shows the target and nominal needle paths during 3D needle insertion. In Fig. 4.3.3.3, point A is the initial location of the target. It can be observed from Fig. 4.3.3.3 that the target is not located on the needle path initially (point A). Robotic fingers apply external force to

99

minimize the initial misalignment. An external disturbance (simulating lateral patient movement) is applied at point B which results in the US probe losing contact with the phantom. Fig. 4.3.3.4 shows the control signals for the four states (see Chapter III) of the supervisory controller. A rising edge enables the state and a falling edge disables the state. At any time only one state of the supervisory controller is active. At point B, loss of contact is detected (using the algorithm described in Chapter III) and the manipulation state is disabled. Fig. 4.3.3.5 shows the target position response along X and Y coordinates. From point B, target position data is not available due to loss of contact. At point B, contact initiation state is enabled and the US probe is moved to reestablish contact with the phantom. Fig. 4.3.3.6 shows movement of the US probe along prismatic joints (d_2 and d_4) of the US device. At point B, the US probe is moved along prismatic joint (d_2) until contact is detected (at point B^*). At point B^*, contact is established but the target is not detected in the US image plane. Hence, the supervisory controller shifts to the target tracking state at point B^*. In the target tracking state, the US probe is moved along prismatic joint (d_4) using the algorithm described in Chapter III. Once the target is detected at point C, the control shifts back to the manipulation state. Target position data is not available from point B to C and the state indicator LED turns on to indicate that needle insertion should be stopped during this time. From point C, needle insertion resumes and the robotic fingers steer the target towards the needle path. At the end of needle insertion, the target is positioned at the needle tip accurately (point D). It can be observed from Fig. 4.3.3.5 that needle insertion and coordinated probe movement with target manipulation takes about 40 seconds.

Fig. 4.3.3.3. Target and nominal needle paths during 3D needle insertion.

Fig. 4.3.3.4. Signals for enabling/disabling supervisory controller states.
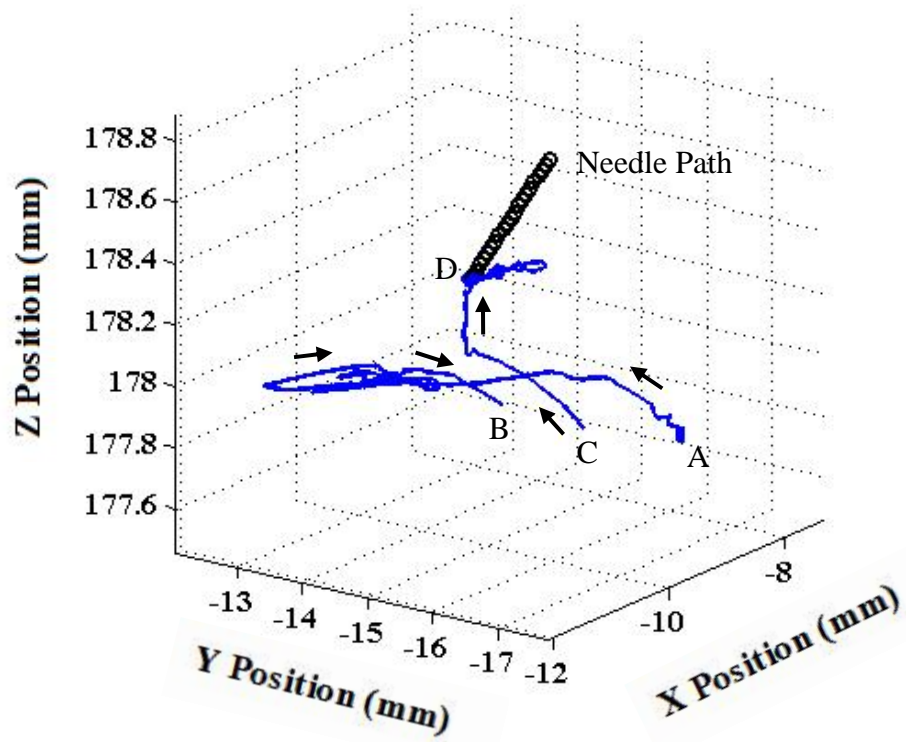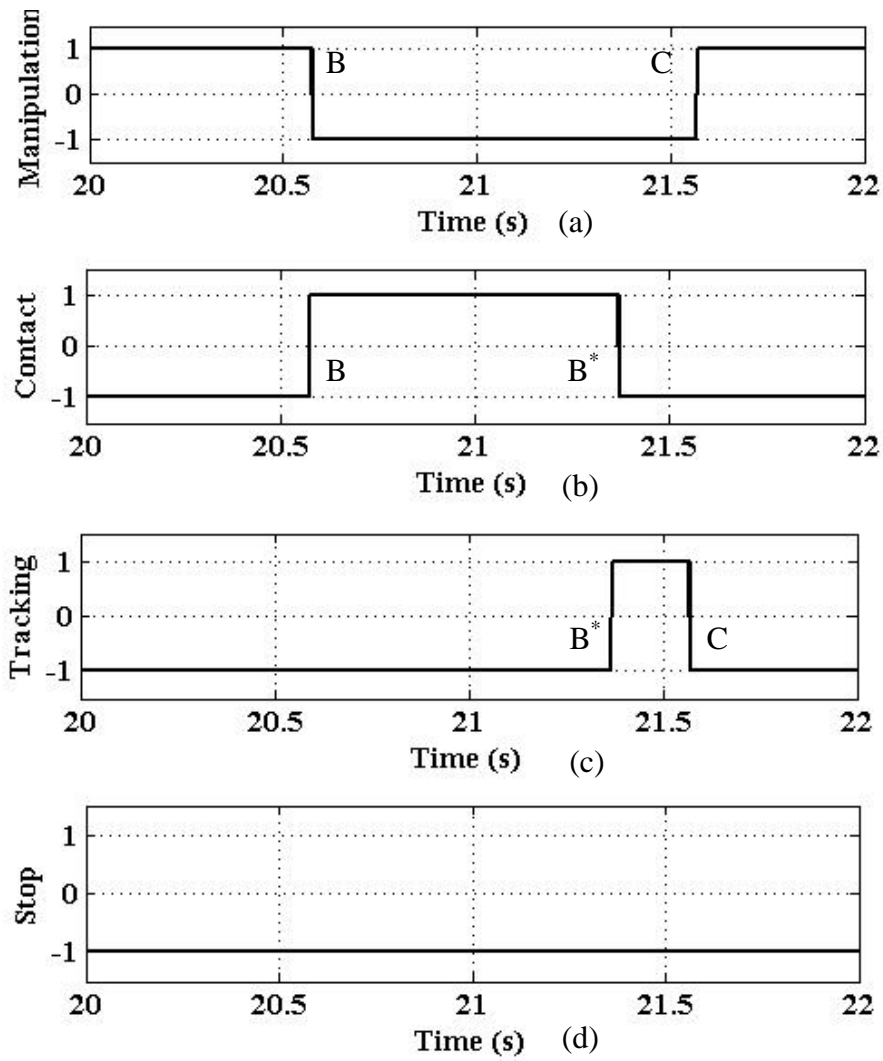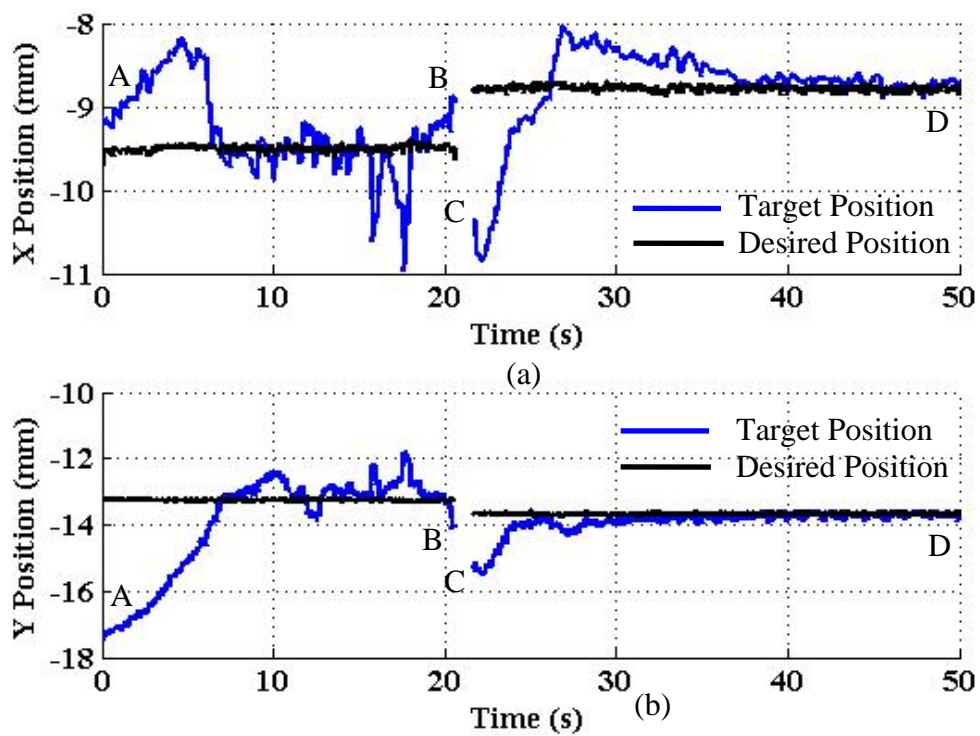
Fig. 4.3.3.5. Target position response during needle insertion (a) X displacement (b) Y displacement.

Fig. 4.3.3.6. Joint coordinates of US image acquisition device.

<u>Experiment 9 (Supervisory Control During Needle Insertion – Target Tracking)</u>

This experiment demonstrates the efficacy of the supervisory controller in coordinating target manipulation, tracking out-of-plane target movement and needle insertion. Phantom 2 (homogeneous, see Appendix A for details) with an embedded target is used in this experiment. Fig. 4.3.3.7 shows the target and nominal needle paths during 3D needle insertion. In Fig. 4.3.3.7, point A is the initial location of the target. It can be observed from Fig. 4.3.3.7 that the target is not located on the needle path initially (point A). Robotic fingers apply external force to minimize the initial misalignment. An external disturbance (simulating vertical patient movement) is applied at point B which results in the target moving out of image plane of the US probe. Fig. 4.3.3.8 shows the control signals for the four states of the supervisory controller. A rising edge enables the state and a falling edge

disables the state. At any time only one state of the supervisory controller is active. At point B, out-of-plane target movement is detected (through segmentation of the US image) and the manipulation state is disabled. Fig. 4.3.3.9 shows the target position response along X and Y coordinates. From point B, target position data is not available since the target is not identified in the US image. At point B, target tracking state is enabled and the US probe is moved to search and recover the target. Fig. 4.3.3.10 shows movement of the US probe along prismatic joint (d_4) of the US device. At point B, the US probe is moved along prismatic joint (d_4) using the algorithm described in Chapter III. At point C, target is detected and the supervisory controller shifts back to the manipulation state. Target position data is not available from point B to C and the state indicator LED turns on to indicate that needle insertion should be stopped during this time. From point C, needle insertion resumes and the robotic fingers steer the target towards the needle path. At the end of needle insertion, the target is positioned at the needle tip accurately (point D). It can be observed from Fig. 4.3.3.9 that needle insertion and coordinated probe movement with target manipulation takes about 60 seconds.

Fig. 4.3.3.7. Target and nominal needle paths during 3D needle insertion.

Fig. 4.3.3.8. Signals for enabling/disabling supervisory controller states.
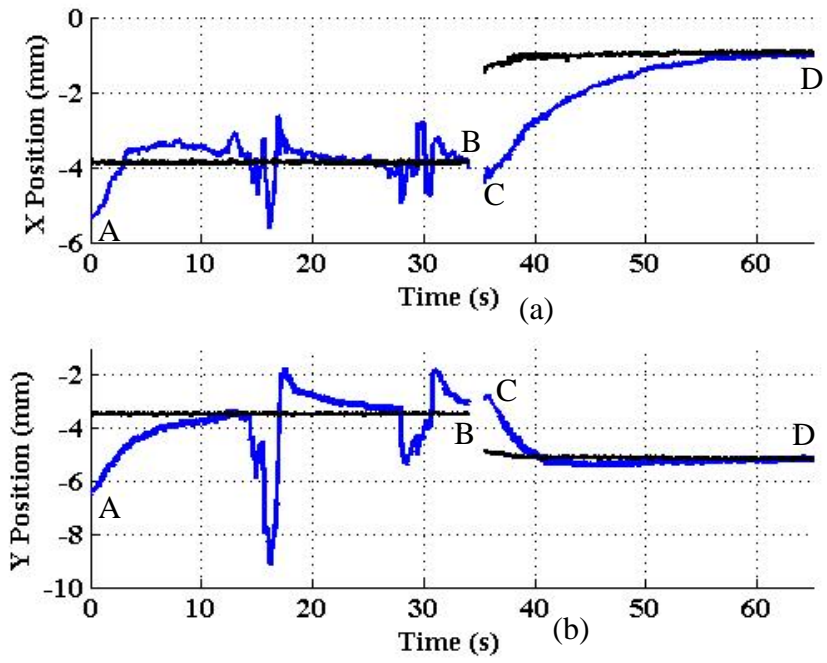
Fig. 4.3.3.9. Target position response during needle insertion (a) X displacement (b) Y displacement.
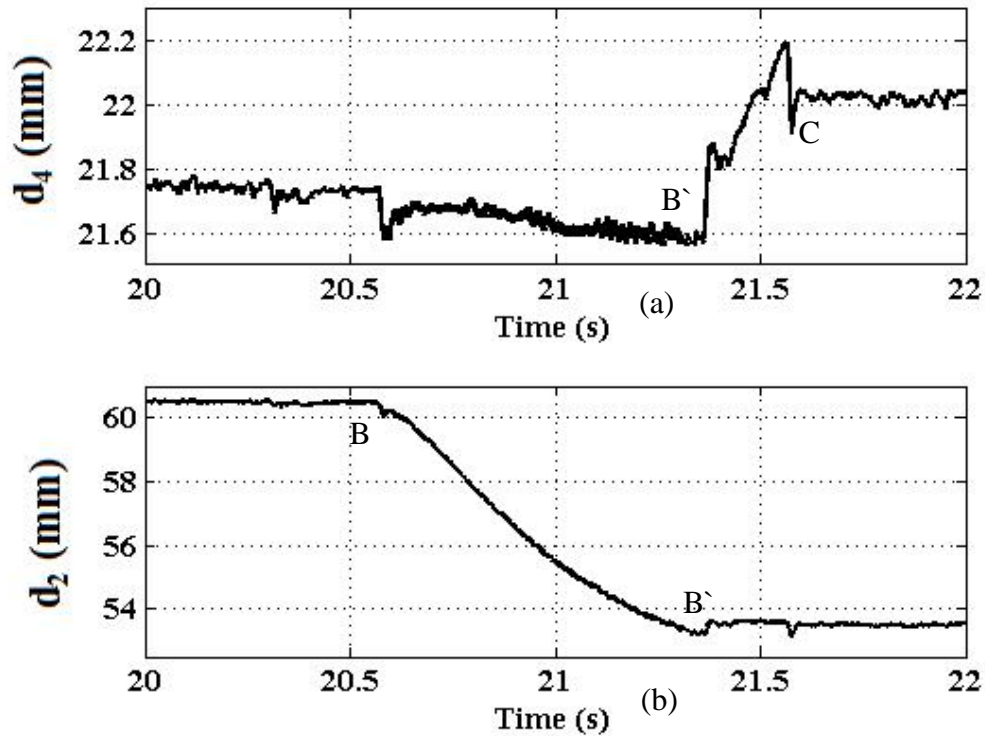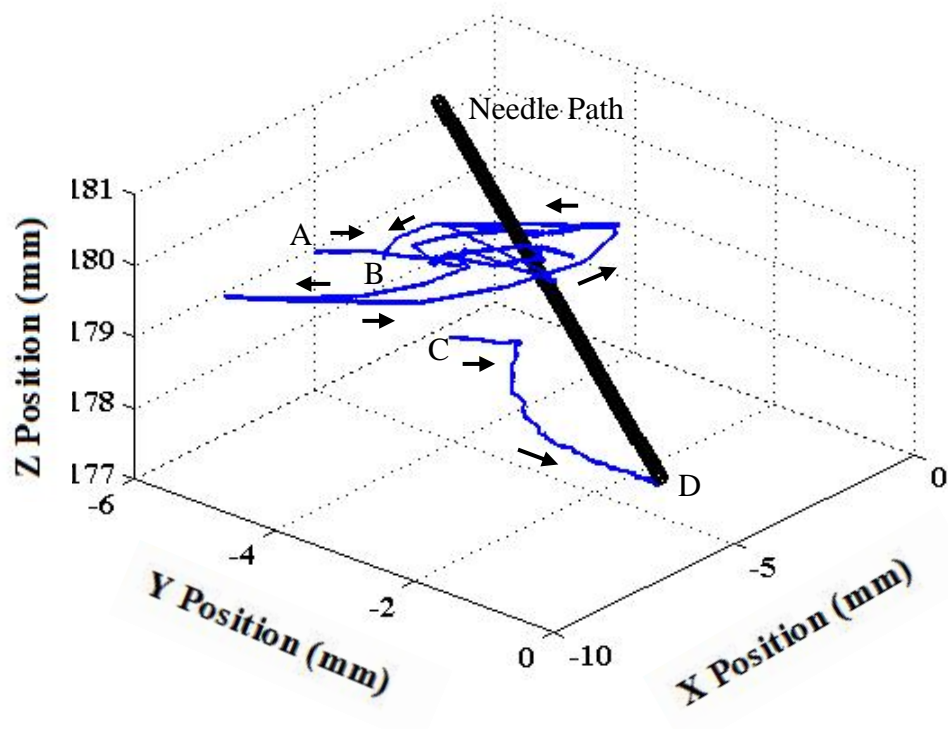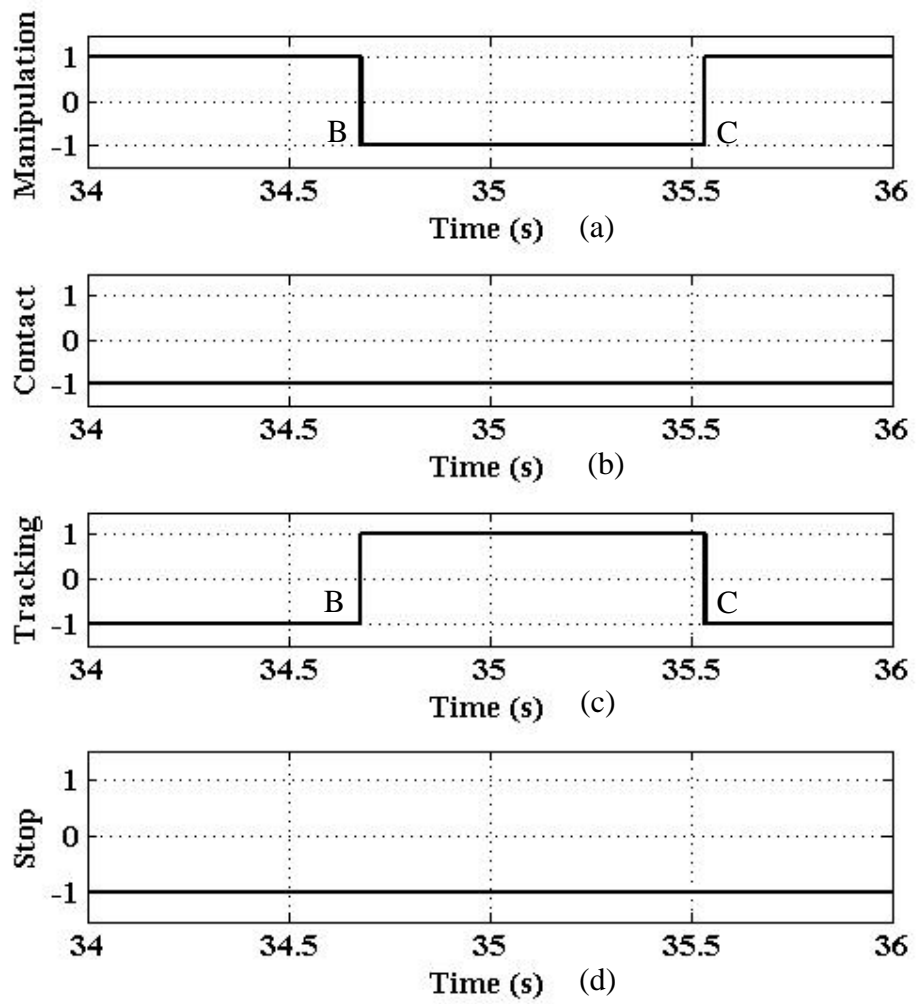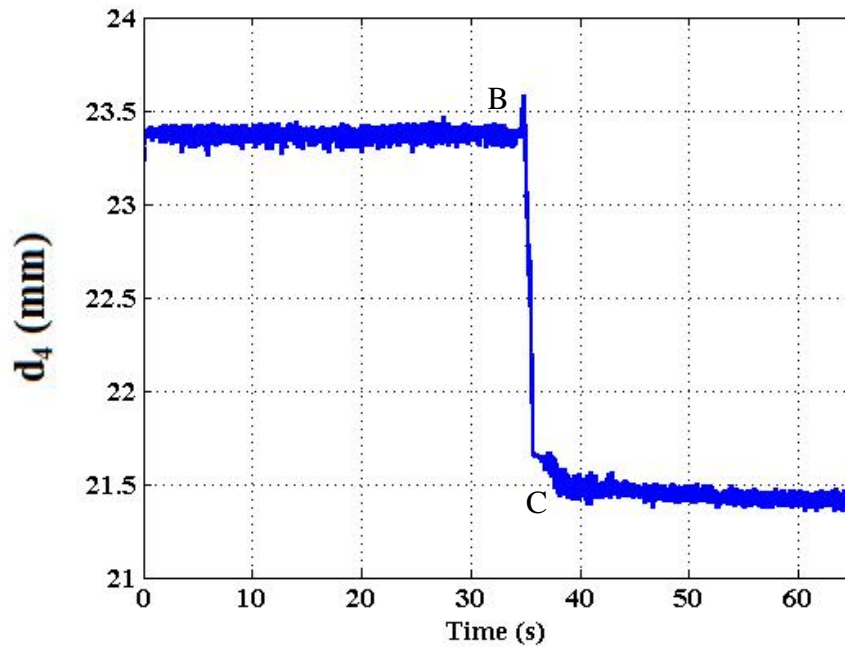

Fig. 4.3.3.10. Joint coordinate of US image acquisition device.

108

<u>Targeting Accuracy During Breast CNB</u>

Targeting accuracy is defined as the error between the centroid of the target and the needle axis when the needle is in a pre-fire position. In the above experiments, steady state is the pre-fire position of the needle. Steady state indicates that the needle is positioned close to the target and is ready to be fired for sampling the target. Root mean square error (RMSE) is used to quantify targeting accuracy. RMSE is defined as

$$\text{RMSE} = \sqrt{\frac{\sum_{t=t_i}^{t_f} (\mathbf{P_n} - \mathbf{P_t})^2}{n}} . \qquad (4.3.4.1)$$

$\mathbf{P_n}$ is a point on the needle axis such that a line passing through $\mathbf{P_n}$ and $\mathbf{P_t}$ is perpendicular to the needle axis. Table 4.3.4.1 shows the RMSE values for thirteen trials. Since targeting accuracy is evaluated at steady state, t_i and t_f are chosen such that the time interval spans the last five seconds of the experiment. Sampling time for the controller is 0.001 s, hence n equals 5001. It can be observed from Table 4.3.4.1 that the (1) average error in target position is 0.17 mm (minimum 0.02 mm; maximum 0.40 mm) (2) average time taken for positioning the target at the needle tip is 37 seconds (minimum 20 seconds; maximum 62 seconds).

Table 4.3.4.1. Targeting accuracy during needle insertion.

I[+] - Inhomogeneous; H[*] - Homogeneous

Trial	Phantom	Needle Altitude (degrees)	RMSE (mm)	Time (seconds)
1	1 (H[*])	10	0.04	37
2	1 (H)	10	0.37	35
3	1 (H)	20	0.13	40
4	1 (H)	15	0.23	30
5	1 (H)	20	0.07	38
6	2 (H)	30	0.02	62
7	2 (H)	20	0.07	42
8	5 (I[+])	20	0.08	35
9	5 (I)	10	0.40	45
10	5 (I)	20	0.33	40
11	5 (I)	20	0.12	25
12	5 (I)	20	0.16	20
13	5 (I)	20	0.14	32

CHAPTER V

CONCLUSION

In this work, a new paradigm for image guided minimally invasive procedures is presented. The basic idea is to use external robotic fingers to manipulate the position of a target embedded in soft tissue for minimizing target misalignment with a surgical instrument. This approach is fundamentally different from techniques developed in literature such as needle steering, preplanning using FEM etc. The potential advantages of this approach are increased success rate, reduced patient discomfort and enhanced diagnostic outcome. Experimental results on phantoms indicate good accuracy in target positioning. Further, experimental results also demonstrate that the proposed approach can be used to quickly and accurately sample a target with a single insertion during breast CNB. The supervisory controller can autonomously coordinate target manipulation, US image acquisition and needle insertion while monitoring safety related events to ensure fail safe and effective operation.

The major contributions of this work are

- A new technique of target manipulation for controlling the position of a target embedded inside a deformable object. This technique can be used for any deformable object exhibiting viscoelastic behavior. Applied target manipulation technique for minimizing needle – target misalignment during breast CNB.

- A passivity based controller for deformable object manipulation to ensure stability of the system.

- An approach for tracking out-of-plane target movement and detecting contact state of US probe for 2D US guided procedures.

- A supervisory controller for coordinating target manipulation, US image acquisition and needle insertion during breast CNB.

- A novel robotic system to provide assistance for breast CNB. The robotic system consists of three devices

    o A device for target manipulation to minimized needle – target misalignment.

    o A device for automated acquisition of US images.

    o A needle guidance device to facilitate needle insertion at a specific position and orientation.

As with any system, there are some limitations

- Target position information is derived through segmentation of US images. Though it is possible to segment US images of phantoms, real-time segmentation of breast US images is challenging.

- To maximize resolution of target position coordinates, the US probe is coplanar with the target manipulation plane. Hence, the needle and the US image plane are not parallel. This presents difficulty to a clinician in identifying the needle tip before sampling the target. However, as discussed previously, using a 6 degree-of-freedom EM sensor is the ideal choice for determining the needle path. In such a case, needle tip and target position are known accurately. Therefore to aid the clinician, needle and target positions can be rendered on a visual display. This can give the clinician visual confirmation before sampling the target.

- Due to manufacturing tolerances and play between mechanical components, there exists error in determining the needle path accurately with respect to the US image frame. As mentioned above, using a 6 degree-of-freedom EM sensor is the ideal choice for determining the needle path.

- The accuracy achievable with this system is limited by the resolution of target position in the direction perpendicular to the image plane of a 2D US probe.

- Due to the complex nature (anisotropy, inhomogeneity etc) of a generic deformable object (including breast tissue) the control law does not guarantee convergence of the target to the desired position. However, the passivity based control approach does ensure stability of the system.

PHANTOM SPECIFICATIONS

Homogeneous phantoms are built according to the procedure described in Chapter IV. Inhomogeneous phantoms are built by pouring plastic material with different elastic properties (determined by the volumetric ratio of plasticizer to plastic) in a mold during the cooling process. Fig. A.1 shows a cross sectional schematic of the distribution of plastic material for inhomogeneous phantoms. In Fig. A.1, dark shaded regions denote regions with higher stiffness.
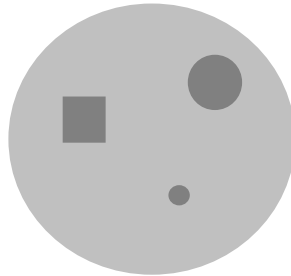
Fig. A.1. Schematic of material distribution in inhomogeneous phantoms.

Central region (in the cross section of the phantom) is the area where the distance from the center is less than (or equal to) half the radius of the phantom. Area where the distance from the center is greater than half the radius of the phantom is defined as the peripheral region. Fig. A.2 shows a schematic illustrating the central and peripheral regions in a phantom.

Fig. A.2. Central and peripheral regions in phantoms

Table A.1 shows specifications of the phantoms used in the experiments (Chapter IV).

Table A.1. Specifications for phantoms used in experiments.

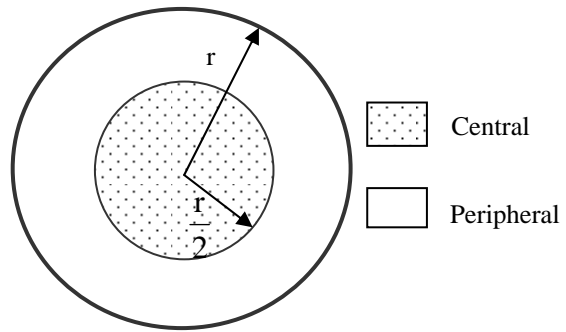| Phantom	Shape	Height (cm)	Cross Section Area (cm^2)	Composition	Plasticizer	Ratio[*]	Target Location	Target Diameter (cm)
1	Cylinder	6.5	75.4	Homogeneous	None	-	Central	1.27
2	Truncated cone	5.4	Min: 37.4; Max: 62.2	Homogeneous	Hardener	4:5	Central	1.27
3	Cylinder	6.5	73.9	Homogeneous	Hardener	19:5	Central	1.27
4	Truncated cone	5.4	Min: 37.4; Max: 62.2	Homogeneous	Softener	9:2	Central	1.27
5	Cylinder	6.9	69.4	Inhomogeneous	Softener	22:5	Central	1.91
6	Truncated cone	6.1	Min: 37.4; Max: 67.9	Homogeneous	None	-	Peripheral	0.64
7	Cylinder	5.4	75.4	Inhomogeneous	Softener	5:2	Central	1.27
8	Cylinder	4.1	67.9	Homogeneous	None	-	Central	0.64
9	Cylinder	3.0	73.9	Homogeneous	None	-	Central	1.27

[*]**Ratio** – Volumetric ratio of plastic to plasticizer.

REFERENCES

[1] W. Wein, S. Brunke, A. Khamene, M. R. Callstrom, N. Navab, "Automatic CT-ultrasound registration for diagnostic imaging and image-guided intervention," *Medical Image Analysis* (2008), doi:10.1016/j.media.2008.06.006.

[2] S. P. DiMaio, S. E. Salcudean, "Needle insertion modeling and simulation," *IEEE Transactions on Robotics and Automation*, Vol. 19, No. 4, October 2003.

[3] M. F. Dillon, A.D. Hill, C. M. Quinn, et al, "The accuracy of ultrasound, stereotactic, and clinical core biopsies in the diagnosis of breast cancer, with an analysis of false – negative cases," *Annals of Surgery,* Vol. 242, No. 5, pp. 701–707, 2005.

[4] G. J. Whitman, B. Erguvan – Dogan, W. T. Yang, et al, "Ultrasound – guided breast biopsies," *Ultrasound Clinics,* Vol 1, pp. 603–615, 2007.

[5] E. M. Boctor, M. A. Choti, E. C. Burdette, R. J. Webster III, "Three – dimensional ultrasound – guided robotic needle placement: an experimental evaluation," *International Journal of Medical Robotics and Computer Assisted Surgery,* Vol. 4, pp. 180–191, 2008.

[6] S. Okazawa, R. Ebrahimi, J. Chuang, S. E. Salcudean, R. Rohling, "Hand-held steerable needle device," *IEEE/ASME Transactions on Mechatronics*, Vol. 10, pp 285-296, June 2005.

[7] D. Glozman, M. Shoham, " Image-guided robotic flexible needle steering," *IEEE Transactions on Robotics*, Vol. 23, No. 3, pp 459–467, June 2007.

[8] R. J. Webster III, J. S. Kim, N. J. Cowan, G. Chirikjian, and A. M. Okamura, "Nonholonomic modeling of needle steering," *International Journal of Robotics Research*, 25(5/6), pp. 509–526, May/June 2006.

[9] M. H. Loser, N. Navab, "A new robotic system for visually controlled percutaneous interventions under CT fluoroscopy", in *Proc. MICCAI*, Vol. 1935, LNCS, pp.887-896, 2000.

[10] F. S. Azar, D. N. Metaxas, M. D. Schnall, "Methods for modeling and predicting mechanical deformations of the breast under external perturbations," *Medical image Analysis*, Vol. 6, pp 1-27, 2002.

[11] R. Alterovitz, K. Goldberg, J. Pouliot, R. Taschereau, I-C. Hsu, "Sensorless planning for medical needle insertion procedures," in *Proc. IEEE International Conference on Intelligent Robots and Systems*, pp. 3337–3343, October 2003.

[12] P. Wellman, "Tactile imaging," PhD dissertation, Division of Engineering and Applied Sciences, Harvard University, Cambridge, Massachusetts, 1999.

[13] F. S. Azar, D. N. Metaxas, M. D. Schnall, "Methods for modeling and predicting mechanical deformations of the breast under external perturbations," *Medical image Analysis*, Vol. 6, pp 1-27, 2002.

[14] T. A. Krouskop, T. M. Wheeler, F. Kallel, B. S. Garra, T. Hall, "The elastic moduli of breast and prostate tissues under compression," *Ultrasonic Imaging,* Vol. 20, pp. 151-159, 1998.

[15] M. Raibert, J. Craig, "Multi-Manipulator control for fixtureless assembly of elastically deformable parts," in *Proc. Japan-USA Symposium on Flexible Automation,* Vol. 2, pp. 1565-1572, 1992.

[16] Z. Doulgeri, A. Golfakis, "Nonlinear manipulation control of a compliant object by dual fingers," *Journal of Dynamic Systems, Measurement, and Control,* Vol. 128, pp. 473-481, 2006.

[17] A. M. Howard, G. A. Bekey, "Intelligent learning for deformable object manipulation," in *Proc. IEEE International Symposium on Computational Intelligence in Robotics and Automation,* pp. 15-20, 1999.

[18] F. F. Khalil, P. Payeur, "Robotic interaction with deformable objects under vision and image guidance – A review," *IEEE International Workshop on Robotic and Sensors Environments,* pp. 1-6, 2007.

[19] N. H. McClamroch, "Displacement control of flexible structures using electrohydraulic servo-actuators," *Journal of Dynamic Systems, Measurement and Control*, Vol 107, pp. 34-39, March 1985.

[20] D. Hughes, J. T. Wen, "Passivity motivated controller design for flexible structures," in *Proc. IEEE International Conference on Robotics and Automation,* pp. 749-754, 1993.

[21] T. Wada, S. Hirai, S. Kawamura, N. Kamiji, "Robust manipulation of deformable objects by a simple PID feedback," in *Proc. International Conference on Robotics and Automation*, pp 85-90, 2001.

[22] M. T. Ho, Y. W. Tu, "PID controller design for a flexible link manipulator," in *Proc. IEEE Conference on Decision and Control,* pp. 6841-6846, 2005.

[23] J. Donne, K. Ossman, U. Ozguner, M. Boesch, A. Ahmed, "Adaptive control of a flexible structure with noncollocated sensors and actuators," in *Proc. IEEE International Symposium on Intelligent Control,* pp. 719-723, Sep 1990.

[24] A. Albu-Schaffer, O. Christian, G. Hirzinger, "Constructive energy shaping based impedance control for a class of underactuated Euler-Lagrange systems," in *Proc. IEEE International Conference on Robotics and Automation*, pp. 1387-1393, 2005.

[25] J. H. Ryu, D. S. Kwon, B. Hannaford, "Control of a flexible manipulator with noncollocated feedback: Time-domain passivity approach," *IEEE Transactions on Robotics,* Vol. 20, No. 4, pp. 776-780, Aug 2004.

[26] T. Wada, S. Hirai, S. Kawamura, "Planning and control of indirect simultaneous positioning operation for deformable objects," in *Proc. International Conference on Robotics and Automation*, pp 2572-2577, 1999.

[27] T. Wada, S. Hirai, S. Kawamura, "Indirect simultaneous positioning operations of extensionally deformable objects," in *Proc. International Conference on Intelligent Robots and Systems*, pp 1333-1338, 1998.

[28] V. D. Nguyen, "Constructing force-closure grasps." in *Proc. International Conference on Robotics and Automation*, Vol. 3, pp. 1368 – 1373, 1986.

[29] D. Alazard, J. P. Chretien, "Flexible joint control: Robustness analysis of the collocated and non-collocated feedbacks, in *Proc. IEEE International Conference on Intelligent Robots and Systems,* pp. 2102-2107, 1993.

[30] Y. S. Kim, B. Hannaford, "Some practical issues in time domain passivity control of haptic interfaces," in *Proc. IEEE/RSJ International Conference on Intelligent Robots and Systems,* pp. 1744-1750, 2001.

[31] J. H. Ryu, D. S. Kwon, B. Hannaford, "Stability guaranteed control: Time domain passivity approach," *IEEE Transactions on Control Systems Technology,* Vol. 12, No. 6, pp. 860-868, Nov 2004.

[32] J. E. Colgate, N. Hogan, "Robust control of dynamically interacting systems," *International Journal of Control,* Vol. 48, No. 1, pp. 65-88, 1988.

[33] S. M. Joshi, A. M. Kelkar, "Passivity-based control of elastic systems," in *Proc. IEEE International Conference on Control Applications*, pp. 724-729, 1997.

[34] B. Brogliato, R. Lozano, B. Maschke, O. Egeland, *Dissipative Systems Analysis and Control.* London: Springer, pp. 373-434, 2007.

[35] B. Hannaford, J. H. Ryu, "Time domain passivity control of haptic interfaces," *IEEE Transactions on Robotics and Automation,* Vol. 18, No. 1, pp. 1-10, 2002.

[36] T. Nilsson, M. Perez, "Introduction to passivity-based control of Euler-Lagrange systems," School of Mathematics and Systems Engineering, Vaxjo University, Sweden, Report 03112 (ISSN 1650-2647), November 2003.

[37] H. G. Tanner, K. J. Kyriakopoulos, "Analysis of deformable object handling," in *Proc. IEEE International Conference on Robotics and Automation,* pp. 2674-2679, 1999.

[38] American Cancer Society, "Cancer Facts & Figures-2008," http://www.cancer.org/downloads/STT/2008CAFFfinalsecured.pdf, accessed on 16th May, 2008.

[39] J. G. Elmore, K. Armstrong, C. D. Lehman, S. W. Fletcher, "Screening for Breast Cancer," *Journal of American Medical Association*, Vol. 293, No. 10, pp. 1245-1256, March 2005.

[40] L. Liberman, T. L. Feng, D. D. Dershaw, E. A. Morris, A. F. Abramson, "US-guided core breast biopsy: use and cost-effectiveness," *Radiology*, Vol. 208, 717-723, 1998.

[41] B. D. Fornage, "Sonographically guided needle biopsy of nonpalpable breast lesions," *Journal of Clinical Ultrasound*, Vol. 27, No. 7, September 1999.

[42] T. A. S. Matalon, B. Silver, "US guidance of interventional procedures," *Radiology*, Vol. 174, 43-47, 1990.

[43] W. L. Smith, K. J. M. Surry, G. R. Mills, D. B. Downy, and A. Fenster, "Three-dimensional ultrasound-guided core needle breast biopsy," *Ultrasound in Medicine and Biology*, Vol. 27, No. 8, pp. 1025–1034, 2001.

[44] S. H. Parker, K. D. Hopper, W. F. Yakes, M. D. Gibson, J. L. Ownbey, T. E. Carter, "Image-directed percutaneous biopsies with a biopsy gun," *Radiology*, Vol. 171, 663-669, 1989.

[45] S. H. Parker, F. Burbank, "A practical approach to minimally invasive breast biopsy," *Radiology*, Vol. 200, 11-20, 1996.

[46] A. J. Leibman, D. Frager, P. Choi, " Experience with breast biopsies using the Advanced Breast Biopsy Instrumentation system," *American Journal of Roentgenology*, Vol. 172, 1409-1412, 1998.

[47] K. Cleary, A. Melzer, V. Watson, G. Kronreif, D. Stoianovici, "Interventional robotic systems: Applications and technology state-of-the-art," *Minimally Invasive Therapy and Allied Technologies*, Vol. 15, No. 2, 101-113, 2006.

[48] N. V. Tsekos, J. Shudy, E. Yacoub, P. V. Tsekos, I. G. Koutlas, "Development of a robotic device for MRI-guided interventions in the breast," in *Proc. Bioinformatics and Bioengineering Conference*, 201-208, 2001.

[49] D. Stoianovici, L. Whitcomb, J. Anderson, R. Taylor, and L. Kavoussi, "A modular surgical robotic system for image guided percutaneous procedures," in *Proc. MICCAI*, Vol. 1496, LNCS, pp. 404–410, 1998.

[50] K. Cleary,M. Freedman, M. Clifford, D. Lindisch, S. Onda, and L. Jiang, "Image-guided robotic delivery system for precise placement of therputic agents," *J. Controlled Release*, Vol. 74, No. 1, pp. 363–368, July 2001.

[51] A. Patriciu, S. Solomon, L. Kavoussi, and D. Stoianovici, "Robotic kidney and spine percutaneous procedures using a new laser-based CT registration method," in *Proc. MICCAI*, Vol. 2208, pp.249–257, 2001.

[52] D. Stoianovici et al., "A novel mechanical transmission applied to percutaneous renal access," in *Proc. ASME Dynamic Systems Control Division, DSC*, Vol. 61, pp. 401–406, 2001.

[53] F. Pierrot, E. Dombre, E. Degoulange, L. Urbain, P. Caron, S. Boudet, J. Gariepy, J. Megnien, "Hippocrate: A safe robot arm for medical applications with force feedback," *Medical Image Analysis*, Vol. 3, No. 3, pp. 285-300, 1999.

[54] K. Masuda, E. Kimura, N. Tateishi, K. Ishihara, "Three-dimensional motion mechanism of ultrasound probe and its application for tele-echography system," in *Proc. IEEE/RSJ International Conference on Intelligent Robots and Systems*, pp. 1112-1116, 2001.

[55] A. Vilchis, J. Troccaz, P. Cinquin, K. Masuda, F. Pellisier, "A new robot architecture for tele-echography," *IEEE Transactions on Robotics and Automation*, Vol. 19, No. 5, pp. 922-926, 2003.

[56] J. Hong, T. Dohi, M. Hashizume, K. Konishi, N. Hata, "An ultrasound driven needle insertion robot for percutaneous cholecystostomy," *Physics in Medicine and Biology*, Vol. 39, No. 3, pp. 441-455, 2004.

[57] M. A. Vitrani, G. Morel, T. Ortmaier, "Automatic Guidance of a surgical instrument with ultrasound based visual servoing," in *Proc. IEEE International Conference on Robotics and Automation*, pp. 510-515, 2005.

[58] P. Abolmaesumi, S. E. Salcudean, W. Zhu, M. R. Sirouspour, S. P. DiMaio, "Image-guided control of a robot for medical ultrasound," *IEEE Transactions on Robotics and Automation*, Vol. 18, No. 1, Feb 2002.

[59] A. Krupa, G. Fichtinger, G. D. Hager, "Full motion tracking in ultrasound using image speckle information and visual servoing," in *Proc. IEEE International Conference on Robotics and Automation*, pp. 2458-2464, 2007.

[60] H. Olsson, K. J. Astrom, "Friction generated limit cycles", *IEEE Transactions on Control Systems Technology*, Vol 9, pp 629-636, 2001.

[61] J. J. Craig, *Introduction to Robotics: Mechanics and control,* 3rd ed, Upper Saddle River, NJ, 2005.

[62] P. J. Antsaklis, X. D. Koutsoukos, "Hybrid systems: review and recent progress," In Samad, T., editor. *Software Enabled Control: Information Technology for Dynamical Systems*. NY: Wiley-IEEE; 2003.

[63] P. J. Antsaklis, "A brief introduction to the theory and applications of hybrid systems," in *Proc. IEEE Special Issue on Hybrid Systems: Theory and Applications*, Vol. 88, No. 7, pp. 879-887, 2000.